

Errata
C 750002

A067183
Jan 30 1981

LEVEL

SALES NO. 33292



70

LASER ASSISTED SEMICONDUCTOR

DEVICE PROCESSING

FINAL TECHNICAL REPORT

1 JUNE 1978 - 30 NOVEMBER 1980

DTIC
ELECT
APR 7 1981
C

This research was sponsored by the
Defense Advanced Research Projects Agency
and the Naval Ocean Systems Center under
ARPA Order No. 3578
Contract No. MDA903-78-C-0284
Monitored By: Dr. Isaac Lagnado
Naval Ocean Systems Center
Contract Duration: 1 June 1978 - 30 November 1980

30 NOVEMBER 1980

DISTRIBUTION STATEMENT A
Approved for public release;
Distribution Unlimited

TRW

DEFENSE AND SPACE SYSTEMS GROUP

One Space Park, Redondo Beach, Ca 90278

81 3 10 004

AD A 097427

DTIC FILE COPY

TABLE OF CONTENTS

	<u>PAGE</u>
PART I - LASER INDUCED SURFACE PROCESSING	1
1.0 Introduction	3
2.0 Results	4
2.1 The Effect of Damage on Laser Heating	4
2.2 Laser Annealing of Low Fluence Ion-Implanted Silicon	5
 APPENDIX A - The Effect of Carrier Diffusion on Laser Heating of Lightly Damaged Semiconductors	 9
 APPENDIX B - Laser Annealing of Low Fluence Ion Implanted Silicon	 23
 APPENDIX C - Contribution of Free Electrons to Optical Absorption in Semiconductors	 31
 PART II - LASER BLOW-OFF ION IMPLANATION	 56
1.0 Summary	57
2.0 Experimental Apparatus	60
2.1 The Laser Blow-Off Plasma	64
3.0 Characterization of Silicon Surfaces Ion Implanted by the Laser Blow-Off Technique	73
3.1 The as-implanted Surfaces	73
3.2 Uniformity of Implantation	74
3.3 Implant Fluence	76
3.4 Implant Penetration	77
3.5 Implant Damage	78
3.6 Groove and Stain Technique	80
4.0 Ion Microprobe Comparisons	83
4.1 Preparation of Standards by Conventional Ion Implantation	83
4.1.1 Equipment Description	83
4.1.2 Process	83

Accession For	
NTIS GRA&I	<input checked="" type="checkbox"/>
DTIC TAB	<input type="checkbox"/>
Unannounced	<input type="checkbox"/>
Justification	<input type="checkbox"/>
By _____	
Distribution/	<input type="checkbox"/>
Availability Co	<input type="checkbox"/>
Special	<input type="checkbox"/>
A	

TABLE OF CONTENTS

	<u>PAGE</u>
4.2 Preparation of Annealed Ion Implant Standards	85
4.2.1 Cleaning Procedure	85
4.2.2 Annealing Procedure	85
4.3 Procedure for Profiling Boron Implantation in Silicon Wafers using the Ion Microprobe (IMMA)	86
4.3.1 Introduction	86
4.3.2 Sample	86
4.3.2.1 Sample Preparation	86
4.3.2.2 Sample Constraints	86
4.3.3 Sample Receipt	87
4.3.4 IMMA Sample Holder and Fixture Cleaning Procedure	87
4.3.5 Sample Fixture Loading	87
4.3.6 Stage Auto Vent and Pump Down	87
4.3.7 Operating Conditions	88
4.3.7.1 Beam Alignment	88
4.3.7.2 System Operation Conditions	88
4.3.8 Measurements	88
4.4 Results of Ion Microprobe Comparisons of Laser Blow-Off Ion Implants with Conventional Implants	92
4.5 Nature of Non Mass-Analyzed Ion Implantation	95
4.6 Results of Evaluation of Laser Blow-Off Ion Implanted Devices	100
APPENDIX A - Thermal Transport in the Target Material During Laser Blow-Off Ion Implantation	103

↓
This report is divided into two separate sections, Part I and Part II, which correspond to the major contractual tasks.

↳ Part I covers the work on "Laser Induced Surface Processing". → p 2

Part II covers the work on "Laser Blow-Off Ion Implantation".

Each part has separate section numbering, references and appendices.

PART I - LASER INDUCED SURFACE PROCESSING

implant

SUMMARY OF FINAL REPORT, PART I

↓
PART I

The objective of ~~Task 1~~ of this program was to evaluate and characterize laser-induced processing of semiconductor materials and devices. The work described here was performed under Contract No. MDA 903-78-C-0284 during the period of June 1978 to July 1979. The results of this work were also presented in two semi-annual reports, and the salient parts and conclusions are presented here. In particular, reprints of two published papers from this work are included as appendices A and B (also as References 1 and 2). Appendix C contains an unpublished derivation of the contribution of free electrons to optical absorption in semiconductors.

> p57

The TRW contribution to laser-induced processing of semi-conductor surfaces consisted of the demonstration of the effect of lattice damage on the laser-induced heating,¹ and the development of annealing techniques for lightly damaged materials.² This new technique, pioneered at TRW, consists of combining a laser anneal with a short low temperature thermal anneal. It exploits the unique ability of laser processing to dissolve lattice defects without providing sufficient energy for melting or regrowth. A detailed discussion of the effect of damage on the laser-induced heating is given in Section 2.1 and Appendix A.

In our new technique, the sample is first irradiated by a pulsed laser. This removes lattice defects. This defect-free material is then subjected to a moderate thermal anneal. This results in full electrical activation without significant change in the impurity distribution. Thus, by combining laser irradiation with short low temperature thermal anneal, it is possible to both eliminate defects and electrically activate lightly damaged semi-conductors. Since melting is avoided, the dopant distribution remains as implanted. The results of these experiments are summarized in Section 2.2 and Appendix B. Preliminary experiments have also shown that this technique can be applied to high fluence implants.

1.0 INTRODUCTION

In our work at TRW, we have investigated the important difference between annealing of heavily and lightly damaged materials. Our original results confirmed findings recently reported in the literature: for lightly damaged samples, the crystal regrowth was poor, and only partial electrical activation was obtained, though the displacement damage was removed. In contrast, for high fluence samples, excellent activation was obtained.

The mechanism for the Q-switched laser annealing is believed to involve melting of the amorphized surface followed by liquid phase regrowth.^{3,4} Here, the defects are almost completely removed and a full activation of dopants at concentrations far exceeding the equilibrium limit of solid solubility has been reported.⁵ This method has its biggest potential in applications where slight changes in the implanted profiles can be tolerated. This is because melting results in some impurity redistribution. For ruby annealed silicon samples, typical profile widths are around 0.3 μm .^{1,5}

Our early experiments lead us to thoroughly investigate the effect of damage on the laser-induced heating. For the theoretical effort, we have developed a model¹ which explains the observed differences between annealing of heavily and lightly damaged surfaces. This is done by taking into account diffusion of the photoexcited carriers. This is discussed in Section 2.1 and Appendix A. In our experimental effort, we have subsequently developed a novel technique² which permits laser annealing of lightly damaged materials. This has the very attractive feature of maintaining the as-implanted impurity profiles. This is discussed in Section 2.2 and Appendix B. Preliminary experiments have also shown that this technique can be applied to high fluence implants.

2.0 RESULTS

2.1 The Effect of Damage on Laser Heating. The conversion of optical to thermal energy during laser annealing consists of two major processes:

- Absorption of laser light
- Conversion of absorbed optical energy to heat.

In strongly absorbing semiconductors, the dominant absorption mechanism at frequencies higher than the bandgap frequency is interband transitions. The absorbed energy is released to heat through the thermalization of the photoexcited carriers, i.e., heat is distributed into a depth comparable to carrier diffusion length. In good quality materials, the carrier diffusion lengths are longer than the optical absorption depth. Thus, the heating volume is enlarged, and for the same laser power, the average temperature is lower than in heavily damaged material.

The carriers recombine preferentially at defect sites, producing localized thermal spikes. If the density of the nonradiative recombination centers is high, the average temperature is high. This is the case in heavily damaged materials. At these elevated temperatures epitaxial regrowth (liquid phase) and impurity activation occur. If the density is low, the average temperature is low. This is the case in lightly damaged materials. Here the application of laser fluxes equivalent to that used in high fluence implants produces no melting in low fluence implants. No regrowth and little or no dopant activation occur even though the defects dissolve due to the preferential supply of energy at the defect sites. Thus, it is possible in lightly damaged materials to remove the displacement damage even without providing sufficient average energy to activate implanted impurities.

Our detailed thermal analysis supports this picture. We have developed a model¹ which explains the observed differences between annealing of lightly and heavily damaged materials by taking into account the diffusion of the photoexcited carriers. Previous thermal models were concerned with heavily damaged materials, in that they assumed that the absorbed optical energy is converted to heat in the immediate vicinity of the absorbed photons. In our work, the time evolution of temperature profiles was calculated for pulsed ruby and Nd:YAG illumination of silicon and ruby illumination of GaAs. The material, optical, and electronic properties were varied, to represent varied material quality. Surface recombination of the carriers was also taken into account. The effect of the damage on the heating was found to be much more pronounced for Nd:YAG than for ruby irradiation because a larger portion of the ruby laser energy (excess above bandgap) is given rapidly to the lattice through quasi-thermalization inside the semiconductor energy bands. Thermal spikes were formed as the result of the preferential recombination of the carriers at the surface. For a sufficiently fast surface recombination, the temperature profile may develop a secondary maximum in the bulk.

2.2 Laser Annealing of Low Fluence Ion-Implanted Silicon. The most successful applications of Q-switched lasers have been for annealing of high fluence implants.³ The method involves a pulsed laser such as a Q-switched Nd:YAG or ruby laser, with a typical pulse length between 10 and 200 nsec, and energy density between .5 and 3 J/cm². The annealing mechanism is believed to be melting of the amorphized surface followed by liquid phase regrowth.^{4,5} Here there is almost complete removal of defects and a full activation of dopant concentrations far exceeding the limit of solid solubility.^{3,5} However, this method can be only applied where slight changes in implanted profile can be tolerated. This is because melting results in some impurity redistribution. Typical profile widths in ruby laser annealed silicon are around 0.3 μm .^{3,6}

The second laser anneal method employs a cw laser operated in a scanning mode. For example, a 7W cw argon laser beam scanned at 2.76 cm/sec and producing lines of 22 μm width was used to anneal to a 1000 Å depth in as-implanted silicon.⁷ The recrystallization is through solid state regrowth, because of the low powers and comparatively long anneal times. The dopant profiles are not changed by cw laser annealing.

The as-implanted impurity profiles can be maintained even in pulsed laser annealing by using techniques developed at TRW. These techniques consist of combined laser irradiation and low temperature thermal anneal. In our work at TRW we have systematically investigated the differences between annealing of lightly damaged materials and heavily damaged materials. We have applied ruby laser pulses of 1.5 to 2.5 J cm² to silicon surfaces oriented in [100] and [111] directions and implanted with 10^{14} to 10^{15} B cm⁻² and 10^{14} to 5×10^{14} B cm⁻². Boron implantations were at 50 keV, phosphorous at 80 keV. It was found that laser energy densities used for high fluence implants did not produce melting or regrowth in the low fluence implants. Although the electrical activation was poor, the lattice defects (e.g., dislocation loops) were removed. We have concluded that the average temperature induced in the lightly damaged material was substantially lower than the temperature induced in the heavily damaged material. This permitted only a small fraction of the implanted ions to migrate to substitutional positions. The damage was removed through the preferential heating at the defect sites.¹ However, when a sequential moderate thermal anneal, 10 min at 1000°C, was applied to these samples, a full electrical activation, and without significant impurity redistribution, was obtained. Thus, by combining a laser anneal with a short thermal anneal, it was possible to achieve defect elimination as well as complete electrical activation. This was the first reported² successful use of pulsed laser radiation for annealing of low fluence implants.

Preliminary experiments have shown that we can also apply these techniques to high fluence implants. One type of implantation, that of $5 \times 10^{14} \text{ P cm}^{-2}$ into a [111] surface, resulted in amorphism. Our early experiments as well as others in the literature showed that irradiation of amorphized surfaces by a Q-switched ruby laser results in melting. Thus, in order to avoid melting, the damaged region should first be recrystallized. This was done by introducing a moderate thermal anneal before the irradiation. To date, the best results were obtained with a two-step thermal anneal, 30 min at 550°C, and 10 min at 1000°C. This caused the amorphous layer to regrow into single crystallinity by solid phase epitaxy. The subsequent irradiation eliminated defects without melting. Not only did we eliminate the defects, but by avoiding melting, we also maintained the desirable as-implanted impurity profiles.

The demonstrated techniques have an enormous potential for practical applications. Low fluence implants account for more than 50 percent of the potential implant uses since all bases for junction transistors fall into this category. The ability to anneal high fluence implants without dopant redistribution is important for the production of shallow emitters, which are essential for an entire category of devices, such as microwave transistors. The ability to anneal material without changing the implanted profiles would permit full exploitation of the ion-implant unique capability of creating narrow accurately controlled impurity profiles.

REFERENCES

1. J. Z. Wilcox, "The Effect of Carrier Diffusion on Laser Heating of Lightly Damaged Semiconductors," J. Appl. Phys. 51, 2866 (1980). See Appendix A
2. S. Prussin and W. von der Ohe, "Laser Annealing of Low Fluence Ion-Implanted Silicon," J. Appl. Phys. 51, 3853 (1980). See Appendix B
3. For a review article and further reference, see C. W. White, J. Narayan, and R. T. Young, "Laser Annealing of Ion-Implanted Semiconductors," Science 204, 461 (1977).
4. R. Baeri, et al., "Arsenic Diffusion in Silicon Melted by High-Power Nanosecond Laser Pulsing," Appl. Phys. Letters 33, 137 (1978).
5. D. H. Auston, et al., "Time-Resolved Reflectivity of Ion-Implanted Silicon During Laser Annealing," Appl. Phys. Letters 33, 437 (1978).
6. J. C. Muller, et al., "Laser Beam Annealing of Heavily Doped Implanted Layers on Silicon," Appl. Phys. Letters 33, 287 (1978).
7. A. Gat, et al., "Physical and Electrical Properties of Laser-Annealed Ion-Implanted Silicon," Appl. Phys. Letters 32, 276 (1978).

APPENDIX A

THE EFFECT OF CARRIER DIFFUSION ON LASER-HEATING OF LIGHTLY DAMAGED SEMICONDUCTORS

J. Z. WILCOX

TRW Defense and Space Systems Group
One Space Park, Redondo Beach, Ca 90278

The effect of carrier diffusion on laser heating of lightly damaged semiconductors

Jaroslava Z. Wilcox

TRW Defense and Space Systems Group, Redondo Beach, California 90278

(Received 10 September 1979; accepted for publication 6 December 1979)

It has been observed that the surface temperature obtained during laser heating of lightly damaged material is generally considerably lower than the temperature obtained in heavily damaged material. We develop a model which explains this observation by taking into account the diffusion of the photoexcited carriers. The time evolution of temperature profiles was calculated for pulsed ruby and Nd : YAG illumination of silicon and ruby illumination of GaAs. The material, optical, and electronic properties were varied, according to the material quality. Surface recombination of the carriers was also taken into account. For the same laser power, the induced temperature was lower and the heating times were longer in good-quality materials than in heavily damaged materials. This is because of longer carrier diffusion lengths in good-quality material. The effect of the damage on the heating was found to be much more pronounced for Nd : YAG than for ruby irradiation because a larger portion of the ruby laser energy (excess above band gap) is given rapidly to the lattice through quasithermalization inside the semiconductor energy bands. Thermal spikes are formed as the result of the preferential recombination of the carriers at the surface. For a sufficiently fast surface recombination, the temperature profile may develop a secondary maximum in the material interior.

PACS numbers: 79.20.Ds, 66.70. + f, 72.20.Jv, 81.40.Ef

1. INTRODUCTION

There is considerable interest in the use of lasers for processing of semiconductor surfaces.¹ The majority of experiments have been in *Q*-switched ruby and Nd : YAG laser annealing of comparatively high-dose implantations. In these experiments, the resulting activated dopant concentrations were often in excess of the limits of equilibrium solid solubility, and the shapes of the ion-implanted profiles were changed as a result of the illumination.² This led to the suggestion that the near-surface regions of the irradiated material actually melted and underwent a type of liquid epitaxy in these experiments. The suggested model is strongly supported by numerical results of several model calculations.³

Heavily damaged material has been successfully annealed also with scanned cw Kr and Ar ion lasers.⁴ No significant dopant redistribution was observed after the annealing, indicating that the regrowth was through solid-state epitaxy.

Laser annealing of lightly damaged material has enjoyed much less attention. The available data indicate a strong sensitivity to the dose of the implanted impurities. Excellent single-crystal regrowth was obtained in Nd : YAG annealing of high-dose samples, while in lower-dose samples the regrowth was poor.⁵ Furthermore, laser powers which melted implanted silicon did not affect the unimplanted regions of the material.⁶ For ruby laser annealing, carrier densities for lower-dose implants were essentially the same as those obtained by the thermal annealing, while in the higher-dose range the carrier density was much higher.⁷ The use of *Q*-switched ruby laser for annealing of low-fluence silicon was studied in greater detail in Ref. 8. The fluences studied ranged from 10^{14} to 10^{15} B/cm² and 10^{14} to 5×10^{14} P/cm². The laser energies were 1–2.5 J cm⁻². No melting and only partial electrical activation occurred as a

result of the irradiation. However, the implant defects were fully dissolved.⁸ Full electrical activation was obtained (at 2 J cm^{-2}) only for the $\{111\}$ surface amorphized by an implant of $5 \times 10^{14} \text{ P/cm}^2$. For nonamorphized surfaces, powers of 2.5 J cm^{-2} produced only partial activation; these surfaces could be activated fully by applying a sequential thermal anneal. In a related series of experiments, we have applied ruby radiation also to silicon which had been subjected to neutron bombardment.⁹ Again, no electrical activation occurred unless the wafers were additionally damaged by Ne implant. However, the surfaces showed melt spots in the vicinity of defects, indicating that the laser energy was released primarily at the defects.

The present work addresses the difference between laser-induced heating of heavily and lightly damaged materials. It presents the results of the thermal calculations which take into account the diffusion of the photoexcited carriers. Previous thermal models have been concerned with heavily damaged materials, in that they assumed that the absorbed optical energy is converted to heat in the immediate vicinity of the absorbed photons. However, in strongly absorbing semiconductors, the primary effect of the absorbed radiation is to generate carriers. Heat is generated when the carriers recombine, i.e., after they have diffused a distance on the order of carrier diffusion length. In good-quality materials, the diffusion lengths may be longer than the optical absorption depth. Hence, the carrier diffusion enlarges the heating volume, and, for the same laser power, causes the surface temperature in lightly damaged material to be lower than in heavily damaged material. Furthermore, a large number of carriers will reach, and recombine at, the surface, making it qualitatively feasible to melt surface defects in lightly damaged materials.

The conversion of optical energy to heat consists of two

major steps: (i) absorption of laser light, and (ii) conversion of absorbed optical energy to heat. We consider strongly semiconductors. In strongly absorbing semiconductors, the dominant¹⁰ absorption mechanism at frequencies higher than the band-gap frequency is interband transitions. The conversion of absorbed energy to heat is accomplished through thermalization of photoexcited carriers. Once the conversion has been accomplished, the temperature distribution is determined by solving the thermal diffusion equation in the semiconductor. At issue is the proper representation of the source term in the heat equation.

In the model used in this work, we categorize the thermalization as consisting essentially of two steps, operative either in parallel or in sequence: relaxation of the electron "excess" energy (above the band gap), and relaxation of the band-gap portion of the energy. The categorization is convenient because the electron redistribution inside the conduction band proceeds generally at a different rate than the electron-hole recombination across the semiconductor band gap. The band-gap portion of the electron energy is released to heat at the rate $\approx E_g \Delta n \tau^{-1}$, where τ is the carrier lifetime, E_g is the semiconductor band gap, and $\Delta n = \Delta n(x, t)$ is concentration of the photoexcited carriers. Δn is calculated by solving the electron diffusion equation. Thus, the band-gap portion of the electron energy is released into a volume bounded by a depth equal to $\max(L, \alpha^{-1})$, where $L \approx (D\tau)^{1/2}$, D is the carrier diffusivity, and α is the optical absorption coefficient.

The conversion of the excess portion of the electron energy is assumed in this work to be instantaneous. This is because the characteristic "quasithermalization" frequency is on the order of the lattice vibrational frequency, $f_c \approx 10^{12}$ – 10^{13} sec⁻¹, which is much faster than any other rate in the problem.¹¹

The presence of defects and interfaces also affects the heating profiles. Interfaces affect heating mainly because of surface recombination of the photoexcited carriers. The effect of the surface will be taken into account in this work through the surface recombination velocity v_s .

Bulk defects may be categorized as localized or distributed. Both affect optical absorption as well as carrier diffusion. The influence of the distributed defects will be taken into account in that the values of the optical absorption coefficient, carrier lifetime, and diffusivity will be different for heavily damaged than for good-quality materials. However, the crystal will be considered homogeneous, and its properties independent of time. In this sense, the values of the material parameters used are some "average" values of the parameters during the processing. The main reason for this is mathematical simplicity. The localized bulk defects will not be treated here explicitly. However, their effect on the heating should be similar to that of the surface defects. This is because both surface and localized defects are fast recombination centers, with the subsequent release of the carrier energy. This leads to the formation of thermal spikes at, and a possible dissolution of, localized defects.

As has already been mentioned, the "band-gap energy source term" in the heat equation requires knowledge of the electron concentration, $n(x, t)$. For constant τ , D , and v_s , we

have solved the electron diffusion equation exactly for a square-shaped laser pulse (no drift current). The solution for $n(x, t)$ is a closed-form expression consisting of complementary error functions. To the best of our knowledge, this solution has never before been reported in the literature. The existence of a closed-form expression for $n(x, t)$ is important for our purposes since it avoids numerical integration of the electron diffusion equation. The heat transport equation is then solved numerically, with the temperature dependence of the thermal conductivity included.

In Sec. II, we describe the mathematical basis of the model. In Sec. III, we discuss the results of the numerical computations of the temperature. Section IV summarizes the results.

II. MODEL

The photon-to-thermal conversion consists of photoexcitation and thermalization of the photoexcited carriers, and heat transport.

A. Concentration of photogenerated carriers

The instantaneous concentration of the photogenerated carriers is, in the one-dimensional approximation and in the absence of electric fields, obtained by solving the electron transport equation,

$$\frac{\partial n}{\partial t} = g - \frac{\Delta n}{\tau} + D \frac{\partial^2 n}{\partial x^2}, \quad (1)$$

where the generation function g gives the photogeneration rate of the carriers,

$$g = \alpha N \exp(-\alpha x), \quad (2)$$

where α is the optical absorption coefficient and $N = N(t)$ is the photon flux incident at the surface. $N(t) = F(t)/h\nu$, where $F(t)$ is the absorbed laser power and $h\nu$ is the photon energy.

$$\Delta n \equiv n(x, t) - n_0, \quad (3)$$

where n_0 is the equilibrium concentration and τ and D are minority-carrier lifetime and diffusion constant, respectively.

In Eq. (1), α , τ , and D are, in general, functions of both x and t . The x dependence arises due to the spatial inhomogeneities in the semiconductor; the time dependence arises from the dependence of α , D , and τ on temperature. Additional time dependence arises due to changes in the semiconductor properties as the damage disappears during the annealing. For high carrier concentrations, α may be a function of the photocarrier concentration $n(x, t)$. It would be quite complicated to fully account for the effect of the changing material properties. We approximate material properties by some "average" values and the crystal is assumed homogeneous, with the exception of the front surface.

Taking into account surface recombination of the carriers, the boundary conditions are

$$n(x=0, t) = -D \frac{\partial n}{\partial x} \bigg|_{x=0} = v_s (n(0) - n_0) \quad (4)$$

and

$$n(x=l) = n_0. \quad (5)$$

where v_s is the surface recombination velocity and l is the semiconductor thickness. Equations (4) and (5) correspond to a finite flux of carriers at the semiconductor front surface, and a constant carrier concentration at the slab back boundary. The initial condition is

$$n(x, t=0) = n_0. \quad (6)$$

In general, if N , α , τ , and D are functions of x and t , Eq.

$$\begin{aligned} \Delta n(x, t) = & \frac{\alpha N_0 \tau}{2(1-L^2\alpha^2)} \left\{ \sum_{\pm} \frac{1+\alpha D/v_s}{\pm 1-L/v_s\tau} \exp(\pm x/L) \operatorname{erf} \left[\pm \frac{x}{(4Dt)^{1/2}} + \left(\frac{t'}{\tau} \right)^{1/2} \right] \right. \\ & + \sum_{\pm} \frac{(\pm 1 + Da/v_s)}{(1 - Da/v_s)} \exp \left(\pm \alpha x - \frac{t'}{\tau} (1 - \alpha^2 L^2) \right) \operatorname{erfc} \left(\pm x/(4Dt')^{1/2} + \alpha (Dt')^{1/2} \right) \\ & \left. + \frac{2(1-L^2\alpha^2)}{(\alpha D/v_s - 1)(1 - v_s^2\tau/D)} \exp \left(-\frac{t'}{\tau} + (t'v_s + x)\frac{v_s}{D} \right) \operatorname{erfc} \left[v_s \left(\frac{t'}{D} \right)^{1/2} + \frac{x}{(4Dt')^{1/2}} \right] \right\}. \end{aligned} \quad (8)$$

where $t_0 = \max(0, t - t_p)$, the diffusion length $L = (D\tau)^{1/2}$, and $\operatorname{erf}(z)$ and $\operatorname{erfc}(z)$ are error and complementary error functions, respectively. Equation (8) is evaluated between the indicated upper and lower boundaries, t and t_0 , respectively. $n(x, t)$ appears as a source term in the thermal diffusion equation discussed in Sec. II B.

B. Thermal transport

The temperature distribution in the semiconductor after the application of the laser pulse is obtained by solving the thermal equation,

$$\frac{\partial T}{\partial t} - \frac{\partial}{\partial x} \left(\frac{\kappa}{c_p} \frac{\partial T}{\partial x} \right) = \frac{S(x, t)}{c_p}, \quad (9)$$

where c_p and κ are the specific heat and thermal conductivity, respectively, and where the source function S is the heat flux deposited in the semiconductor lattice per unit length. Equation (9) is solved subject to appropriate boundary conditions. In many instances, these are (i) initial temperature, (ii) thermal flux at the front surface, and (iii) thermal flux or temperature of the heat sink at the back of the sample.

1. Lightly damaged materials

Following our previous discussion, we express S as a summation of three terms, S_1 , S_2 , and S_3 . S_1 is the "excess" portion of the electron energy, S_2 is the band-gap portion of the electron energy, and S_3 is energy released by carriers recombined at the semiconductor surface.

The excess portion of the electron energy is released during quasithermalization of photoexcited electrons inside the conduction band. Since the characteristic frequency, 10^{12} – 10^{13} sec $^{-1}$, is much faster¹¹ than any other rate in the problem, we approximate

$$S_1(x, t) = (h\nu - E_g) \alpha N(t) \exp(-\alpha x), \quad (10)$$

where ν is the laser frequency and E_g is the band-gap energy.

The energy-gap portion of the electron energy is transferred to heat at rate τ_0^{-1} , where τ_0 is the nonradiative lifetime of the electron,

(1) has to be solved numerically. However, Eq. (1) can be solved exactly analytically for the special case when α , τ , and D are constants, and the generation function $N(t)$ is a square-shaped laser pulse,

$$N(t) = N_0, \quad 0 < t < t_p, \\ = 0, \quad \text{otherwise.} \quad (7)$$

In Eq. (7), t_p is the length of the laser pulse and N_0 is the number (constant) of arriving photons at the semiconductor front surface. The mathematical methods are discussed in the Appendix. The result is

$$S_2(x, t) \approx E_g \frac{n(x, t) - n_0}{\tau_0}. \quad (11)$$

The surface recombination contributes a term

$$S_3(x, t) = E_g v_s (n(x, t) - n_0) \delta(x), \quad (12)$$

where $\delta(x)$ is the delta function. Mathematically, the effect of $S_3(x, t)$ will be to introduce a finite derivative $\partial T/\partial x$ at $x=0$; see Eq. (14) in what follows.

Similarly as for the electron diffusion, we consider an essentially uniform crystal. It is worth noticing, however, that the effect of the presence of localized carrier "sinks" in the crystal on temperature could be included through source terms of the type of Eq. (12) (which in turn introduce discontinuities in $\partial T/\partial x$). Physically, this corresponds to a localized deposition of the energy, and a subsequent formation of thermal spikes at defect sites. This makes dissolution of localized defects feasible. In this sense, location $x=0$ of this paper may be viewed as a defect site, with the recombination rate for the carriers equal to $v_s \Delta n(x, t) \delta(x)$.

Neglecting loss of heat radiated from the front surface (it has been estimated to be typically six orders of magnitude smaller than the incoming laser flux), Eq. (9) is then solved subject to the following initial and boundary conditions:

$$T(x, t=0) = T_0, \quad (13)$$

$$\frac{\partial T(x=0, t)}{\partial x} = -\frac{E_g}{\kappa} v_s (n(0, t) - n_0), \quad (14)$$

$$T(x=l, t) = T_0, \quad (15)$$

where T_0 is the temperature of the heat sink at the back of the sample. Equation (14) was obtained by substituting Eq. (12) into Eq. (9) and integrating the resulting equation across the front boundary. Equation (9) has to be solved numerically.

2. Heavily damaged materials and κ and c_p are constants

For heavily damaged materials and κ , $c_p = \text{const}$, Eq. (9) has a closed-form solution. This is because for extremely short carrier lifetimes, $\tau v_s \alpha < 1$ and $\tau D \alpha^2 < 1$ (i.e., bulk recombination is faster than either the surface recombination or carrier diffusion), the source functions simplify to

TABLE I. The values of the material and laser parameters used in the calculations

	Damage	τ (sec)	D (cm ² sec ⁻¹)	v (cm/sec)	c_p (J/cm ³)	Ruby	α (cm ⁻¹) Nd : YAG	t (nsec)
GaAs	Good quality to amorphized	10^{-8} – 10^{-11}	200–15	0– 10^3	1.78	2×10^4	N A	10
Si	Good quality to amorphized	10^{-6} – 10^{-11}	30–3	0– 10^3	1.6	2×10^4 – 2×10^5	100– 10^3	100

$$S_2(x, t) = E_g \frac{n(x, t) - n_0}{\tau} \approx E_g g = E_g \alpha F(t) \exp(-\alpha x) \quad (16)$$

and

$$S_1(x, t) \approx 0. \quad (17)$$

This yields the source term

$$S \approx S_1 + S_2 = h\nu \alpha N(t) \exp(-\alpha x) \quad (18)$$

and the boundary condition

$$\frac{\partial T(x=0, t)}{\partial x} = 0. \quad (19)$$

The solution to Eq. (9) is then obtained by taking the limit $1/\tau \rightarrow 0$ in Eq. (A10) of the Appendix. This yields

$$\begin{aligned} \Delta T(x, t) = & \frac{F_0}{2\alpha\kappa} \left\{ \exp\left(\frac{\kappa}{c_p} \alpha^2 t'\right) \sum_{i=1}^{\infty} \exp(\pm \alpha x) \right. \\ & \times \operatorname{erfc}\left[\alpha \left(\frac{\kappa t'}{c_p}\right)^{1/2} \pm \frac{x}{[(4\kappa/c_p)t']^{1/2}}\right] \\ & + 4\alpha \left(\frac{\kappa t'}{c_p}\right)^{1/2} \exp\left(\frac{-x^2}{(4\kappa/c_p)t'}\right) \\ & \left. + 2\alpha x \operatorname{erf}\left(\frac{x}{[(4\kappa/c_p)t']^{1/2}}\right) \right\}, \quad (20) \end{aligned}$$

where $F_0 = h\nu N_0$, and the upper and lower boundaries are $t' = t$ and $t_0 = \max(0, t - t_p)$, respectively.

III. NUMERICAL RESULTS

Equation (9) was solved numerically for ruby and Nd : YAG lasers, GaAs, and silicon. The material parameters used ranged from those appropriate for heavily damaged materials to those corresponding to high-quality materials. The values of these parameters are summarized in Table I. The thermal conductivity $\kappa(T)$ was represented by a summation of exponentials chosen to fit data measured for pure GaAs and silicon.¹² The carrier lifetimes were taken as $\tau = \tau_0$. The laser pulse lengths used (10 nsec for ruby and 100 nsec for Nd : YAG laser) are the optimum pulse lengths for heavily damaged materials.

Samples of the numerical results are shown in Figs. 1–12. The profiles are shown as a function of the normalized distance αx away from the semiconductor front surface, with time (in fractions and multiples of the pulse length t_p) as a parameter. The symbols shown (in cgs units unless specified otherwise) have their usual meaning. The normalized temperature $(T - T_0)(F_0/\kappa_0\alpha)^{-1}$ is dimensionless, κ_0 is a

quantity (equal to unity) which has the dimension of thermal conductivity. F_0 is the actual absorbed power (in W/cm²). The profiles shown correspond to $\Delta T_{\max} \approx 900$ – 1300 °C (just below the melting), the exact number can be calculated from parameters specified in each figure. Before inspecting the profiles, it is convenient to qualitatively summarize the main results of these calculations. This will aid understanding when inspecting the profiles.

A. Heavily damaged materials

For heavily damaged materials, the effects of carrier diffusion and surface recombination on heat generation can be neglected. The simulated profiles approached those calculated using Eq. (20) [Eq. (20) assumes $\kappa = \text{const}$, $\tau_0 D < 1$, and $\tau_0 D \alpha^2 < 1$]. As compared to Eq. (20), the effect of $\kappa = \kappa(T)$ on the profiles was to slightly increase the surface temperature and narrow the profile width. This is because $\kappa(T)$ decreases with increasing temperature.

1. Surface temperature and profile width

For the pulse length shorter than the thermal diffusion time, $t_p < t_{th}$, where $t_{th} = c_p/\kappa\alpha^2$, the profiles are optical absorption depth limited. The profile width $\approx \alpha^{-1}$, and ΔT_{\max} grows linearly with both the pulse length and optical absorption coefficient, $\Delta T_{\max} \approx F_0 \alpha/c_p$. For the pulse length longer than t_{th} , $t_p > t_{th}$, the profile is thermal diffusion limited. Its width is $\approx (\kappa t_p/c_p)^{1/2}$, and ΔT_{\max} is independent of α and proportional to the square root of the pulse length, $T_{\max} \approx F_0(t_p/\kappa c_p)^{1/2}$ (the surface temperature approaches saturation for extremely long pulses). In either case, ΔT_{\max} is approximately linear with pulse peak power (ΔT_{\max} is exactly linear with F_0 for $\kappa = \text{const}$). The heating is most efficient (least laser energy required) when $t_p \approx t_{th}$. The optical depth-limited profiles are generally narrower than the thermal diffusion-limited profiles.

2. Temperature decay

After the end of the laser pulse, the temperature drops and the profile broadens as the heat propagates into the bulk. The decay is much faster for strong absorption than for weak absorption. This is because the thermal diffusion time $c_p/\kappa\alpha^2$ is much longer for small α than for large α . For example, for $\alpha = 2 \times 10^3$ cm⁻¹, the surface temperature typically dropped to one-half of its maximum value at $t \approx 100\tau_0$. For $\alpha = 2 \times 10^4$ cm⁻¹, the half-time was only $t \approx 5\tau_0$.

For comparison purposes, Eq. (9) was, for heavily damaged materials, also solved for the "Gaussian" pulse shapes. We have observed really no significant difference between the shapes of the thermal profiles created by square and Gaussian pulse shapes. The resulting temperature distributions were affected much more by the condition α^{-1} versus $(\kappa t_p / c_p)^{1/2}$ than by the pulse shape. For the Gaussian pulse, slightly higher laser powers were required to achieve the same surface temperature as for the square-shaped pulse. The Gaussian profiles tend to decay more slowly than the square-shaped pulse profiles.

B. Lightly damaged materials

The main effect of carrier diffusion on temperature profiles consists of the following:

(i) Higher laser powers are required to raise the surface temperature of a good-quality material than of a damaged material.

(ii) Temperature profiles in good-quality materials are generally wider than in damaged materials.

(iii) The time (t_m) at which the surface temperature reaches maximum, and time ($t_{1/2}$) required for the surface temperature to drop to one half of its maximum value after the end of the laser pulse, are longer in good-quality materials than in damaged materials.

(iv) The effect of carrier diffusion on temperature profiles is much stronger for Nd : YAG laser than for ruby laser irradiation.

(v) The effect of the "sinking" of the carriers is to produce thermal spikes at the surface and lower temperature in the material interior. For a sufficiently fast surface recombination, the profiles may develop a secondary local maximum in the material interior.

Conclusions (i)-(iv) are the direct consequence of the model used for the transfer of the photon energy to heat. The excess and band-gap portions of the electron energy heat volumes bounded by the depths

$$\sigma_{eg} = \max[\alpha^{-1}, (\kappa t_p / c_p)^{1/2}] \quad (21)$$

and

$$l_{egs} = \max(\sigma_{eg}, L), \quad (22)$$

respectively.

Thus, in good-quality materials where the carrier diffusion length $L > \sigma_{eg}$, the band-gap portion of the energy heats a volume which is larger than the one heated by the excess energy. This results in temperatures which are generally lower (for the same laser power) than those in damaged materials. Furthermore, since both the electron lifetime (τ) and the thermal diffusion time associated with the band-gap portion of the energy

$$t_{thg} = c_p l_{egs}^2 / 4\kappa, \quad (23)$$

may be quite long, the heating times (t_m and $t_{1/2}$) may be substantially longer than t_p . Clearly, the effect of carrier diffusion on the temperature will be greater for Nd : YAG than for ruby laser irradiation. This is because Nd : YAG frequency is very close to the silicon band-gap frequency; the excess portion of the electron energy is $\approx 1\%$. For ruby irradiation of silicon, the excess portion of the electron energy is large, $\approx 35\%$, and is not affected by electron diffusion.

Conclusion (v) is the unique consequence of the surface recombination of the carriers. For $v_s = 0$, the temperature is smooth and monotonically decreasing with the distance away from the surface. This is because both the thermal source S_1 (excess energy) and S_2 (band-gap energy distribution) are also monotonically decreasing, and the surface recombination source $S_3 = 0$. For $v_s \neq 0$, however, the carriers preferentially recombine, and release their energy, at the surface. This leads to the formation of thermal spikes. Furthermore, since the carrier distribution develops a "sink" at the surface, the source $S_2(x)$ will be nonmonotonic. If the maximum of S_2 is sufficiently strong so that also the total $S = S_1 + S_2$ is nonmonotonic, then the resulting thermal distribution may develop a local interior maximum. (We note that all peaks and maxima will eventually disappear with time because of carrier and thermal diffusion.)

Figures 1 and 2 show carrier distributions for silicon, with time (t/t_p) and v_s as parameters. In Fig. 1, the electron lifetime is 10^{-6} sec, in Fig. 2, $\tau = 10^{-7}$ sec. The effect of v_s is clearly seen. The carrier distribution (per unit photon flux) is high and monotonic for $v_s = 0$, lower and nonmonotonic for $v_s \neq 0$. For short τ (Fig. 1), the maximum is sharp and close to the surface. The maximum moves into the material interior with increasing v_s and higher t/t_p . Because of the short τ ($\tau < t_p$), the distribution decays extremely rapidly after the end of the pulse ($t > t_p$). For longer τ ($\tau > t_p$, see Fig. 2), the maximum is much more pronounced. The concentration remains high even when $t > t_p$.

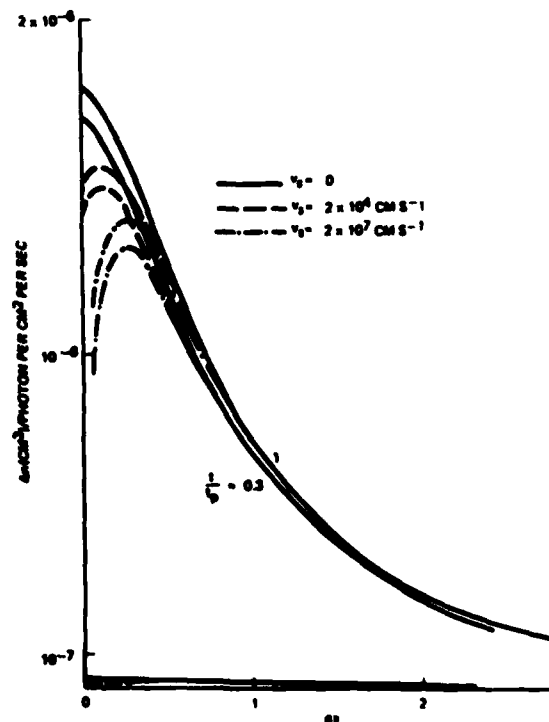


FIG. 1. Photocarrier concentration in ruby-irradiated silicon, $t_p = 10^{-6}$ sec, $\alpha = 2 \times 10^3$ cm $^{-1}$, $\tau = 10^{-6}$ sec, $D = 3$ cm 2 sec $^{-1}$. For $t = 0$, $n(x,t)$ is nonmonotonic. Since $\tau < t_p$, $n(x,t)$ decays rapidly after $t = t_p$.

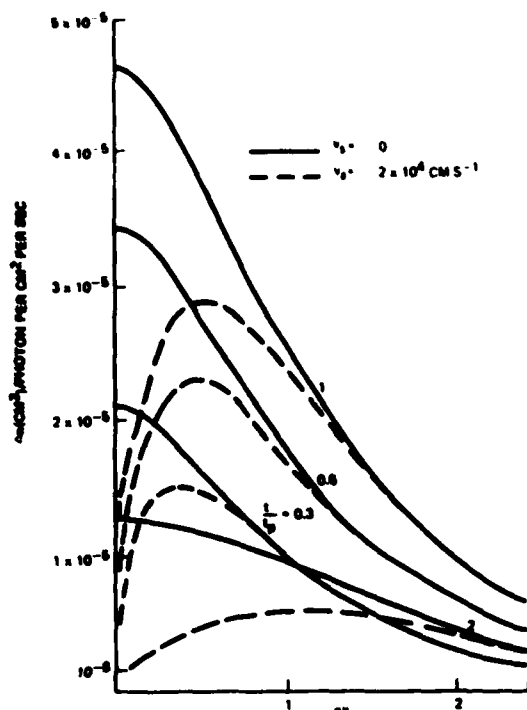


FIG. 2. Photocarrier concentration in Nd:YAG-irradiated silicon, $t_p = 10^{-7}$ sec, $\alpha = 10^3$ cm $^{-1}$, $\tau = 10^{-8}$ sec, $D = 3$ cm 2 sec $^{-1}$. For $v_0 \neq 0$, $n(x,t)$ is nonmonotonic. Since $\tau \approx t_p$, $n(x,t)$ is still high at $t = t_p$.

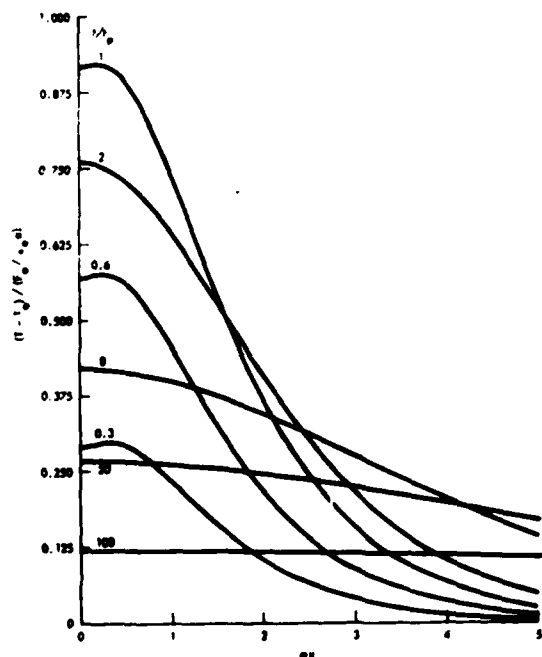


FIG. 3. Temperature for ruby irradiation of heavily damaged GaAs: $\tau = 10^{-11}$ sec, $D = 15$ cm 2 sec $^{-1}$, $v_0 = 2 \times 10^7$ cm sec $^{-1}$, $\alpha = 2 \times 10^4$ cm $^{-1}$, $t_p = 10^{-8}$ sec, $F_0 = 2 \times 10^7$ W/cm 2 .

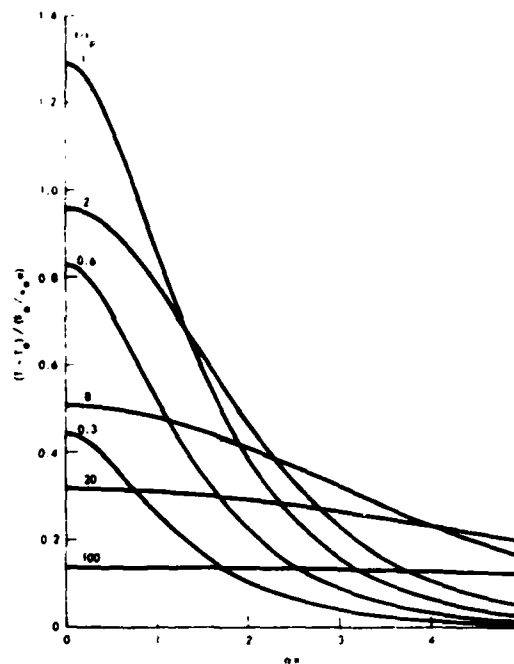


FIG. 4. Temperature for ruby irradiation of heavily damaged GaAs: $\tau = 10^{-11}$ sec, $D = 15$ cm 2 sec $^{-1}$, $v_0 = 2 \times 10^4$ cm sec $^{-1}$, $\alpha = 2 \times 10^4$ cm $^{-1}$, $t_p = 10^{-8}$ sec, $F_0 = 2 \times 10^7$ W/cm 2 .

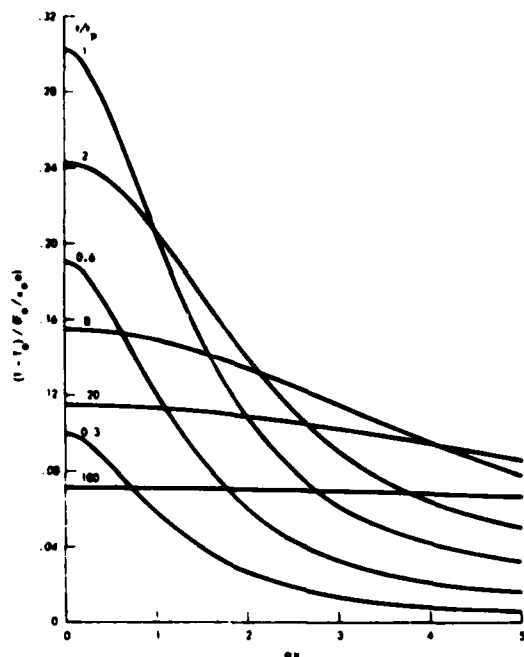
Inspection of Figs. 3–12 reveals the qualitative features discussed above.

1. Ruby irradiation of GaAs

Figures 3–5 show temperature distributions for ruby laser irradiation of GaAs. Figures 3 and 4 show the effect of v_0 . The principal effect of large v_0 in GaAs is to lower the surface temperature. For the same laser input, the surface temperature obtained for $v_0 = 2 \times 10^4$ cm sec $^{-1}$ is higher (by $\approx 50\%$) than the temperature obtained for $v_0 = 2 \times 10^7$ cm sec $^{-1}$. Figures 4 and 5 compare temperature distributions for heavily damaged and good-quality GaAs. The principal effect of the electron diffusion is to increase the laser power required for heating good-quality material in Fig. 5, approximately by $(1 - E_g/h\nu)^{-1} \approx 5$ (for the same α). Its effect on the width of the profiles is negligible; the widths of profiles shown in Figs. 4 and 5 are practically identical. This is because in good-quality material, the band-gap energy (80% of the photon energy) is distributed into the depth $L \approx 3 \times 10^{-1}$ cm, which is much larger (by nearly two orders of magnitude) than the depth for the excess energy (20%), $\alpha^{-1} \approx 5 \times 10^{-3}$ cm. This makes the band-gap portion of the energy ineffective for the heating. We should note that for intermediately damaged GaAs, more of the available power will be used for the heating, and for $\alpha^{-1} \approx L$, the profiles will be somewhat wider than in either the heavily damaged or high-quality materials.

2. Ruby irradiation of silicon

Temperature profiles in amorphous silicon are very



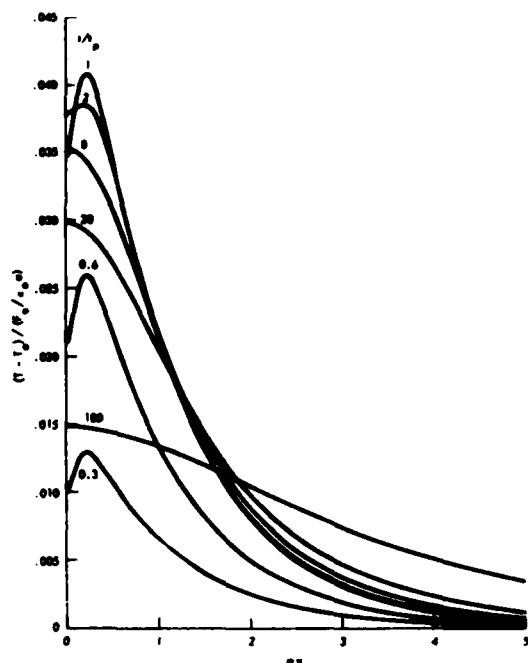


FIG. 8. Temperature for Nd:YAG irradiation of damaged silicon: $\tau = 10^{-8}$ sec, $D = 3$ cm² sec⁻¹, $v_1 = 2 \times 10^7$ cm sec⁻¹, $\alpha = 10^3$ cm⁻¹, $t_p = 10^{-7}$ sec, $F_0 = 2.5 \times 10^7$ W/cm².

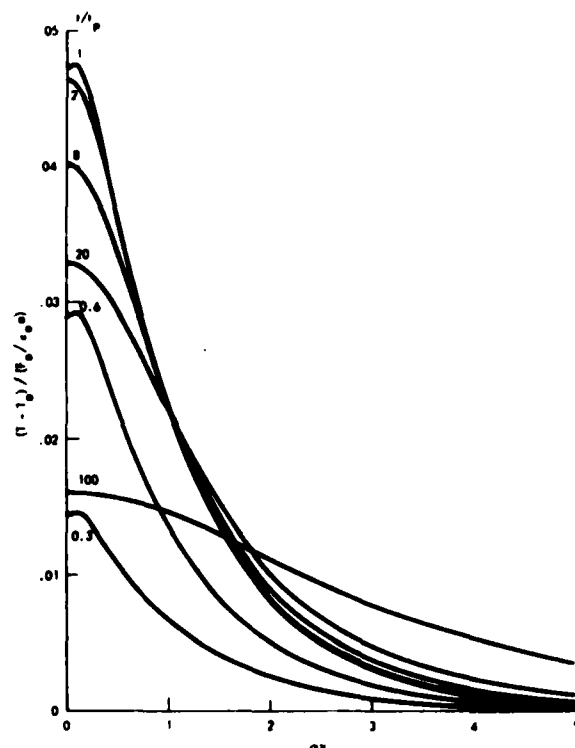


FIG. 9. Temperature for Nd:YAG irradiation of damaged silicon: $\tau = 10^{-8}$ sec, $D = 3$ cm² sec⁻¹, $v_1 = 2 \times 10^4$ cm sec⁻¹, $\alpha = 10^3$ cm⁻¹, $t_p = 10^{-7}$ sec, $F_0 = 2.5 \times 10^7$ W/cm².

and 2×10^4 cm sec⁻¹ in Figs. 8 and 9, respectively. The half-widths are $\approx \alpha^{-1} > L$ in both cases. The primary effect of slow v_1 ($v_1 < L$) in Fig. 9 is to suppress the interior maximum appearing in Fig. 8 for large v_1 . There should be a sharp peak at the surface in Fig. 8 for large v_1 . The peak is unresolved because of the numerical limitations. The peak corresponds to thermal spikes (discussed earlier), created at $x = 0$ as the result of the preferential deposition of the carrier energy at the surface.

As has already been discussed, the occurrence of thermal spikes and local interior maxima (the local maximum is always lower than the spike) is the consequence of fast surface recombination. By inspecting the simulated profiles, a nonmonotonic $T(x)$ occurs for v_1 sufficiently large, $v_1 \tau > L$ [so that maximum in $n(x, t)$ is large and separated from the surface], τ not too short (so that the energy does not relax instantaneously), α^{-1} not too small, $\alpha^{-1} \gtrsim L$ (so that the band-gap energy is not dissipated into too large a volume), and the excess portion of the energy not too large compared to the band-gap energy [so that the source term $S_1(x)$ does not suppress the peak in $S_2(x)$]. If these conditions are satisfied, $T(x)$ becomes nonmonotonic, with a sharp spike at the surface and a local maximum at the distance $0 < x < L$. The magnitude of the spike can be estimated by using the energy conservation arguments. For example, noticing that the energy carried by carriers recombined at the surface must be equal to the heat contained in the spike, we obtain that in the limit of rapid v_1 , short τ , and large α , the height of the spike is on the order of $\Delta T_{\text{peak}} \approx \alpha \tau F_0 (v_1 l_i / \kappa \epsilon_p)^{1/2}$, where l_i is the characteristic length associated with the position of the maxi-

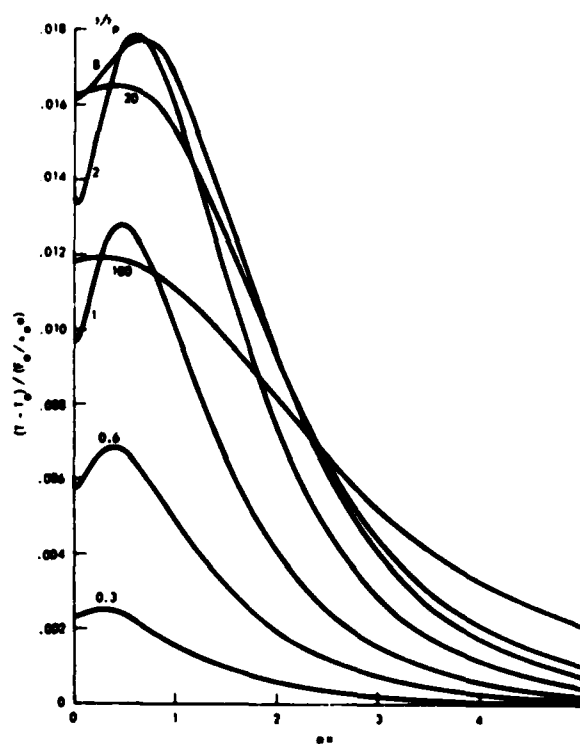


FIG. 10. Temperature for Nd:YAG irradiation of silicon: $\tau = 10^{-8}$ sec, $D = 3$ cm² sec⁻¹, $v_1 = 2 \times 10^4$ cm sec⁻¹, $\alpha = 10^3$ cm⁻¹, $t_p = 10^{-7}$ sec, $F_0 = 7 \times 10^7$ W/cm².

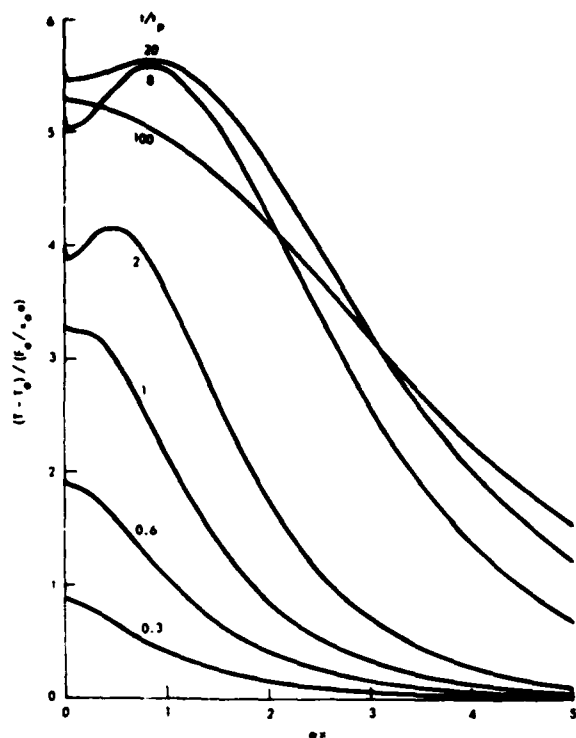


FIG. 11. Temperature for Nd:YAG irradiation of silicon: $\tau = 10^{-6}$ sec, $D = 3 \text{ cm}^2 \text{ sec}^{-1}$, $v_s = 2 \times 10^4 \text{ cm sec}^{-1}$, $\alpha = 10^3 \text{ cm}^{-1}$, $t_p = 10^{-7}$ sec, $F_0 = 2 \times 10^6 \text{ W/cm}^2$.

imum in $\Delta n(x, t)$. For typical parameters of interest, this yields $\Delta T_{\text{peak}} \approx \text{several } 10^3 \text{ K}$ and spike characteristic width $l_p \approx (l_s \kappa / c_p v_s)^{1/2} \approx 10^{-6} \text{ cm}$. The local maximum will initially move deeper into the bulk (with the diffusing carriers) until it eventually disappears, with the characteristic time $t = \max[\tau, t_p, (c_p / 4\kappa) L^2]$.

Figure 10 corresponds to light-to-intermediately damaged material ($\alpha \approx 10^3 \text{ cm}^{-1}$, $\tau \approx 10^{-7} \text{ sec}$). The development of nonmonotonic $\Delta T(x, t)$ is clearly seen (again, there should be a spike at $x = 0$). The temperature becomes monotonic at times $t \gtrsim t_{\text{th}, \alpha} \approx (c_p / 4\kappa) L^2 \approx 10^{-6} \text{ sec}$. Because of the long τ , the required power is about twice higher than the one for the heavily damaged material in Fig. 9 (for otherwise the same parameters). Figures 11 and 12 show the effect of the electron diffusivity D on the profiles. The main effect of increasing D (at constant τ , $\tau = 10^{-6} \text{ sec}$) is to suppress the interior maximum. Because of the long τ , the heating times are very long, the temperature is high even at time $t \gtrsim 100\tau$.

We have also simulated profiles for $\alpha = 100$ and 500 cm^{-1} . On the scaled distances ax , the shapes of the profiles were qualitatively similar to those calculated for $\alpha = 10^3 \text{ cm}^{-1}$. The required powers were also much higher (approximately by the ratio of α 's and the heating times accordingly longer [as determined by the thermal time $(c_p / 4\kappa) L^2$, see Eq. (23)].

IV. DISCUSSION

In order to facilitate a more comprehensive under-

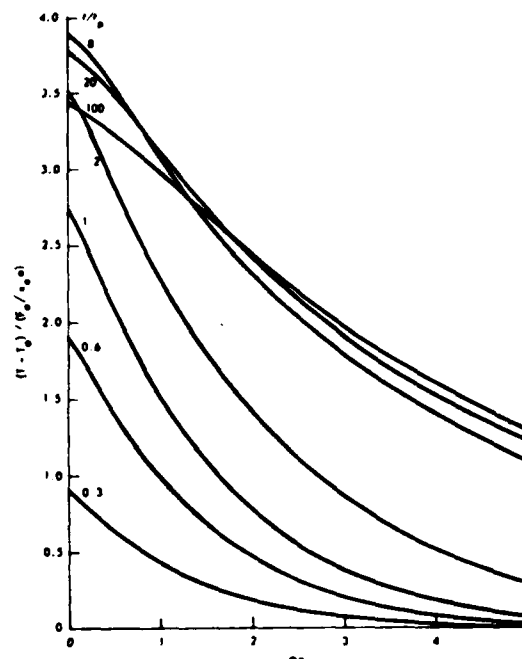


FIG. 12. Temperature for Nd:YAG irradiation of silicon: $\tau = 10^{-6}$ sec, $D = 30 \text{ cm}^2 \text{ sec}^{-1}$, $v_s = 2 \times 10^4 \text{ cm sec}^{-1}$, $\alpha = 10^3 \text{ cm}^{-1}$, $t_p = 10^{-7}$ sec, $F_0 = 2.5 \times 10^6 \text{ W/cm}^2$.

standing of our results, Figs. 13 and 14 show the derived dependence of (i) pulse energy (Q) required to raise the surface temperature by $\Delta T \approx 1400^\circ \text{C}$, (ii) time at which the surface temperature reaches its maximum (t_m), and (iii) time at which the temperature drops to one-half of its maximum value ($t_{1/2}$), on the quality of the processed material (silicon

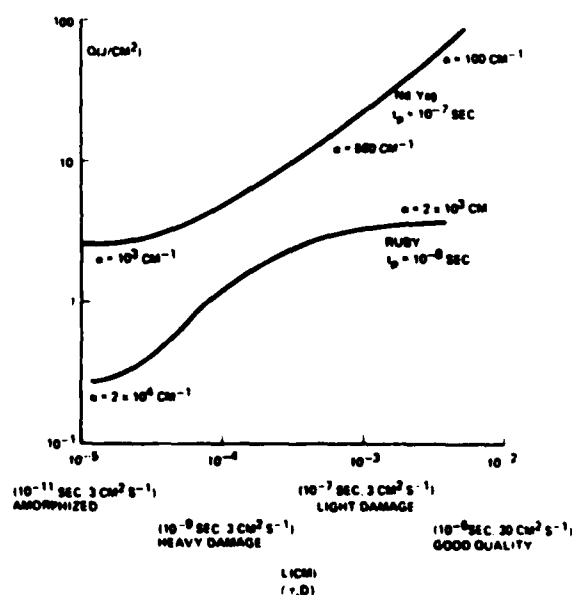


FIG. 13. Laser energy (Q) required to heat the silicon surface just below the melting temperature Nd:YAG $t_p = 10^{-7}$ sec, ruby $t_p = 10^{-8}$ sec.

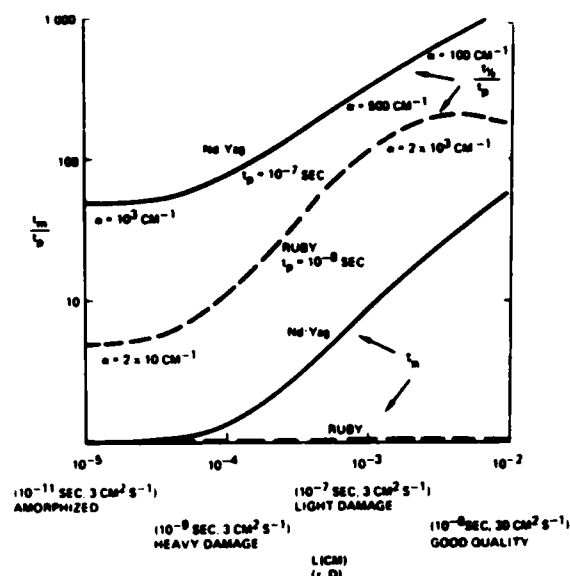


FIG. 14. The dependence of (i) time at which the surface temperature reaches the maximum (t_m); (ii) time when the surface temperature decays to one-half of its maximum value ($t_{1/2}$), on material quality (silicon).

only). The quality is characterized in terms of the electron diffusion length L (the corresponding values of τ and D and α are also indicated). Q ($Q \approx F t_p$) is the actually absorbed energy; the incident energy is nearly twice as high as the absorbed energy because of material reflection. We emphasize once again that the values of the material parameters are some "average" representative values (this is true particularly for the values of α for Nd : YAG irradiation of silicon), and thus the derived quantities are very approximate. The results can be generalized to different laser parameters.

A. Ruby in silicon

The required energy increases with L increasing, from about $Q \approx 0.25$ J for amorphous to $Q \approx 4$ J for good-quality material. Only the excess portion of the energy is operative for heating of the quality material ($E_r/h\nu \approx 65\%$), and, therefore, Q saturates at long L ; this is seen in Fig. 13. With the α 's and t_p used, the heated volume is thermal diffusion dominated for amorphous material and optical absorption depth limited for good-quality material. The surface temperature reaches maximum at $t_m = t_p$. The effect of the band-gap portion of the energy is to slow down the temperature decay in lightly damaged materials. At intermediate values of L , $L \gtrsim \alpha^{-1}$, the temperature remains high up to the time $(c_p/4\kappa)L^2$ (i.e., $t_{1/2} = \tau$). At very long L ($L \gg \alpha^{-1}$), however, the band-gap energy is dissipated into an extremely large volume (depth \approx several L), so that its effect on temperature becomes insignificant. The temperature starts to decay more rapidly. The decrease in $t_{1/2}$ is seen in Fig. 14 for $L \gtrsim 5 \times 10^{-4}$ cm.

B. Nd : YAG in silicon

The heating is nearly entirely band-gap energy domi-

nated. For amorphous and damaged materials, the optical absorption depth $\alpha^{-1} > (\sigma_{th} L)$ and the profile width is therefore $\approx \alpha^{-1}$, unaffected by the diffusion. The surface temperature is $\Delta T_{max} \approx Q\alpha/c_p$. In good-quality material, L becomes $\gtrsim 10^{-2}$ cm. This is larger than the probable value of α^{-1} in the material, $\alpha^{-1} \approx 2 \times 10^{-3}$ cm for lightly damaged, and $\alpha^{-1} \approx 10^{-2}$ cm for good-quality material. Therefore, the depth of the heated volume is $\approx L$, and the power required to heat the material increases accordingly. In Fig. 13, Q increases at long L with L approximately linearly.

Because the heating is band-gap energy dominated, T_{max} is obtained in good-quality materials at times on the order of several τ ($t_m \approx t_p$ in amorphous and heavily damaged material). The decay of the surface temperature is determined by the thermal diffusion time $t_{th,g}$ ($t_{1/2} \approx t_{th,g} = \max[(c_p/4\kappa)L^2, (c_p/4\kappa)(1/\alpha^2), t_p]$). Since the thickness of the heated region increases with L increasing, there is no saturation of $t_{1/2}$ at long L which has been observed for ruby irradiation of silicon.

In summary, we have investigated in this work the influence of the diffusion of the photoexcited carriers on laser heating of strongly absorbing semiconductors. The diffusion was found to increase the powers required to heat good-quality materials and to prolong the heating times. Surface recombination was found to create thermal spikes at the surface. The profiles could become nonmonotonic as the consequence of the interplay of surface recombination and diffusion of the photoexcited carriers. The strength of the spike was estimated from energy arguments.

In practice, the existence of the thermal spikes may be of importance for annealing of localized defects. For a sufficiently strong spike, it is qualitatively feasible for the heat to dissolve the defect. This results in localized defect removal. For practical utilization, further analyses are desirable. This is because of the effect of both the finite size (e.g., finite thickness of the surface "dead layer"), and spatial distribution, of the defects on the temperature profiles. Further effects, not considered here, include other energy "diffusion" mechanisms (such as radiative recombination of the carriers), non-equilibrium effects, and distributed damage such as that created during ion implantation. The damaged regions have different optical, thermal, and electronic properties than the rest of the material (they often absorb the radiation more strongly). Furthermore, as the damage disappears, material properties change during the processing. This was not taken into account here; in the model used, with the exception of the front surface, the material was assumed homogeneous, and its properties independent of time. Further analyses are being planned to account for these effects.

ACKNOWLEDGMENTS

The author wishes to thank Dr. R.S. Witte, Dr. S. Prussin, Dr. W. von der Ohe, and Dr. L. Heflinger for technical discussions concerning the laser annealing; Dr. P. Molmud and Dr. T.J. Wilcox for mathematical discussions, and R. Lipkis for her help in computer calculations. This work was supported in part by DARPA Contract MDA903-78-C-0284.

APPENDIX A: ELECTRON TRANSPORT EQUATION: SOLUTION BY LAPLACE TRANSFORM TECHNIQUE

Problem

The diffusion equation we want to solve is

$$\frac{\partial n}{\partial t} = \alpha F(t) \exp(-\alpha x) - \frac{(n - n_0)}{\tau} + D \frac{\partial^2 n}{\partial x^2}. \quad (\text{A1})$$

We consider constant α , τ , and D , and a square-shaped generation function $F(t)$:

$$F(t) = F_0, \quad 0 < t < t_p \\ = 0, \quad \text{otherwise.} \quad (\text{A2})$$

The boundary conditions are

$$D \frac{\partial n}{\partial x} \Big|_{x=0} = v_s (n(0, t) - n_0) \quad (\text{A3})$$

for the front surface and

$$n(x = l) = n_0 \quad (\text{A4})$$

for the back surface.

The initial condition is

$$n(x, t = 0) = n_0. \quad (\text{A5})$$

Equation (A1) is a linear partial differential equation for $n(x, t)$. For $v_s = 0$, Eq. (A1) can be solved by using the Green's function technique. For $v_s \neq 0$, it is solved by using the Laplace transform technique. In using the Laplace transforms, advantage is taken of the knowledge of the steady-state solution to Eq. (A1).

Case $v_s = 0$: Green's function technique

For $v_s = 0$, Green's function is

$$G(x, x', t - t') = \frac{1}{[4\pi D(t - t')]^{1/2}} \sum_{n=-\infty}^{\infty} (-1)^n \exp\left(-\frac{t}{\tau}\right) \\ \times \left[\exp\left(-\frac{(x - x' - 2nl)^2}{4D(t - t')}\right) + \exp\left(-\frac{(x + x' - 2nl)^2}{4D(t - t')}\right) \right], \quad (\text{A6})$$

and $\Delta n \equiv n(x, t) - n_0$ is

$$\Delta n(x, t) = \int_0^x dx' \int_0^{t'} G(x, x', t - t') \alpha F_0 \exp(-\alpha x) dt'. \quad (\text{A7})$$

Assuming the slab thickness $l \gg \alpha^{-1}$, the semiconductor can be replaced by a semi-infinite medium, with the result that the summation \sum_n in Eq. (A6) reduces to only one term, namely, the term $n = 0$. Substituting the resulting equation into Eq. (A7) and integrating it over coordinate x yields

$$\Delta n(x, t) = \frac{\alpha F_0}{2} \sum_{\pm} \exp(\pm \alpha x) \int_0^{t'} dt' \\ \times \exp\left(-\frac{t'}{\tau} (1 - \alpha^2 L^2)\right) \\ \times \operatorname{erfc}\left(\frac{\pm x + 2\alpha D t'}{2(D t')^{1/2}}\right), \quad (\text{A8})$$

where $L = (D\tau)^{1/2}$, $\operatorname{erfc}(z)$ is the complementary error function, and the integral lower boundary t_0 is

$$t_0 = 0, \quad t < t_p, \\ t_0 = t - t_p, \quad t > t_p. \quad (\text{A9})$$

Integral (A8) is evaluated by using the partial fraction.

This yields

$$\Delta n(x, t) = \frac{\alpha \tau F_0}{2(\alpha^2 L^2 - 1)} \sum_{\pm} \exp(\pm \alpha x) \left[\exp\left(-\frac{t'}{\tau} (1 - \alpha^2 L^2)\right) \operatorname{erfc}\left(\frac{\pm x + 2\alpha D t'}{2(D t')^{1/2}}\right) \right]' \\ + \frac{2}{\pi^{1/2}} \int_0^{t'} dt' \exp\left(-\frac{t'}{\tau} (1 - \alpha^2 L^2)\right) \exp(\pm \alpha x) \left(\pm \frac{x}{4D^{1/2} t'^{3/2}} + \frac{\alpha D^{1/2}}{2(t')^{1/2}} \exp\left[-\left(\frac{x^2}{4D t'} + \alpha^2 D t'\right)\right] \right) \quad (\text{A10})$$

The second term on the right-hand side of Eq. (A10) is evaluated by using the following change of variables:

$$t = z^2 \quad \text{and} \quad t' = z'^2 \quad (\text{A11})$$

for the first and second term under the integral sign, respectively. Performing the change of the variables, each of the two terms transforms into an expression of the type ($a \neq 0$)

$$\int \exp\left(-a^2 z^2 - \frac{b^2}{z^2}\right) dz = \frac{\pi^{1/2}}{4a} \sum_{\pm} \exp(\pm 2ab) \operatorname{erf}\left(az \pm \frac{b}{z}\right) + \text{const.} \quad (\text{A12})$$

Collecting the resulting terms completes the calculation. The final result is

$$\Delta n(x, t) = \frac{\alpha \tau F_0}{2(\alpha^2 L^2 - 1)} \left[\exp\left(-\frac{(1 - L^2 \alpha^2) t'}{\tau}\right) \sum_{\pm} \exp(\pm \alpha x) \operatorname{erfc}\left(\alpha(D t')^{1/2} \pm \frac{x}{(4D t')^{1/2}}\right) \right]' \\ + \alpha L \sum_{\pm} \exp\left(\pm \frac{x}{L}\right) \operatorname{erf}\left[\left(\frac{t'}{\tau}\right)^{1/2} \pm \frac{x}{(4D t')^{1/2}}\right] \quad (\text{A13})$$

Case $v_s \neq 0$: Laplace transform technique

Since the steady-state solution to Eq. (A1) is known, Eq. (A1) is Laplace transformed with respect to time. One obtains [for the square-shaped $F(t)$]

$$\frac{\alpha F_0}{s} \exp(-\alpha x) [1 - \exp(-\alpha t_p)] - \left(s + \frac{1}{\tau}\right) \Delta \bar{n}(x, s) + D \frac{\partial^2 \bar{n}(x, s)}{\partial x^2} = 0, \quad (\text{A14})$$

where $\bar{n}(x, s)$ is the Laplace transform of $n(x, t)$. The solution of Eq. (A14) is

$$\Delta \bar{n}(x, s) = \frac{\alpha F_0 \tau}{s} \frac{1 - \exp(-st_p)}{1 + s\tau - \alpha^2 L^2} \left[\exp(-\alpha x) - \frac{v_s + \alpha D}{v_s + [D(1/\tau + s)]^{1/2}} \exp\left(-\frac{x}{L}(1 + s\tau)^{1/2}\right) \right]. \quad (\text{A15})$$

The reverse Laplace transform is easiest to find by using the well-known results for the partial expressions appearing in Eq. (A15), and making time convolutions of the partial Laplace transforms. That is,

$$F(t) = \int_0^t F_1(t-t') F_2(t') dt', \quad (\text{A16})$$

where

$$\bar{f}_1(s) \rightarrow F_1(t), \quad \bar{f}_2(s) \rightarrow F_2(t), \quad \bar{f}_1(s) \bar{f}_2(s) \rightarrow F(t), \quad \bar{f}(s+c) \rightarrow F(t) \exp(-ct), \quad \bar{f}(as) \rightarrow \frac{1}{a} F\left(\frac{t}{a}\right).$$

The partial transform used in evaluating the inverse Laplace transform of Eq. (A15) are of the type

$$\frac{\exp(-as)}{s(s+b)} \rightarrow \begin{cases} \frac{1}{b} [1 - \exp(-b(t-a))] H(t-a), & a > 0 \\ \frac{1}{b} [1 - \exp(-bt)], & a < 0 \end{cases} \quad (\text{A17})$$

and

$$\frac{\exp(-as^{1/2})}{b + s^{1/2}} \rightarrow \frac{1}{(\pi t)^{1/2}} \exp\left(-\frac{a^2}{4t}\right) - b \exp(ab + b^2 t) \operatorname{erfc}\left(\frac{a}{2t^{1/2}} + bt^{1/2}\right). \quad (\text{A18})$$

In Eq. (A17), $H(t)$ is the step function. $H(t) = 1$ for $t > 0$ and zero otherwise.

Using Eqs. (A16)–(A18), the inverse transform of Eq. (A15) is

$$\begin{aligned} \Delta n(x, t) = & \frac{\alpha \tau F_0}{1 - \alpha^2 L^2} \left(\exp(-\alpha x) \left[1 - \exp\left(-\frac{t'}{\tau}(1 - \alpha^2 L^2)\right) \right] \right)' \\ & - \frac{(v_s + \alpha D)}{D} \int_0^t \exp\left(-\frac{t'}{\tau}\right) \\ & \times \left\{ \left(\frac{D}{\pi t'} \right)^{1/2} \exp\left(-\frac{x^2}{4Dt'}\right) - v_s \exp\left(\frac{v_s}{D}(x + v_s t')\right) \operatorname{erfc}\left[\frac{x}{(4Dt')^{1/2}} + v_s \left(\frac{t'}{D}\right)^{1/2}\right] \right\} \\ & \times \left[1 - \exp\left(-\frac{t-t'}{\tau}(1 - \alpha^2 L^2)\right) - \left[1 - \exp\left(-\frac{(t-t'-t_p)}{\tau}(1 - \alpha^2 L^2)\right) \right] H(t-t'-t_p) \right] dt'. \quad (\text{A19}) \end{aligned}$$

Integral (A19) is evaluated by using the same changes of variables as those used for evaluation of integrals in the Green's function expression, Eq. (A8) and the following discussion. It is convenient to rewrite Eq. (A19) in the form

$$\begin{aligned} \Delta n(x, t) = & \frac{\alpha \tau F_0}{1 - \alpha^2 L^2} \left(-\exp(-\alpha x) \exp\left(-\frac{t'}{\tau}(1 - \alpha^2 L^2)\right) \right)' - \frac{(v_s + \alpha D)}{D} \\ & \times \int_0^t f(t') \left[1 - g(t') \exp\left(-\frac{t'}{\tau}(1 - \alpha^2 L^2)\right) - \left[1 - g(t') \exp\left(-\frac{(t-t_p)}{\tau}(1 - \alpha^2 L^2)\right) \right] H(t-t'-t_p) \right] dt', \quad (\text{A20}) \end{aligned}$$

where

$$f(t) = \exp\left(-\frac{t}{\tau}\right) \left\{ \exp\left(\frac{-x^2/4Dt}{(\pi t/D)^{1/2}}\right) - v_s \exp\left(\frac{v_s}{D}(x + v_s t)\right) \operatorname{erfc}\left[\frac{x}{2(Dt)^{1/2}} + v_s \left(\frac{t}{D}\right)^{1/2}\right] \right\}, \quad (\text{A21})$$

$$g(t) = \exp\left(\frac{t}{\tau}(1 - \alpha^2 L^2)\right). \quad (\text{A22})$$

The solution of Eq. (A20) is

$$\begin{aligned} \Delta n(x, t) = & \frac{\alpha \tau F_0}{1 - \alpha^2 L^2} \left\{ -\exp\left(-\alpha x - \frac{t'}{\tau}(1 - \alpha^2 L^2)\right) - \frac{v_s + \alpha D}{D} \left[F(t') - [G(t') - G(0)] \right] \right. \\ & \left. \times \exp\left(-\frac{t'}{\tau}(1 - \alpha^2 L^2)\right) \right\}' , \quad (\text{A23}) \end{aligned}$$

where

$$F(t) = \int dt' f(t') + \text{const}, \quad (\text{A24})$$

$$G(t) = \int dt' f(t)g(t') + \text{const}. \quad (\text{A25})$$

The first term in the integral on the right-hand side of Eq. (A24) is evaluated by using the change of the variables $t' = z^2$. The resulting integral is of the type of Eq. (A12). The second term under the integration sign is evaluated by first using the partial fraction, and then making the change of the variables, $t' = z^2$, in the two resulting integral expressions. The integral is of the type

$$\int dt \exp\left(-a^2t - \frac{b^2}{t}\right) \left(-\frac{\beta}{t^{3/2}} + \frac{\alpha}{t^{1/2}}\right) = \frac{\pi^{1/2}}{2} \sum_{\pm} \exp(\pm 2ab) \left(\frac{\alpha}{a} + \frac{\beta}{b}\right) \text{erf}\left(at^{1/2} \pm \frac{b}{t^{1/2}}\right). \quad (\text{A26})$$

Integral (A25) is evaluated by using the same procedure. In fact, the only difference between the integrals, Eqs. (A24) and (A25), is the replacement of τ^{-1} in Eq. (24) by $\alpha^2 D$ in Eq. (A25).

$$f(t, \tau)g(t, \tau) \rightarrow f(t, 1/D\alpha^2). \quad (\text{A27})$$

The mathematics is then straightforward, though rather tedious. After having collected and combined all terms, the final result is

$$\begin{aligned} \Delta n(x, t) = & \frac{\alpha F_0 \tau}{2(1-L^2\alpha^2)} \left\{ \sum_{\pm} \left(\frac{1+\alpha D/v_i}{\pm 1-L/v_i\tau} \right) \exp\left(\pm \frac{x}{L}\right) \text{erf}\left[\pm \frac{x}{(4Dt')^{1/2}} + \left(\frac{t'}{\tau}\right)^{1/2}\right] \right. \\ & + \sum_{\pm} \frac{(\pm 1 + D\alpha/v_i)}{(1-D\alpha/v_i)} \exp\left(\pm \alpha x - \frac{t'}{\tau}(1-\alpha^2 L^2)\right) \text{erfc}\left[\pm \frac{x}{(4Dt')^{1/2}} + \alpha(Dt')^{1/2}\right] \\ & \left. + \frac{2(1-L^2\alpha^2)}{(\alpha D/v_i - 1)(1-v_i^2\tau/D)} \exp\left(\frac{-t'}{\tau} + (t'v_i + x)\frac{v_i}{D}\right) \text{erfc}\left[v_i\left(\frac{t'}{D}\right)^{1/2} + \frac{x}{(4Dt')^{1/2}}\right] \right\} \Big|_{\max(0, t-t_p)} \quad (\text{A28}) \end{aligned}$$

It is easy to verify that Eq. (A28) reduces to Eq. (A13) in the limit of $v_i = 0$. In the steady state, Eq. (A28) reduces to the well-known expression

$$\lim_{t \rightarrow \infty} \Delta n(x, \infty) = \frac{\alpha F_0}{1-\alpha^2 L^2} \left[\exp(-\alpha x) - \frac{v_i + \alpha D}{v_i + L/\tau} \exp\left(-\frac{x}{L}\right) \right]. \quad (\text{A29})$$

¹C.W. White, J. Narayan, and R.T. Young, *Science* **204**, 401 (1979) and references therein.

²See, for example, R.T. Young, C.W. White, G.J. Clark, J. Narayan, W.H. Christie, M. Murakami, P.W. King, and S.D. Kramer, *Appl. Phys. Lett.* **32**, 139 (1978).

³P. Beeri, S.U. Campisano, G. Foti, and E. Rimini, *Appl. Phys. Lett.* **33**, 137 (1978); D.H. Austen, C.M. Surko, T.N.C. Venkatesan, R.E. Slusher, and J.A. Golovchenko, *Appl. Phys. Lett.* **33**, 437 (1978); J.C. Schultz and R.J. Collins, *Appl. Phys. Lett.* **34**, 84 (1979).

⁴A. Gat, J.F. Gibbons, I.J. Magee, J. Peng, V. Deline, P. Williams, and C.A. Evans, Jr., *Appl. Phys. Lett.* **32**, 276 (1978).

⁵G.K. Celler, J.M. Poate, and L.C. Kimerling, *Appl. Phys. Lett.* **32**, 464 (1978).

⁶T.N.C. Venkatesan, J.A. Golovchenko, J.M. Poate, P. Cowan, and G.K. Celler, *Appl. Phys. Lett.* **33**, 429 (1978).

⁷O.G. Kutukova and L.N. Strel'tsov, *Sov. Phys. Semicond.* **10**, 265 (1976).

⁸S.A. Prussin and W. von der Ohe, *J. Appl. Phys.* (to be published); see also TRW DSSG Semiannual Technical Report II, February 1979–June 1979, DARPA Contract No. MDA 903-78-C-0284.

⁹S.A. Prussin, W. von der Ohe, J.Z. Wilcox, and R.S. Witte, TRW Internal Report 78.4351.8-123, October 1978.

¹⁰Other mechanisms include photon-phonon interaction and free absorption. We have made estimates of the free-carrier absorption and found that for laser intensities of interest the effect is small at the ruby laser wavelength. However, it may become large at the Nd:YAG laser wavelength. The photon-phonon and free-electron absorptions were not taken into account in this work.

¹¹The pulse lengths (t_p) are on the order of 10^{-6} – 10^{-7} sec. The thermal diffusion time (time it takes the thermal energy to diffuse a distance α^{-1} away from the semiconductor surface) is $t_{th} \approx c_p/\kappa\alpha^2 \approx 10^{-8}$ – 10^{-9} sec for $\alpha = 10^4$ – 10^5 cm⁻¹, respectively. The time it takes the electron (provided that electron lifetime is long enough that the electron does not recombine earlier, $L > \alpha^{-1}$) to traverse a distance α^{-1} is $t_e = 1/D\alpha^2 \approx 10^{-8}$ sec for the typical value of $D \leq 10$ cm² sec⁻¹.

¹²S.M. See, *Physics of Semiconductor Devices* (Wiley-Interscience, New York, 1969).

¹³It is well known that, for Nd:YAG irradiation α increases rapidly with temperature. For single crystal silicon, $\alpha \approx 10$ cm⁻¹ at 300°K and increases by approximately two orders of magnitude at the melting temperature. This was not taken into account; the values used are some representative average values.

APPENDIX B

LASER ANNEALING OF LOW FLUENCE ION IMPLANTED SILICON

S. PRUSSIN
TRW Semiconductors
Lawndale, Ca 90260

AND

W. VON DER OHE
TRW Defense and Space Systems Group
One Space Park, Redondo Beach, Ca 90278

Laser annealing of low-fluence ion-implanted silicon

S. Prussin

TRW Semiconductors, Laundale, California 90260

W. von der Ohe

TRW Defense and Space Systems Group, One Space Park, Redondo Beach, California 90278

(Received 29 October 1979; accepted for publication 25 February 1980)

Ruby laser pulses of $1.5\text{--}2.5\text{ J cm}^{-2}$ were shown to be effective in dissolving defect nuclei in $\{100\}$ and $\{111\}$ silicon surfaces implanted with $10^{14}\text{--}10^{15}\text{ B cm}^{-2}$ and $(1\text{--}5)\times 10^{14}\text{ P cm}^{-2}$. No melting and only partial electrical activation appear to occur. A sequential moderate thermal anneal, 10 min at 1000°C , results in full electrical activation. A $\{111\}$ silicon surface, made amorphous by an ion implantation of $5\times 10^{14}\text{ P cm}^{-2}$ was electrically activated and completely cleared of defect nuclei without apparent melting by preceding the laser anneal by a two-step thermal anneal (30 min at 550°C , 10 min at 1000°C). The mechanism of pulse laser annealing of nonamorphous ion-implanted surfaces is discussed.

PACS numbers: 78.50.Ge, 61.70.Tm, 79.20.Ds, 61.80.Jh

1. INTRODUCTION

Ion implantation has been found to result in the introduction of electrically active impurities in an extremely uniform and reproducible manner. Concomitant with this desirable characteristic, ion implantation leaves a residue of lattice defects. These primary defects consist of impurity atoms on nonlattice positions, and the presence of many silicon vacancies and interstitials. A relatively moderate thermal anneal, 1000°C for 10 min, results in relocation of the impurity atoms to lattice positions, as shown by their electrical activation. There is, however, a considerable residuum of lattice damage remaining. These secondary defects¹ have been studied by TEM for both light and heavy implantations and have been shown to consist primarily of dislocation loops, with and without enclosed stacking faults.² For heavy implantations the Rutherford ion-backscattering and ion-channel technique has been used to show the presence of residual defects.³ A method developed by the author⁴ utilizes a two-step technique. By growing a thermal oxide, extrinsic dislocation loops are found to expand to a size of several microns. Using chemical etching techniques the intersection of these ternary defects with the surface can be observed by optical or scanning electron microscopy. This method was applied to boron and phosphorus over the range $10^{13}\text{--}10^{15}\text{ cm}^{-2}$. A thermal anneal of 1 h at 1100°C in dry N_2 was effective for 10^{14} cm^{-2} , but not for 10^{15} cm^{-2} fluences in dissolving the defect nuclei introduced by the ion implantation, so that a subsequent oxidation failed to result in the development of expanded dislocation loops.⁴ This, however, causes a significant redistribution of the implanted impurities.

In this study a Q-switched ruby laser was used. A review of the literature, as well as a recent review article, indicates that this laser has only been effectively used when the implant fluences were high enough to convert the surface to an amorphous condition.⁵ Under such conditions it was found that the laser beam melts the crystal to a depth somewhat greater than that of the implanted profile. This molten layer recrystallizes from the undamaged substrate generat-

ing an epitaxially grown defect-free single-crystalline silicon layer containing the implanted impurity atoms in normal lattice sites.⁵ Thus both defect elimination and electrical activation of the dopant atoms are simultaneously carried out. During the time the implanted region is molten, the impurity atoms diffuse rapidly in the liquid, resulting in a significant redistribution of the implanted dopant atoms. It has been suggested that the time available for annealing with Q-switched ruby lasers is too short for an unmolten damaged layer to be annealed with a single pulse and that melting followed by liquid phase epitaxy is essential for effective annealing.⁵

Continuous Ar laser annealing was applied by Gat *et al.*⁶ to silicon surfaces implanted with fluences of As heavy enough, $> 10^{14}\text{ cm}^{-2}$ at 100 keV, to convert the surface to an amorphous condition. Melting did not occur and thus, also, no redistribution of the implanted As. Fewer defects remained than were found for a single-step thermal anneal (30 min at 1000°C), but complete elimination of defect nuclei did not occur.

In this study we chose B-implant fluences of 10^{14} , 5×10^{14} , and 10^{15} cm^{-2} , and P-implant fluences of 10^{14} and $5\times 10^{14}\text{ cm}^{-2}$ into both $\{100\}$ and $\{111\}$ silicon surfaces. One implantation, that of $5\times 10^{14}\text{ P cm}^{-2}$ into a $\{111\}$ surface, resulted in amorphism. For the rest of the wafers, the surfaces retained their single crystallinity.

For these lower-fluence implants it was found that laser energies which were described in the literature as resulting in melting of the surface and completely activating the implanted impurity atoms here failed to heat the silicon surfaces sufficiently to permit more than a fraction of the implanted dopant atoms to migrate to substitutional positions. Nevertheless the temperature distribution within the implanted layer was such that complete solution of implant defect nuclei occurred. By combining a laser anneal with a short thermal anneal it was possible to achieve both defect elimination as well as complete electrical activation. Such a process would avoid impurity redistribution, permitting the dopant distribution to remain as implanted.

TABLE I. Experimental conditions.

Wafer numbers	Type	Orientation	Implant species	Implant fluence (10^{14} cm^{-2})
113A, 113B	n	(100)	11_n	1.0
114A, 114B	p	(100)	31_p	1.0
115A, 115B	n	(100)	11_n	5.0
116A, 116B	p	(100)	31_p	5.0
117A, 117B	n	(100)	11_n	10.0
213A, 213B	n	(111)	11_n	1.0
214A, 214B	p	(111)	31_p	1.0
215A, 215B	n	(111)	11_n	5.0
216A, 216B	p	(111)	31_p	5.0
217A, 217B	n	(111)	11_n	10.0

*Boron implantations at 50 keV; phosphorus implantations at 80 keV.

II. EXPERIMENTAL INVESTIGATION

Twenty wafers were subjected to implantation with boron and phosphorus ions. The orientations, conductivity types, and resistivities of the wafers, together with the fluences and implant energies are given in Table I. The implant energies were chosen to give similar distributions for the B and P ions. The wafers were commercially polished and had resistivities in the range of 1–4 $\Omega \text{ cm}$. After implantation the wafers were examined for the presence of amorphism. This was determined by the presence of a characteris-

tic "milky" appearance of the implanted area as compared to the adjacent areas protected from implantation by the wafer holder.² Wafers 216A and 216B exhibited such amorphism.

After implantation the series A wafers were subjected to an identical laser annealing process and the series B wafers were halved, each half being subjected to a separate laser annealing process. Figure 1 describes the experimental procedure.

The laser annealing was carried out with a Q-switched ruby laser operated in the multimode condition. The pulse duration was 15 nsec and the beam size was approximately 1 cm in diameter. The beam was projected through a rectangular aperture $4.4 \times 7.9 \text{ mm}$. For the A wafers, large areas, approximately one-fourth of the surface of each 2-in.-diam wafer, were pulsed with a single-laser energy. This was accomplished by using pulses of the same energy, as the wafer was repeatedly translated a distance equal to the width or height of the projected beam. Figure 2 illustrates the laser pulse distribution. The laser energies utilized were 1.0, 1.5, 2.0, and 2.5 J cm^{-2} . After laser annealing, all surfaces were examined by high-power optical microscopy. The ripple appearance characteristic of surface melting⁷ was not found. In the center of each wafer there remained a small reference area which was not subjected to laser annealing. The laser annealed areas were sufficiently large to permit a sheet resistance value to be obtained directly without introducing correction factors.

Table II lists the results of the sheet resistance measurements following the laser annealing. A minimum of six readings were taken for each annealed area and the average was taken. For the two lower energies there was considerable scatter while for the two higher energies all readings were within $\pm 5\%$ of the mean. This would appear possibly to be due to inhomogeneities within the laser beam. For the higher energies, lateral thermal conduction could smooth out the annealing effect.

After measuring the sheet resistances of the laser annealed areas all wafers were subjected to a thermal anneal of 10 min at 1000 $^{\circ}\text{C}$ in a N_2 atmosphere. The results of sheet resistance measurements repeated on the same laser annealed areas are found in Table III.

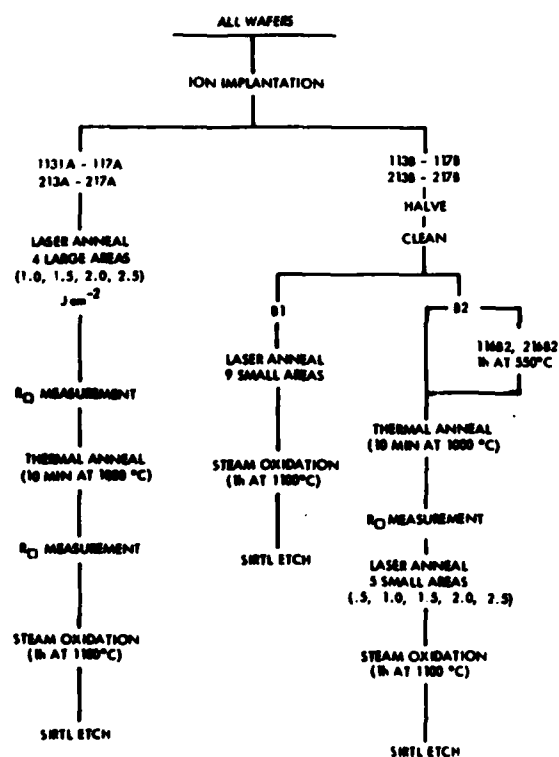


FIG. 1. Flow diagram of experiments.

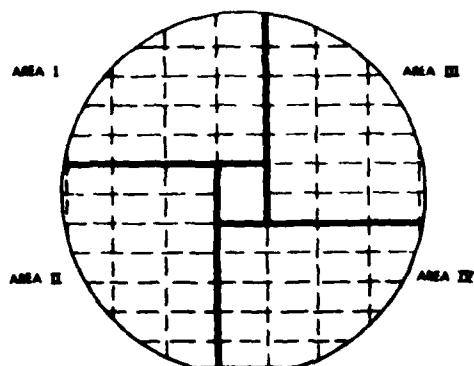


FIG. 2. Distribution of laser pulses. Area I (1.0 J cm^{-2}), area II (1.5 J cm^{-2}), area III (2.0 J cm^{-2}), area IV (2.5 J cm^{-2}).

As seen in Fig. 1, the B series wafers were halved, one-half designated as B1 and the other as B2. The B1 halves were subjected to laser annealing at nine discrete areas. Each area was $4.4 \times 7.9 \text{ mm}$, the size of the aperture through which the beam was projected. The laser energies used were 0.5 , 1.0 , 1.5 , 2.0 , and 2.5 J cm^{-2} with a single pulse as well as $0.5 (2\times)$, $0.5 (4\times)$, $1.0 (2\times)$, and $1.0 \text{ J cm}^{-2} (3\times)$. Each discrete laser annealed area was surrounded by a nonannealed area and after oxidation and Sirtl etching the laser pulse boundary (LPB) was examined by optical microscopy and compared to the ion-implant boundary (IIB), between the area of the wafer covered by the wafer holder and the area of the wafer subjected to implantation without laser annealing.

Wafers 116B and 216B received identical implantations of $5 \times 10^{14} \text{ P cm}^{-2}$, but only 216B with a $\{111\}$ orientation exhibited amorphism. The wafer halves 116B2 and 216B2 were subjected to a preanneal treatment of 1 h at 550°C to permit slow transformation of the amorphous layer to single crystallinity. This was confirmed by the disappearance of the milky surface on 216B2. All B2 halves were then annealed for 10 min at 1000°C . Sheet resistivity measurements were carried out and are given in Table III under the heading of zero-laser-beam energy.

The B2 halves were then subjected to laser annealing at five discrete areas, using single-laser pulses of 0.5 , 1.0 , 1.5 ,

2.0 , and 2.5 J cm^{-2} . Each discrete laser annealed area, $4.4 \times 7.9 \text{ mm}$, was surrounded by a nonannealed area. After steam oxidation and Sirtl etching, the surfaces were examined by optical microscopy.

III. EXPERIMENTAL RESULTS

Examination of the results listed in Table II shows that in every case there is a significant increase in electrical activity of the implanted ions in going from 1.0 to 1.5 J cm^{-2} and from 1.5 to 2.0 J cm^{-2} . In going from 2.0 to 2.5 J cm^{-2} , the change in R_{\square} appears to be much smaller. At first it might appear that this is a result of an approach to complete activation. Following the laser anneal with the moderate thermal anneal of 10 min at 1000°C results in a very significant decrease in sheet resistance for all specimens for all laser anneals, as is shown by comparing Table III with Table II. This is illustrated in Fig. 3, in which the sheet resistances for laser annealing alone and for combined laser and thermal annealing are compared.

The question arises whether this drop in sheet resistance is due to the activation of the implanted impurity or to the redistribution of the implanted atoms over a larger volume, resulting in a higher average mobility for the carriers. In the appendix the expected decrease in sheet resistivity for the B-implanted wafers, due to the redistribution occurring for an anneal of 10 min at 1000°C , is calculated to be 7.5%. This was checked by subjecting a wafer implanted with $1 \times 10^{14} \text{ B cm}^{-2}$ at 50 keV to a succession of five 2-min anneals at 1000°C . The sheet resistivities measured after each anneal were found to remain within the calculated range. We therefore conclude, for the fluences studied, that laser annealing by itself is incapable of bringing about full electrical activation of the implanted ions.

A measure of the effectiveness of laser pulses in eliminating implant damage is the comparison of the implanted and laser annealed surfaces with that of an unimplanted and unpulsed surface after oxidation and Sirtl etching. Where these are identical we can reasonably assume that the laser annealing eliminated the defect nuclei introduced by the ion implantation. For the B1 specimens, single-laser pulses of 0.5 J cm^{-2} failed to show any reduction in defect density. In every case a laser pulse of 2.0 or 2.5 J cm^{-2} resulted in com-

TABLE II. Sheet resistances of ion-implanted wafers following laser anneal.

Wafer number	Implant fluence (10^{14} cm^{-2})	Sheet resistance, Ω/\square Laser energy, J cm^{-2}			
		1.0	1.5	2.0	2.5
113A	1.0B	---	1712	877	886
114A	1.0P	---	682	480	459
115A	5.0B	1374	407	256	270
116A	5.0P	386	200	162	155
117A	10.0B	5312	280	127	128
213A	1.0B	---	975	907	794
214A	1.0P	---	766	493	450
215A	5.0B	747	306	239	246
216A	5.0P	435	185	148	145
217A	10.0B	3372	406	124	124

TABLE III. Sheet resistance in Ω/\square of laser annealed areas following thermal anneal of 10 MIN at 1000 °C in N₂ ambient

Specimen	Laser beam energy (J/cm ²)				
	0	1.0	1.5	2.0	2.5
113	619	710	714	660	658
114	409	395	400	397	390
115	193	189	191	188	190
116	139	132	131	130	130
117	113	106	102	103	99
213	655	675	690	661	650
214	393	416	409	402	395
215	199	199	194	194	192
216	150	148	144	137	136
217	109	107	109*	104	102

*Reduced area due to fracture of wafer.

plete elimination of the ion-implant defects. In most of the B1 specimens (213, 214, 114, 115, 116, and 117) all defects were eliminated by a 1.5 J cm⁻² pulse, for the others (113, 215, 216, 217) a slight defect residue remained after laser pulsing. For a laser pulse of 1.0 J cm⁻² there was a transitional structure between no annealing and complete annealing. This structure was also found at the laser pulse boundary (LPB) of the higher-energy laser annealed areas.

Figure 4 illustrates the laser pulse boundary of specimen 113B1 for 1.5 J cm⁻². The nonpulsed surface is characterized by a light concentration of oxidation stacking faults (OSF), the pulsed area is relatively clear, and the transitional region is characterized by a higher concentration of OSF corresponding to that found for the lower laser energy of 1.0 J cm⁻². Figures 5 and 6 illustrate the LPB for specimen 117B1 for 1.5 J cm⁻². In Fig. 5 we see the laser annealed area

free of OSF on the right and the transition zone containing a heavy concentration of OSF with a light background on the left. In Fig. 6 the transition zone is on the right and the unannealed area containing a heavy background together with a heavy concentration of OSF is found on the left.

In this investigation we also studied the effect of multiple laser pulses of 0.5 and 1.0 J cm⁻² with a 1-min interval.

Since a laser pulse of 1.0 J cm⁻² results in a significant reduction of the defect concentration for various implantations while 1.5 J cm⁻² was effective in eliminating all defects in most cases, it appeared reasonable that multiple pulses of 1.0 J cm⁻² might be equivalent to a single pulse of higher energy. It was found, however, that multiple pulses of 0.5 and 1.0 J cm⁻² did not reduce the defect concentration to any significant extent below the level found for a single pulse of the same energy.

Following the thermal anneal of the A series wafers, these too were subjected to steam oxidation and Sirtl etching. Microscopic examination showed results similar to those obtained with the B1 series, confirming our prior experience that an anneal of 1000 °C for 10 min has little or no effect in dissolving ion-implant defect nuclei.⁴

The annealing procedure, 10 min at 1000 °C in dry N₂, utilized for the B2 wafer halves prior to laser pulsing converts the ion-implant damage into secondary defects.¹ These consist of small dislocation loops, probably resulting from the agglomeration of the primary defects, the vacancies and the interstitial atoms generated in the implantation process. The secondary defects appear to be much more stable than the primary defects as shown by their greater resistance to solution by laser annealing. Of the ten specimens, only one, 216B2, exhibited complete defect removal with laser annealing. For all the others there was some reduction in defect concentration, but even for the highest laser pulse energy used, 2.5 J cm⁻², there was a very significant residue of defects.

The [111] oriented wafers, 216A and 216B, which received 5×10^{14} P cm⁻² implantation were the only ones of the 20 studied which exhibited amorphism after implantation. The [100] oriented wafers, 116A and 116B, which received the same implantation, did not. Specimens 116B2 and 216B2 received identical two-step thermal anneals prior to laser pulsing. The first step, 60 min at 550 °C, was chosen to per-

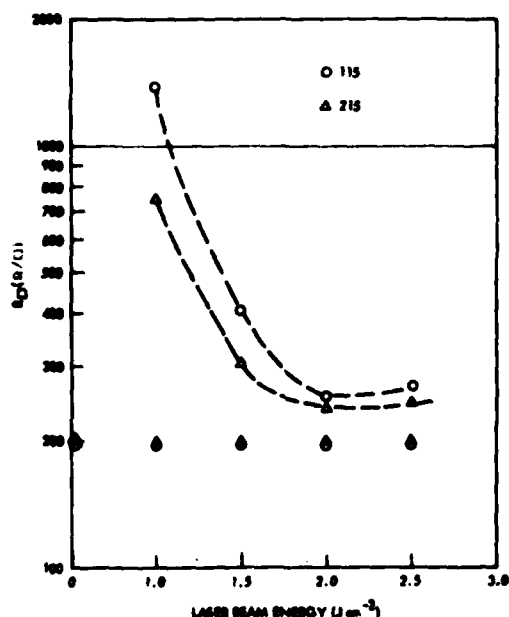


FIG. 3. Sheet resistances of 5×10^{14} B cm⁻² implanted wafers, higher connected points are laser annealed only, lower unconnected values are laser plus thermally annealed.

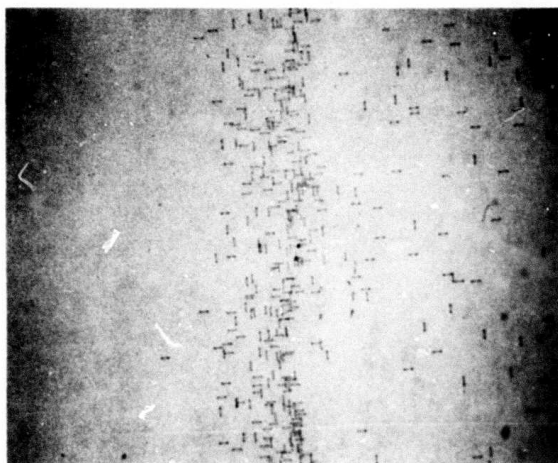


FIG. 4. Laser pulse boundary for specimen 113B1, pulsed area on the right, 1×10^{14} B cm⁻², 1.5 J cm⁻² laser energy, Sirtl etch 10 Sec, magnification 100 \times .

mit slow regrowth of the amorphous layer into single-crystal silicon. Examination of specimen 216B2 after this step did indeed show that the implanted surface had lost its milky appearance and could not be distinguished from the adjacent nonimplanted surfaces. Sheet resistivity measurements gave values of 392 Ω/\square for 116B2 and 264 Ω/\square for 216B2, agreeing with work of Miyao *et al.*⁸ that only partial activation is obtained for 550 °C anneals.

The second step, 10 min at 1000 °C, was a standard thermal anneal used to produce electrical activation of the implanted impurities. The two-step process has been shown to reduce significantly the implant damage for heavier implant fluences.⁹

We found that the use of a two-step thermal anneal for this amorphous surface permits us to dissolve the ion-implant defect nuclei with a laser pulse energy of 2.0 J cm⁻².

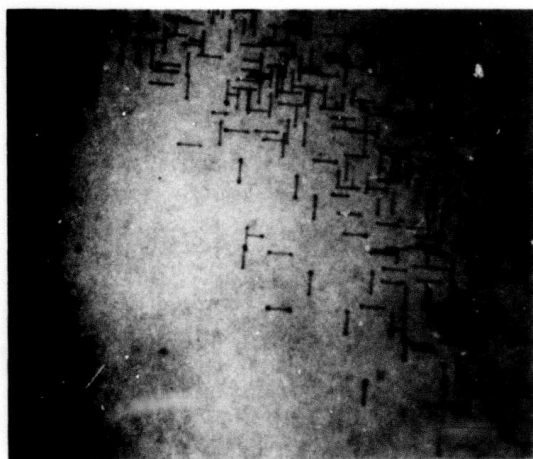


FIG. 5. Laser pulse boundary for specimen 117B1, junction of laser annealed and transition area, pulsed area on the right, 1×10^{14} B cm⁻², 1.5 J cm⁻² laser energy, Sirtl etch 10 Sec, magnification 250 \times .

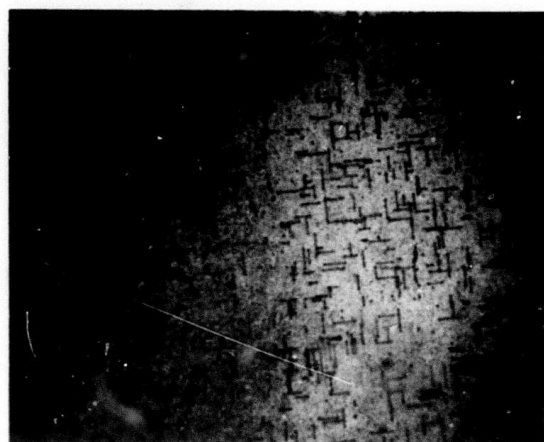


FIG. 6. Laser pulse boundary for specimen 117B1, junction of unannealed and transition area. Pulsed area on the right, 1×10^{15} cm⁻², 1.5 J cm⁻² laser energy, Sirtl etch 10 Sec, magnification 250 \times .

This last result suggests that the technique of combined laser and thermal annealing which was developed for low-fluence implants as described here might also be effectively applied to heavy implants, where the surface is converted to an amorphous condition and therefore prone to melting and concomitant impurity redistribution when subjected to pulsed laser annealing. By introducing a two-step thermal anneal, the amorphous surface is solid phase epitaxially regrown without impurity redistribution. Subsequent laser annealing results in the dissolution of the implant defects without melting and the resultant impurity redistribution.



FIG. 7. Scanning electron micrograph of neutron irradiated silicon surface exposed to a ruby laser pulse of 2.0 J cm⁻², magnification 3000 \times .

IV. DISCUSSION

The results of this study suggest that the energy release in the interaction of a pulsed ruby laser with a single-crystalline surface containing discrete implant defects occurs primarily at the defects, creating localized hot spots which result in the dissolution of the defect and in the heating and electrical activation of the area adjacent to the defect. The partial activation of the implanted impurities is explained by the defects being concentrated closer to the surface than the impurities.¹⁰ This phenomenon was clearly illustrated in a separate unpublished study of the interaction of Q-switch ruby laser pulses, identical to the ones used in this study, with silicon which has been subjected to neutral bombardment. In that study we found clear signs of the occurrence of localized melting at the silicon surfaces in the vicinity of defects, Fig. 7. We did not detect such melt spots for ion-implanted and laser annealed silicon.

The results obtained suggest that melting does not occur in the laser annealing of a single-crystalline implanted silicon surface. This belief is based on the occurrence of partial electrical activation by laser annealing, the partial solution of defects with lower laser energies, and the absence of a rippled surface characteristic of melting.

The interaction of a laser pulse with a semiconducting crystal is well understood. For each photon absorbed we generate a hole-electron pair. These have a kinetic energy as well as a potential energy equal to the band-gap energy. The kinetic energy is transferred almost immediately to the crystal lattice as heat, while the potential energy is released at such a time and place as recombination of the hole-electron pair occurs.

We recognize that the intensity of a laser pulse I in penetrating a distance x from the surface of a homogeneous crystal is given by the relation

$$I = I_0 e^{-\alpha x},$$

where I_0 is the initial intensity and α is the absorptivity.

The concentration of excess hole-electron pairs generated is proportional to the rate of absorption.

$$[n] = [p] = -k \frac{dI}{dx} = k\alpha I(x).$$

The surface volume contains not only the implanted impurities but also a high concentration of crystal defects which can act as recombination centers for the hole-electron pairs generated by the laser pulse. This permits the generation of high temperatures at defect sites by the diffusion of excess electrons and holes from adjacent areas. A requirement for this model to be applicable is that the rate of diffusion of holes and electrons to the defect recombination centers exceed by a significant amount the rate of thermal diffusion from the defect. This model has been developed in considerable detail.¹¹

Another model views the defect site as important in the generation of hole-electron pairs.

The absorptivity α is a function of the crystalline perfection of the silicon. The value for amorphous silicon exceeds that for crystalline silicon by an order of magnitude.¹² This suggests that the absorption of laser energy at a defect site is

much higher than in adjacent undamaged silicon. According to this view, we would generate high concentrations of holes and electrons around individual defect sites. We recognize that the recombination rate is proportional to the hole-electron concentration product, i.e., $R = r[n][p]$. An increase in the electron and hole concentrations of an order of magnitude results in an increase in the recombination rate of two orders of magnitude. The rate of diffusion of excess holes and electrons away from the defect site where they were generated will be proportional to their concentration gradient and hence to their concentration. This is significantly less than the rate of recombination, insuring that recombination and hence thermal release occurs at the defect sites where the hole-electron pairs were generated.

On the basis of available evidence we are unable to decide whether either or both of these suggested models are valid.

In our results we found that repeated lower-energy pulses, i.e., 0.5 and 1.0 J cm⁻² resulted in no greater solution of defect nuclei than occurs with a single pulse. It would appear that the first pulse dissolves some of the primary defect nuclei while converting others due to released thermal energy into secondary defects. As shown in our second set of experiments, secondary defects are much more resistant to dissolution by laser pulsing, so that repeated pulsing contributes little to defect removal.

V. CONCLUSIONS

(1) Pulsed laser annealing of lower-fluence ion implants does not result in full electrical activation. (2) Laser anneal single-pulse energies of 1.5 J cm⁻² are sufficient to dissolve implant defect nuclei in lower-fluence ion implants without causing melting. (3) Following a pulsed laser anneal with thermal annealing permits us to obtain both dissolution of implant defect nuclei as well as complete electrical activation without redistribution of low-fluence ion implanted impurities. (4) A two-step thermal anneal followed by a pulsed laser anneal permits us to obtain both dissolution of implant defect nuclei, as well as complete electrical activation without impurity redistribution, for implant fluences sufficiently high to cause amorphism at the surface.

This work was supported in part by the Defense Advanced Research Projects Agency.

APPENDIX: CALCULATION OF EXPECTED DROP IN SHEET RESISTANCE RESULTING FROM IMPURITY REDISTRIBUTION DUE TO THERMAL ANNEAL

The mean deviation ΔRp for the 50-keV boron implants is $5.7 \times 10^{-2} \mu\text{m}$. After a thermal anneal, the mean deviation is increased to $\Delta Rp'$ which can be expressed as

$$\Delta Rp' = [\Delta Rp^2 + 2Dt]^{1/2},$$

where D is the diffusion coefficient and t is the diffusion time.

For the thermal diffusion of implanted boron, Ricco *et al.*¹³ found that the diffusion coefficients of Kendall and Dekries¹⁴ gave a good fit. Using their value for 1000 °C, we obtain a value of $\Delta Rp'$ for a 10 min diffusion of $7.38 \times 10^{-2} \mu\text{m}$.

Nicholas¹⁵ has published an empirical expression giving the sheet resistance R_{\square} as a function of the fluence F and the mean deviation,

$$R_{\square} = 1 \times 10^{11} (F)^{-0.7} (\Delta R_p \times 10^{-4})^{-0.1}.$$

The percentage decrease in sheet resistance due to thermal anneal can therefore be calculated as 7.5%.

¹Masao Tamura, Appl. Phys. Lett. 23, 651 (1973).

²D. J. Mazey, R. S. Nelson, and R. S. Barnes, Philos. Mag. 17, 1145 (1968).

³E. Bøgh, P. Højild, and I. Stenagaard, in *Proceedings of the First International Conference on Ion Implantation*, edited by L. Chadderton and F. Eizen (Gordon and Breach, New York, 1971).

⁴S. Prussin, J. Appl. 48, 1635 (1974).

⁵C. W. White, J. Narayan, and R. T. Young, Science 204, 461 (1979).

⁶A. Gat, J. F. Gibbons, T. J. Magee, J. Peng, V. R. Deline, P. Williams, and C. A. Evans, Jr., Appl. Phys. Lett. 32, 276 (1978).

⁷H. J. Leamy, G. A. Rozgonyi, T. T. Sheng, and G. K. Celler, Appl. Phys. Lett. 32, 535 (1978).

⁸M. Miyao, N. Yoshihuro, and T. Tokuyama, J. Appl. Phys. 50, 223 (1979).

⁹L. Csépregi, W. K. Chu, H. Muller, J. W. Mayer, and T. W. Sigmon, Radiat. Eff. 28, 227 (1976).

¹⁰Yoshiaki Akasaka, Kazuo Horio, Kiyoshi Yoneda, Teruo Sakurai, Hidetoshi Nishi, Shoji Kawake, and Atsutomo Tobi, J. Appl. Phys. 44, 220 (1973).

¹¹J. Wilcox, J. Appl. Phys. (to be published).

¹²P. Baeri, S. U. Campisano, G. Foti, and E. Rimini, Appl. Phys. Lett. 33, 137 (1978).

¹³Robert P. Ricco, Joseph I. Goldstein, and J. Gordon McCallum, J. Electrochem. Soc. 124, 276 (1977).

¹⁴D. L. Kendall and D. B. DeVries, in *Semiconductor Silicon*, edited by R. R. Haberecht and E. L. Kern (The Electrochemical Society, New York, 1969), 358.

¹⁵K. H. Nicholas, Radiat. Eff. 28, 177 (1976).

APPENDIX C

CONTRIBUTION OF FREE ELECTRONS TO OPTICAL ABSORPTION IN SEMICONDUCTORS

J. Z. WILCOX

TRW Defense and Space Systems Group
One Space Park, Redondo Beach, Ca 90278

1.0 INTRODUCTION

The purpose of this report is to establish whether free carrier contribution to optical absorption in semiconductors will significantly modify absorption characteristics of intrinsic semiconductors. The work which is described in this report has been stimulated by an idea of using lasers for processing of surface regions of semiconductor materials.

Laser-induced surface processing (LISP) is based on the notion that, when irradiated by a laser whose radiation is strongly absorbed in the processed material, the surface of the irradiated material is elevated to high temperatures in controllable manners. In the usual mode of operation, LISP uses a high-power laser whose frequency is higher than the semiconductor band gap frequency, thus causing in it band-to-band transitions. High densities of free carriers may result due to photoexcitation of electrons into the conduction band. One then asks whether these high densities will contribute significantly to the optical properties of the absorbing material, specifically, to its absorption characteristics. Significant changes in the optical properties of the semiconductor would in turn affect absorption of the laser beam, i.e., the process through which the carriers have been created.

It is well known that high concentrations of free carriers in metals may cause significant absorption in visible or infrared, due to collective motion of the carriers. The absorption peaks up just below the plasma frequency. In semiconductors, high carrier concentrations may be obtained by heavy doping of the semiconductors, thermal excitation at elevated temperatures, carrier photo-generation and current injection, among other things. The relative importance of the contribution of the free carriers to optical absorption will depend on the radiation frequency. In the frequency region below the band gap energy, free carrier absorption may be the major mechanism of optical absorption. In the frequency region above the band gap energy, band-to-band transitions may be expected to be stronger than collective excitations unless the carrier concentration is very high. Thus, the strength of the absorption is expected to depend

on the number of free carriers, carrier lifetimes and frequency. It is the carrier contribution to optical absorption in the frequency region above the band gap frequency which is of interest in LISP.

The increase in the number of free carriers in strongly absorbing semiconductors during LISP is due to (1) carrier photogeneration and (2) thermal excitation of a large number of free carriers. As has already been noted, the primary mechanisms for optical absorption in strongly absorbing semiconductors are band-to-band transitions, creating (for long pulse length and long carrier lifetimes) large instantaneous concentrations of photoelectrons. The source of the thermally excited electrons is heat; thermal excitations occur after carriers photo-excited into the conduction band relax back into the valence band, transferring optical energy to thermal vibrations of the lattice.

It may be of interest to note here that thermal runaway in semiconductor laser windows is caused by thermal excitations. These windows are fabricated from intrinsic semiconductors transparent to the laser frequency. However, for high power lasers, even a very low residual absorption causes the window to heat up, thus thermally exciting carriers into the conduction band and rapidly increasing absorption with temperature.

This report will be organized as follows. The number of photo-excited and thermally-generated carriers during LISP will be calculated in Section 2.0. The diffusion equation will be used for estimating values of instantaneous densities of the photogenerated carriers. A theory of optical absorption through collective motion of free electrons is developed in Section 3.0. In Section 4.0 we calculate the absorption coefficient due to the free electrons as a function of frequency and further discuss our results.

2.0 CARRIER CONCENTRATION

2.1 Transport of Photogenerated Carriers. The instantaneous concentration of photogenerated carriers $n(x,t)$ in a semiconductor in the absence of an accelerating electric field is obtained in the low carrier concentration approximation by solving the following diffusion equation,

$$\frac{dn}{dt} = g - \frac{\Delta n}{\tau} + D \frac{\partial^2 n}{\partial x^2}, \quad (1)$$

where the generation function g gives the photogeneration rate of the carriers,

$$g = \alpha F e^{-\alpha x}, \quad (2)$$

where α is optical absorption coefficient and $F = F(t)$ gives the rate of the photon flux incident at a unit surface of the semiconductor.

$$\Delta n = n(x,t) - n_0, \quad (3)$$

where n_0 is the equilibrium carrier concentration, τ and D are minority carrier lifetimes and diffusion constant, respectively.

Assuming that g , τ and D are independent of carrier concentration, Eq. (1) can be solved by using Green function techniques. For the boundary conditions,

$$j(x = 0, t) \equiv -D \frac{\partial n}{\partial x} \bigg|_{x=0} = 0 \quad (4)$$

and

$$n(x = l) = n_0, \quad (5)$$

the Green function is

$$G(x, x', t-t') = \frac{1}{\sqrt{4\pi D(t-t')}} \sum_{n=-\infty}^{+\infty} \left(e^{-\frac{(x-x'-2n\ell)^2}{4D(t-t')}} + e^{-\frac{(x+x'-2n\ell)^2}{4D(t-t')}} \right) e^{-\frac{(t-t')}{\tau}} (-1)^n, \quad (6)$$

where ℓ is the semiconductor thickness. The boundary conditions (4) and (5) describe the physical situation when there is no flux of carriers across the semiconductor front surface, and carrier concentration at the slab back boundary is constant (n_0 is the equilibrium minority carrier concentration).

The solution of Eq. (1) is then given by

$$n(x,t) = \int_0^\ell dx' \int_0^t dt' G(x,x', t-t') g(x',t') \quad , \quad (6)$$

where the generation function $g(x,t)$ is given by Eq. (2).

For the slab thickness ℓ such that

$$\ell \gg 1/\alpha \quad , \quad (7)$$

the semiconductor can be replaced by a semi-infinite medium, with the result that the summation \sum_n in Eq. (6) is reduced to one term, namely, term $n=0$. Carrier concentration is then equal to

$$n(x,t) = \int_0^\ell dx' \int_0^t dt' G(x,x', t-t') \alpha F(t') e^{-\alpha x'} \quad , \quad (8)$$

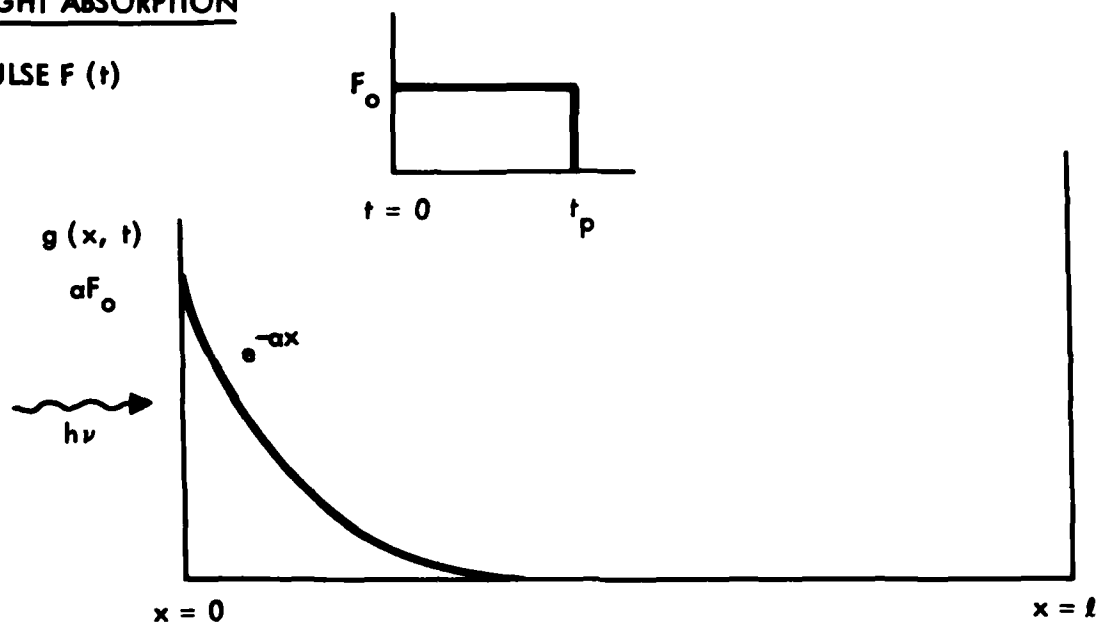
where the Green function is

$$G(x,x',t-t') = \frac{1}{\sqrt{4\pi D(t-t')}} e^{-\frac{(t-t')}{\tau}} \left(e^{-\frac{(x-x')^2}{4D(t-t')}} + e^{-\frac{(x+x')^2}{4D(t-t')}} \right) \quad (9)$$

Our reason for solving the transport equation is to find out whether the instantaneous concentration of photoexcited carriers is sufficiently large so that the strength of free carrier-induced optical absorption becomes comparable with band-to-band absorption. In order to estimate the strength of the effect, we have evaluated the concentration of carriers photoexcited at the semiconductor front surface for a square shape laser pulse (See Figure 1). Carrier concentration at $x = 0$ gives an upper estimate for concentrations inside the semiconductor ($x > 0$).

LIGHT ABSORPTION

PULSE $F(t)$



CARRIER TRANSPORT

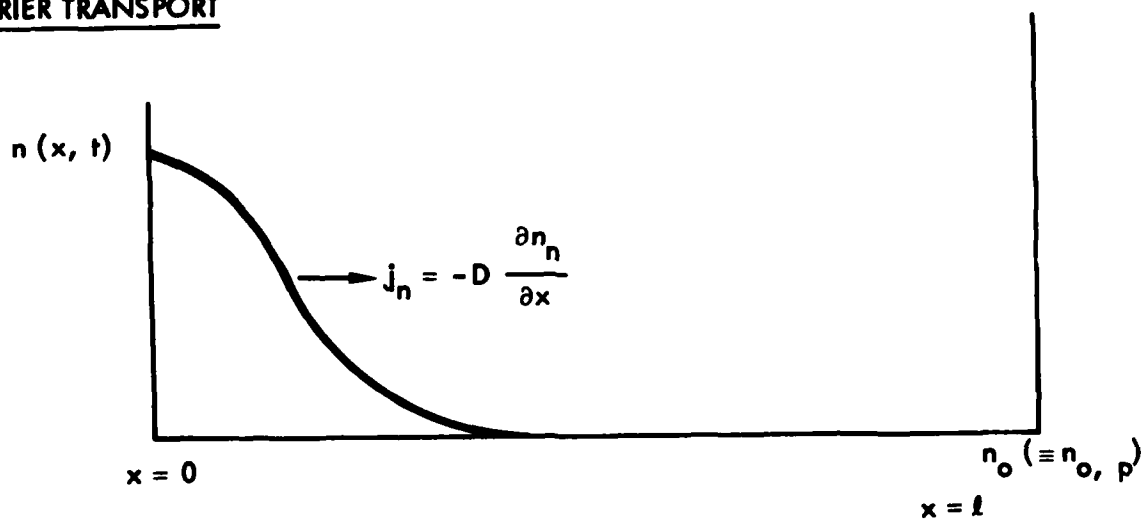


FIGURE 1. Photogeneration and transport of carriers in a semiconductor slab

For the square-shape laser pulse, the generation function $F(t)$ is equal to

$$\begin{aligned} F(t) &= F_0 & 0 < t < t_p, \\ F(t) &= 0 & t_p < t < \infty \end{aligned} \quad (10)$$

where t_p is the length of the laser pulse and F_0 is a (constant) number of arriving photons at the semiconductor front surface. Using Eqs. (9) and (10), Eq. (8) then reduces to

$$n(x=0, t) = \int_{t-t_p}^t dt' e^{-t' \left(\frac{1}{\tau} - D\alpha^2 \right)} \operatorname{erfc} (\alpha \sqrt{Dt'}), \quad (11)$$

where $\operatorname{erfc} (z)$ is the complementary error function.

Clearly, the number of photogenerated carriers is largest at the end of the laser pulse. Since, for our purposes, we are interested in the maximum values of the concentration of the photo-excited carriers, in what follows, we shall be concerned with the integral,

$$n(0, t_p) = \alpha F_0 \int_0^{t_p} dt e^{-t \left(\frac{1}{\tau} - D\alpha^2 \right)} \operatorname{erfc} (\alpha \sqrt{Dt}). \quad (12)$$

Inspecting Eq. (12), we find that there exist various physical regimes of our interest characterized by relative length of three time constants: laser pulse length (t_p), carrier lifetime (τ) and "diffusion" time ($1/D\alpha^2$). In order to obtain approximate expressions for the concentrations, in what follows, we shall therefore evaluate Eq. (12) in the following limits:

2.1.1 Steady State or a very long pulse limit: $t_p \gg \tau$, $t_p \gg 1/D\alpha^2$.

Setting the integral upper boundary to infinity, $t_p \rightarrow \infty$, Eq. (10) yields

$$n(0, t_p) \approx \frac{\alpha F_0 \tau}{1 + \alpha L}, \quad (13)$$

where the diffusion length $L = \sqrt{D\tau}$. That is, photocarrier concentration is limited by the length of the carrier lifetime or the length of the diffusion time, whichever is smaller. Here, the "diffusion time" is defined as the length of time it takes the carrier to diffuse away from the surface region (of the depth $1/\alpha$), where the carrier was originally created, into the semiconductor interior.

2.1.2 Short pulse.

2.1.2.1 Pulse shorter than diffusion time: $t_p < 1/D\alpha^2$

Expanding the error function for small arguments, Eq. (12) yields

$$n(0, t_p) \approx \alpha F_0 \frac{e^{-t_p \left(\frac{1}{\tau} - D\alpha^2 \right)} - 1}{D\alpha^2 - \frac{1}{\tau}} \quad (14)$$

In order to better understand the physical content of this result, we further reduce Eq. (14) in the following limits:

$$(a) \quad \underline{\tau < t_p (t_p < 1/\alpha^2 D)}.$$

$$n(0, t_p) \approx \alpha F_0 \tau \quad (15)$$

For the carrier lifetime shortest of the three time constant, carrier concentration is carrier lifetime-limited.

$$(b) \quad \underline{t_p < \tau (\tau < 1/\alpha^2 D \text{ or } \tau < 1/\alpha^2 D > t_p)}.$$

$$n(0, t_p) \approx \alpha F_0 t_p. \quad (16)$$

For the pulse length shorter than the carrier lifetime, the concentration is pulse length-limited.

2.1.2.2 Pulse longer than diffusion time: $t_p > 1/D\alpha^2$

In this limit, the integral in Eq. (12) is broken into two intervals, namely, $t < 1/D\alpha^2$ and $t > 1/D\alpha^2$. In the first interval, the error function is expanded for small arguments. In the second interval, the error function is expanded for large arguments. We obtain

$$n(0, t_p) = \alpha F_0 \int_0^{1/\alpha^2 D} dt e^{-t(\frac{1}{\tau} - D\alpha^2)} \left(1 - \frac{1}{\sqrt{\pi}} \alpha \sqrt{Dt}\right) + \int_{1/\alpha^2 D}^{t_p} dt \frac{e^{-t/\tau}}{\sqrt{\pi} \alpha \sqrt{Dt}} \quad (17)$$

$$= \alpha F_0 \left[\frac{e^{-\frac{1}{D\alpha^2}(\frac{1}{\tau} - D\alpha^2)} - 1}{D\alpha^2 - \frac{1}{\tau}} + \frac{1}{\alpha} \sqrt{\frac{\tau}{D}} \left(\operatorname{erf} \sqrt{\frac{t_p}{\tau}} - \operatorname{erf} \left(\frac{1}{\alpha \sqrt{D\tau}} \right) \right) \right].$$

A further insight into Eq. (17) is obtained by reducing it into simpler expressions for the following limiting cases:

(a) $t_p < \tau$ ($t_p > 1/D\alpha^2$).

Equation (17) reduce to

$$n(0, t_p) \approx F_0 \sqrt{\frac{t_p}{D}}. \quad (18)$$

The result, Eq. (8), can be better understood by rewriting it into the following form,

$$n(0, t_p) \approx \frac{F_0}{\frac{\sqrt{Dt_p}}{t_p}} \quad (18')$$

Notice that denominator of Eq. (18') has dimension of velocity. That is, for $t_p < \tau$, carrier concentration is limited by carrier diffusion within the time interval equal to the length of the laser pulse.

$$(b) \quad \underline{1/D\alpha^2 < \tau < t_p.}$$

Equation (17) reduces to

$$n(0, t_p) \approx F_0 \sqrt{\frac{\tau}{D}}, \quad (19)$$

which can be rewritten as

$$n(0, t_p) \approx \frac{F_0}{\frac{\sqrt{D\tau}}{\tau}} \quad (19')$$

That is, by analogy with Eq. (18'), for $\tau < t_p$, the concentration is limited by carrier diffusion within the time interval equal to the carrier lifetime.

$$(c) \quad \underline{\tau < 1/D\alpha^2 < t_p.}$$

Equation (17) reduces to

$$n(0, t_p) \approx \alpha F_0 \tau \quad (20)$$

That is, carrier concentration is limited by carrier lifetime. (It should be noted here that Eqs. (19) and (20) in fact reproduced the steady state result, viz., Eq. (13)).

The results, Eqs. (13) through (20), are summarized in Table 1. It is seen that the following "rule-of-thumb" applies. The surface concentration of the photoexcited carriers is limited by the length of the shortest time interval in the problem, t_p or τ , if these are the shortest time intervals; or, in the case of fast carrier diffusion, by diffusion of carriers within the time interval t_p or τ , whichever is shorter. Comments in the third column of Table 1 refer to real physical cases to which the respective limiting expressions apply. The values of the representative parameters (i.e., time constants, mobilities, diffusivities) used for identifying the various physical regimes are also listed in Table 1. In the last column of Table 1 are listed plasma frequencies corresponding to the maximum concentrations (column four). The plasma frequencies were

TABLE I. MAXIMUM INSTANTANEOUS CONCENTRATIONS OF PHOTOEXCITED ELECTRONS AT THE SURFACE OF A P-TYPE SEMICONDUCTOR IRRADIATED BY A SQUARE SHAPE RUBY LASER PULSE OF THE PEAK POWER $P_0 = 10^7$ W/cm².

PHOTOELECTRON CONCENTRATIONS						
Physical Regime		Concentrations	Comments	$n_p (cm^{-3})$	$w_p (s^{-1})$	
$t_p > \tau_n$	$t_p > 1/D_n \alpha^2$	$\tau_n > 1/D_n \alpha^2$	$F_0 \tau_n / L_n$	Quality and lightly damaged GaAs	$\approx 2 \times 10^{20}$	$\approx 3 \times 10^{14}$
		$\tau_n < 1/D_n \alpha^2$	$\alpha F_0 \tau_n$	Damaged GaAs	$\approx 3 \times 10^{18}$	$\approx 4 \times 10^{13}$
	$t_p < 1/D_n \alpha^2$	$\tau_n < 1/D_n \alpha^2$	$\alpha F_0 \tau_n$			
$t_p < \tau_n$	$t_p > 1/D_n \alpha^2$	$\tau_n > 1/D_n \alpha^2$	$F_0 \sqrt{t_p / D_n}$	Quality and damaged silicon	$\approx 3 \times 10^{21}$	$\approx 1.2 \times 10^{14}$
		$\tau_n > 1/D_n \alpha^2$	$\alpha F_0 t_p$			
	$t_p < 1/D_n \alpha^2$	$\tau_n < 1/D_n \alpha^2$	$\alpha F_0 t_p$			

SEMICONDUCTOR PARAMETERS ($T = 300^\circ\text{K}$, $\alpha = 10^4 \text{ cm}^{-1}$, $t_p = 3 \times 10^{-8} \text{ seconds}$)

Semi-conductor	Quality					Heavily Damaged				
	τ_n (s)	$\mu_n \left(\frac{\text{cm}^2}{\text{Vs}} \right)$	$D_n \left(\frac{\text{cm}^2}{\text{s}} \right)$	L_n (cm)	$\frac{1}{D_n \alpha^2} \text{ (s)}$	τ_n (s)	$\mu_n \left(\frac{\text{cm}^2}{\text{Vs}} \right)$	$D_n \left(\frac{\text{cm}^2}{\text{s}} \right)$	L_n (cm)	$\frac{1}{D_n \alpha^2} \text{ (s)}$
Si111con	10^{-3}	10^3	25	.15	4×10^{-10}	10^{-7}	10^2	2.5	5×10^{-4}	4×10^{-9}
	10^{-8}	8×10^3	200	1.4×10^{-3}	5×10^{-11}	10^{-11}	10^3	25	1.5×10^{-5}	4×10^{-10}

obtained by evaluating the expression,

$$\omega_p = \left(\frac{4\pi n e^2}{\epsilon m_e} \right)^{1/2}, \quad (21)$$

where ϵ is the dielectric constant and m_e is electron effective mass. The maximum concentrations were evaluated for the photon flux

$F_0 = 3 \times 10^{25} \text{ cm}^{-2} \text{ s}^{-1}$, where $F_0 = P_0/h\nu$. P_0 is the peak power of the ruby laser ($\lambda = .6943 \text{ } \mu\text{m}$) and was taken $P_0 = 10^7 \text{ w/cm}^2$. The pulse width was 30 nanoseconds. The pulse was square-shaped.

2.2 Surface Recombination Velocity

The effect of the presence of the surface in the vicinity of the active region is to introduce additional carrier-loss mechanism into the problem. It is customary to define an effective surface recombination velocity s of minority carriers by the expression:

$$D \left. \frac{\partial n}{\partial x} \right|_{x=0} = s \Delta n(0) = s(n(0) - n_0), \quad (22)$$

where n_0 is the equilibrium concentration of minority carriers. Thus, if one wishes to account for the effect of the surface recombination on carrier concentration, Eq. (22) will replace the boundary condition, Eq. (4), of the previous section.

The transport equation, Eq (1), with the boundary conditions, Equations (5) and (22) may be solved using again the Green function techniques. We have not constructed the complete Green function for this problem. However, we have solved Eq. (1) directly for the case of the steady state. In the steady state, solution to Eq. (1) with the boundary conditions Eq. (5) and (22) and with the source term Eq. (2) applied over a long period of time is

$$\Delta n = \frac{\alpha F \tau}{1 - \alpha^2 L^2} \left(- \frac{(s + \alpha D)}{s + L/\tau} e^{-x/L} + e^{-\alpha x} \right), \quad (23)$$

where all parameters were defined in Section 2.1.

Taking the limit of large s , $s > \alpha D$ and $s > L/\tau$, Eq. (23) reduces at $x = 0$ to the simple expression:

$$\Delta n(0) \approx \frac{F_0}{s(1 + 1/L\alpha)}$$

Thus, in the case of a rapid surface recombination, concentration of photoexcited carriers is limited by surface recombination velocity, s , as expected. Intuitively, one expects a similar result also for the transient case: For a finite pulse length, carrier concentration will be surface recombination-limited if the surface velocity is higher than any of the other characteristic velocities in the problem, i.e., if

$$s > \left(\frac{1}{\alpha \tau}, \frac{L}{\tau}, \frac{1}{\alpha t_p}, \alpha D \right) \quad (25)$$

In the other cases, i.e., for the surface recombination slower than any of the characteristic velocities, carrier concentrations will be limited by the corresponding velocities, viz., Eqs. (15) through (20).

2.3 Thermal Excitations

Heating the semiconductor to high temperatures will have a threefold effect on the semiconductor properties: (1) increase the intrinsic carrier densities, (2) increase of extrinsic carrier densities, and (3) temperature dependance of carrier lifetimes, mobilities and diffusivities.

2.3.1 Intrinsic Carrier Densities. Intrinsic carrier densities of Ge, Si and GaAs as a function of reciprocal temperature are shown in Figure 2.

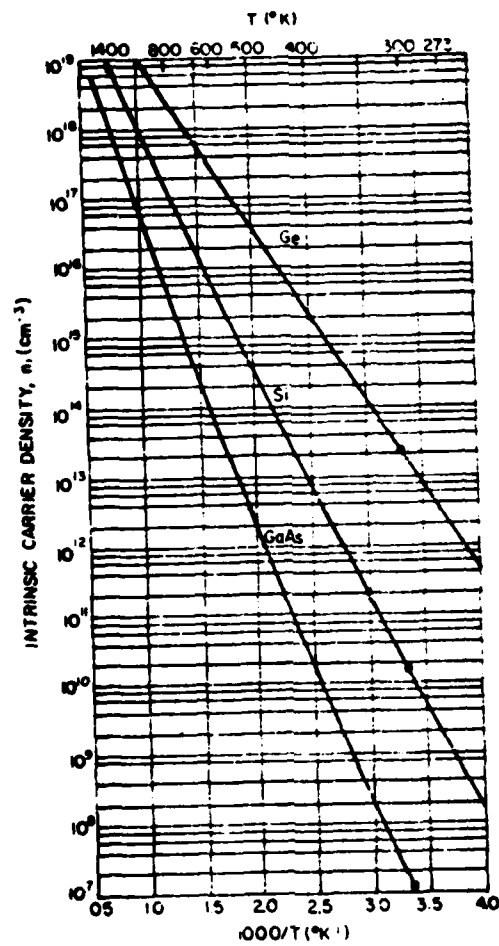


Figure 2. Intrinsic carrier densities of Ge, Si, and GaAs as a function of reciprocal temperature.

2.3.2 Extrinsic Carrier Densities. In the limit of low temperature ($kT < E_g - E_d$) or a high doping concentration, the ratio of ionized dopants at temperatures T_1 and T_2 is

$$\frac{n(T_2)}{n(T_1)} = \exp \left[-\frac{E_g - E_d}{2k} \left(\frac{1}{T_2} - \frac{1}{T_1} \right) \right], \quad (26)$$

where $E_g - E_d$ is the position of the dopant level below the bottom of the conduction band. In the limit of high temperature, or low doping, the ionized dopant concentration is approximately constant, equal to the total dopant concentration,

$$n \approx N$$

Thus, at elevated temperatures, the maximum concentration of extrinsic electrons is equal to the dopant concentration, yielding the following plasma frequencies $\omega_p = (4\pi ne^2/\epsilon m)^{1/2}$:

$$\text{GaAs} \quad \omega_p \approx 6.2 \times 10^4 \sqrt{N} \quad (27a)$$

$$\text{Si} \quad \omega_p \approx 2 \times 10^4 \sqrt{N} \quad (27b)$$

2.3.3 Temperature Dependence of Physical Constants. Temperature dependence of semiconductor parameters such as lifetimes, mobilities and diffusivities is rather complex. In the context of the present investigation, changes in temperature will modify intervals of physical regimes defined in Table I of Section 2.2. Due to their complexity, and their comparatively small effect, we shall neglect these temperature changes in the present problem.

3.0 EFFECTS OF FREE ELECTRONS ON SEMICONDUCTOR ABSORPTION

3.1 Propagation of electromagnetic wave in a lossy medium.

Attenuation of electromagnetic waves in semiconductors follows from solving Maxwell Equations in a conducting medium. Solving the Maxwell Equations for the electromagnetic wave,

$$E = E_0 \exp [i(\bar{k}x - \omega t)] \quad , \quad (28)$$

propagating in a lossy medium, one obtains for the complex (frequency-dependant) wave vector k ,

$$\bar{k}^2 = \bar{\epsilon} \frac{\omega^2}{c^2} \quad , \quad (29)$$

where ω is the angular frequency and the generalized complex dielectric constant $\bar{\epsilon}$ is

$$\bar{\epsilon} = \epsilon + i \frac{4\pi\sigma}{\omega} \quad . \quad (30)$$

Alternatively, since the generalized complex conductivity is

$$\bar{\sigma} = \sigma + \frac{i\omega}{4\pi} (1 - \epsilon) \quad . \quad (31)$$

Equation (31) can be rewritten as

$$\bar{\epsilon} = 1 + \frac{i4\pi\bar{\sigma}}{\omega} \quad . \quad (32)$$

In Eqs. (29) - (32), $\bar{\epsilon}, \bar{\sigma}$ and ϵ, σ are complex and real quantities, respectively, and are functions of angular frequency ω . Using Eq. 30, the generalized refractive index \bar{n} ,

$$\bar{n} \equiv \sqrt{\bar{\epsilon}} = n + i\kappa \quad , \quad (33)$$

can be written as

$$n^2 - \kappa^2 = \epsilon \quad (34)$$

$$\kappa n \frac{\omega}{2\pi} = \sigma \quad , \quad (35)$$

where n is the real part of the generalized refractive index \bar{n} and κ (the imaginary part of \bar{n}) is related to the extinction coefficient α (extinction of energy carried by the electromagnetic wave), by

$$\alpha = 2\kappa \frac{\omega}{c} \quad (36)$$

Hence, the absorption coefficient β (describing attenuation of the amplitude of the electromagnetic wave) is equal to

$$\beta \equiv \frac{\alpha}{2} = \kappa \frac{\omega}{c} \quad (37)$$

and the electromagnetic wave is

$$E = E_0 e^{i(kx - \omega t) - \beta x} \quad (38)$$

We note that Eqs. (34) and (35) can be rewritten alternatively as

$$n^2 = \frac{1}{2} \left(\epsilon + \sqrt{\epsilon^2 + 16\pi^2 \frac{\sigma^2}{\omega^2}} \right) \quad (39)$$

$$\kappa^2 = \frac{1}{2} \left(-\epsilon + \sqrt{\epsilon^2 + 16\pi^2 \frac{\sigma^2}{\omega^2}} \right), \quad (40)$$

giving n and κ directly in terms of ϵ and σ . Once the dielectric constant and conductivity are known, the above Equations completely describe dispersion and attenuation of electromagnetic waves propagating in a lossy medium.

3.2 Electron Susceptibility and Conductivity

In a radiation field, the current of the free carriers has a component in phase and a component out of phase with the electric field. The in-phase current contributes to the conductivity and the out-of-phase component contributes to the susceptibility. In order to estimate the free carrier contribution to σ and ϵ , it is convenient to employ a model of a damped oscillator. In this model, carrier motion is described by the following equation of motion,

$$m(\ddot{x} + \tau^{-1}\dot{x} + \omega_0^2 x) = eE_0 e^{-i\omega t} , \quad (41)$$

where the damping constant τ is electron "relaxation" time and ω_0 is the restoring force. Since, for free carriers, there is no local restriction on their motion, in what follows, the restoring force will be neglected.

Putting $\omega_0 = 0$, and using the definitions polarization $P = nex$ and current $j = ne\dot{x}$, we obtain

$$\bar{\epsilon} \equiv \epsilon_0 + 4\pi \frac{P}{E} = \left(1 + \frac{i\omega_p^2 \tau}{\omega(1-i\omega\tau)}\right) \epsilon_0 , \quad (42)$$

$$\bar{\sigma} \equiv \frac{j}{E} = \frac{ne^2 \tau}{m(1-i\omega\tau)} , \quad (43)$$

where ω_p is the plasma frequency, $\omega_p^2 = \frac{4\pi ne^2}{\epsilon m}$, and n is the free electron density. It is straightforward to verify that Eqs. (42) and (43) satisfy the relations of Section III.1. Rewriting Eqs. (42) and (43) as

$$\epsilon = \left(1 - \frac{\omega_p^2 \tau^2}{1 + \omega^2 \tau^2}\right) \epsilon_0 \quad (44)$$

and

$$\sigma = \frac{ne^2 \tau}{m(1 + \omega^2 \tau^2)} , \quad (45)$$

and substituting them into Eqs. (39) and (40), the absorption coefficient can now be evaluated.

The final remark will concern time constant τ . τ is the relaxation time, which, in the context of the damped oscillator model, is related to carrier mobility,

$$\tau = \mu \frac{m}{e} . \quad (46)$$

where m and e are electron effective mass and charge, respectively.

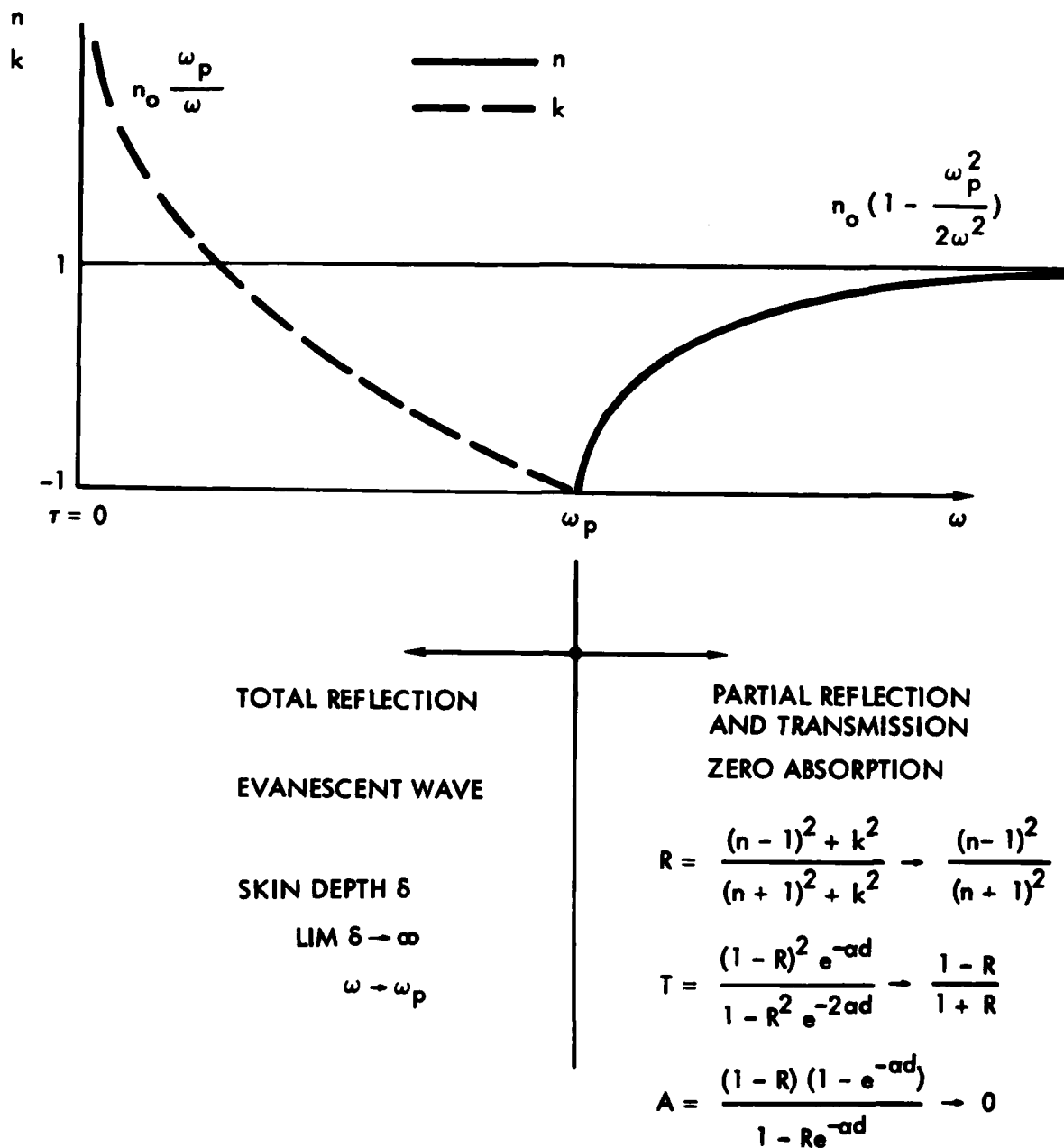
4.0 ABSORPTION COEFFICIENT

The refraction and absorption coefficients associated with free electrons are calculated by substituting Eqs. (44) and (45) into Eqs. (39) and (40). The results are sketched in Figure 3 through 5.

In Figure 3, we plot the qualitative behavior of both the real and imaginary parts of the generalized refractive index versus frequency for the case of $\tau = \infty$. This is a rather illustrative case. It shows that, in the absence of any loss mechanism, there is a total reflection at frequencies $\omega < \omega_p$. At $\omega < \omega_p$, the wave is evanescent with the skin depth $\delta (\delta \equiv \beta^{-1})$ approaching infinity as frequency ω approaches ω_p . In the frequency region above the plasma frequency, $\omega > \omega_p$, there is zero absorption ($\kappa = 0$), the wave being partially reflected and partially transmitted. There is a practically complete transmission at very high frequencies.

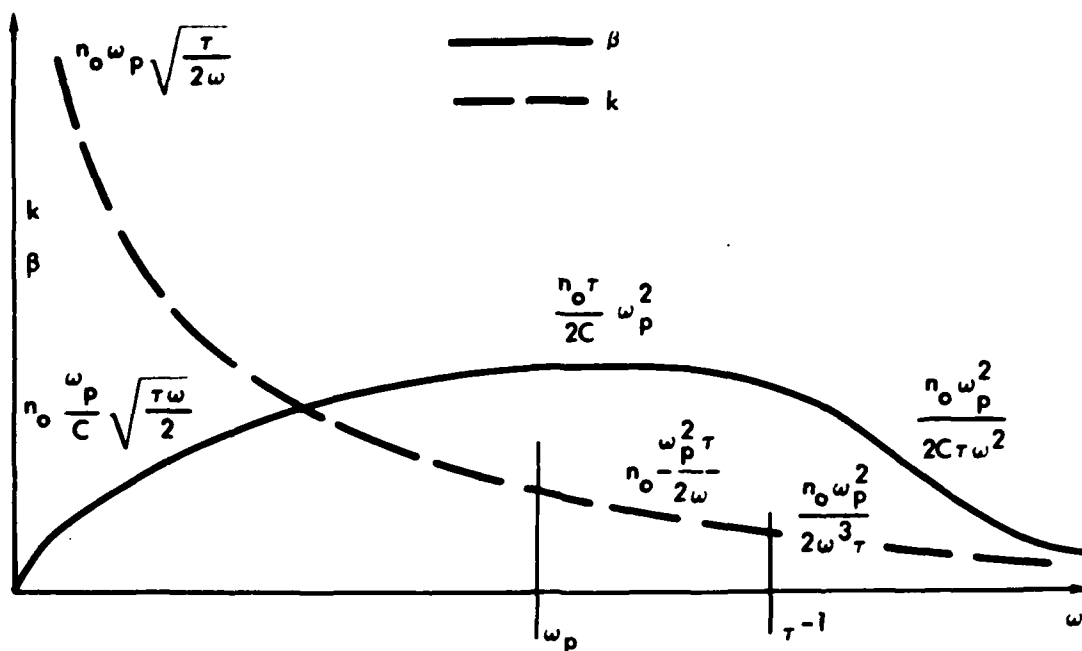
In Figure 4, we sketch the qualitative behavior of real and imaginary parts of the generalized refractive index, n and κ , respectively, versus frequency for both, the case $\omega_p > \tau^{-1}$ and $\omega_p < \tau^{-1}$. Also noted in Figure 4 are leading terms of expansions of n and κ versus ω in various frequency regimes; that is, regimes defined by relative magnitudes of parameters ω , ω_p and τ^{-1} . The leading terms were obtained by expanding expressions for n and κ in terms of smallness parameters appropriate to the various regimes. It is seen that finite values of n and κ are obtained at all frequencies indicating partial transmission, reflection and absorption of electromagnetic wave in all the frequency regions.

In Figure 5, we sketch qualitatively the imaginary part of the refractive index, κ , and the absorption coefficient β ; Figure 5.1 shows the case of $\omega_p < \tau^{-1}$ and Figure 5.2 the case $\omega_p > \tau^{-1}$. By comparing Figure 5.1 and 5.2, it is seen that the qualitative behavior of β in the two cases is the same. The absorption coefficient starts from zero at $\omega = 0$ and grows approximately with frequency as $(\omega)^{1/2}$ until ω approaches frequency

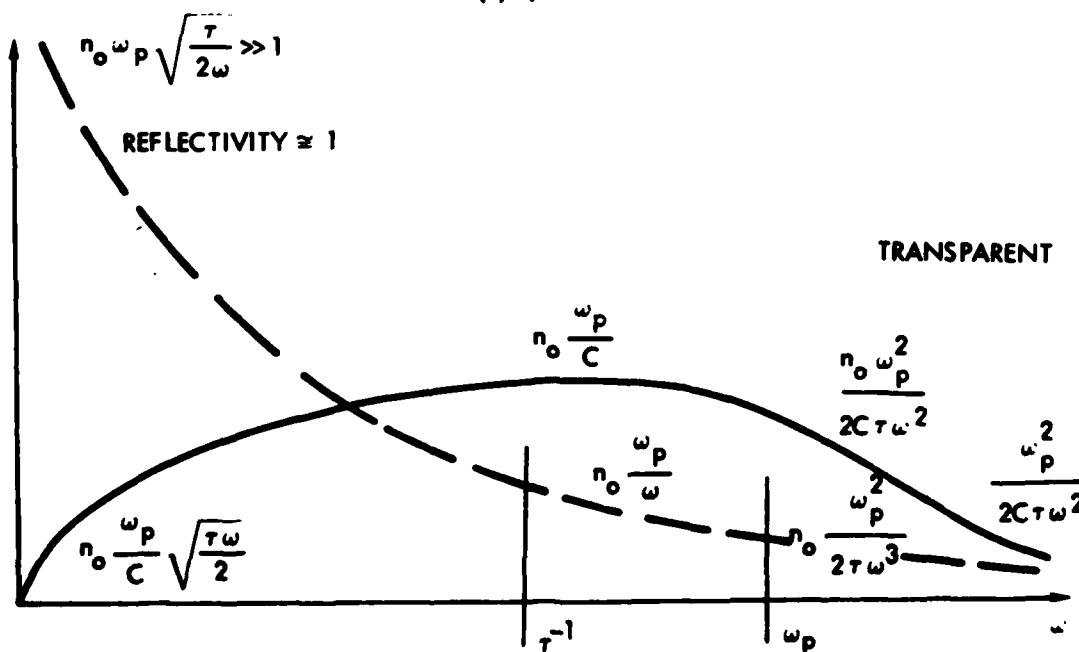


(GOOD METALS: $\tau^{-1} \ll \omega_p$, $\lambda_p \cong 1.3 \mu\text{m}$)

FIGURE 3. Real (n) and imaginary (k) parts of the generalized refractive index in the absence of any absorption mechanism. (Good metal approximation: $\tau^{-1} \ll \omega_p$, $\lambda_p \cong 1.3 \mu\text{m}$)

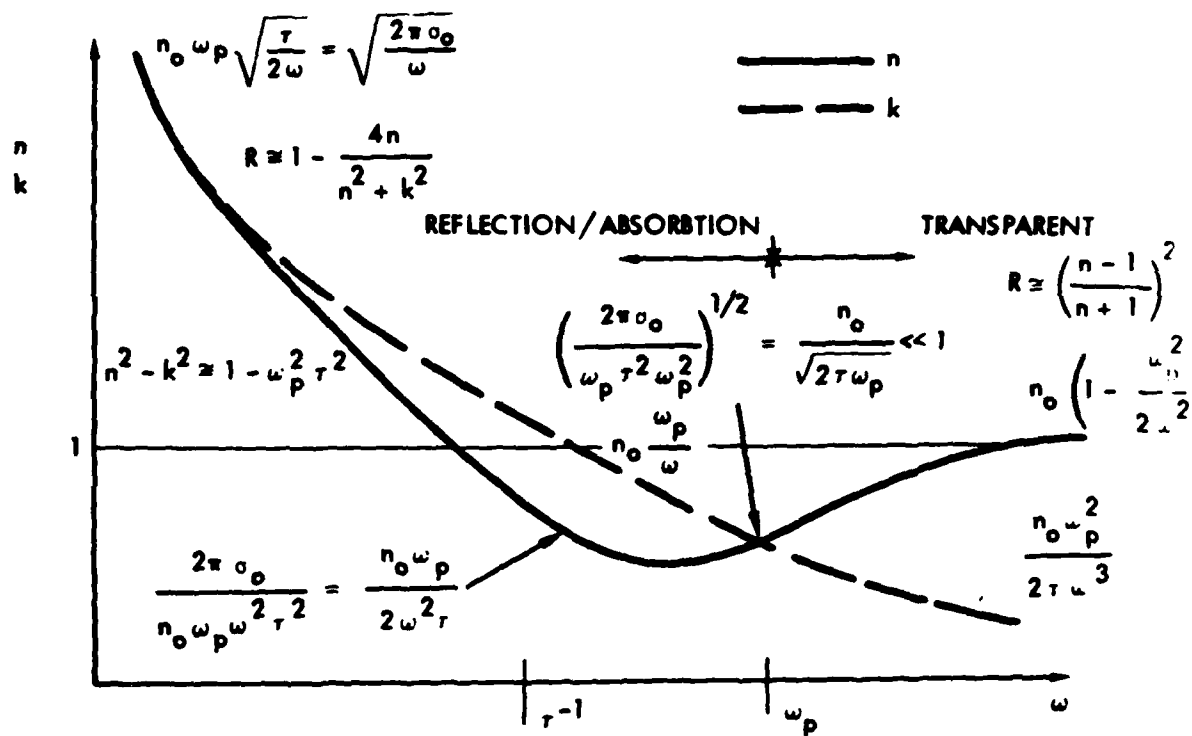


(a) (INTRINSIC SEMICONDUCTOR)

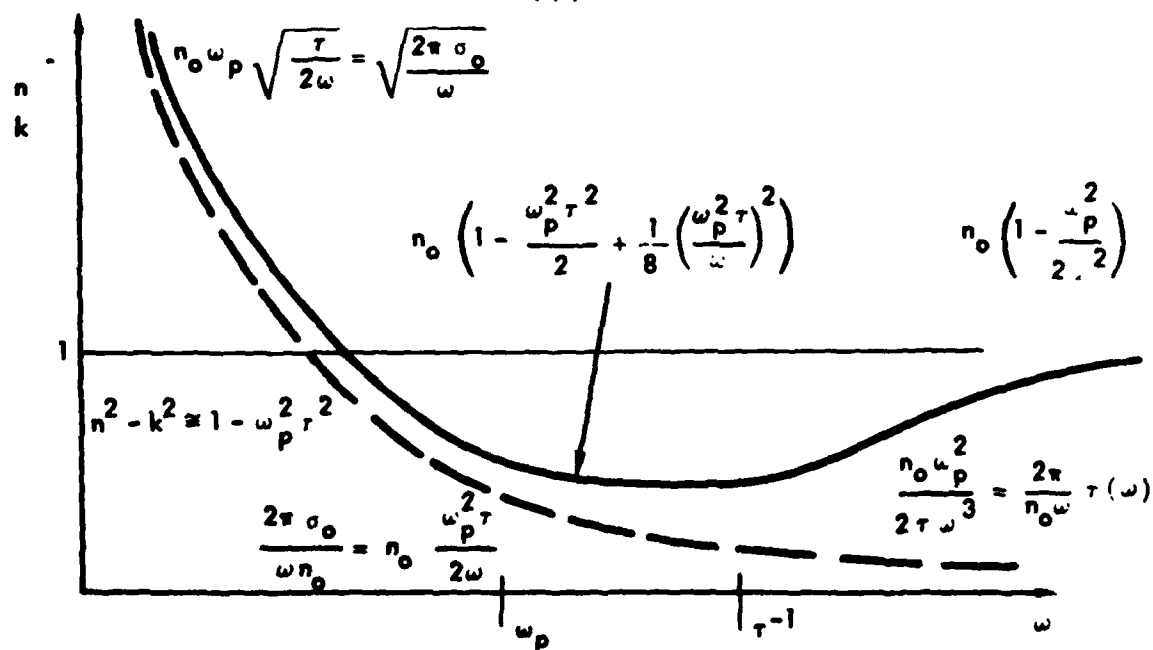


(b) (EXTRINSIC SEMICONDUCTOR)

FIGURE 5. Qualitative behavior of the imaginary part of the index of refraction (κ) and the optical absorption coefficient (β) due to the free electron effect. (a) $\tau^{-1} > \omega_p$ (intrinsic semiconductors); (b) $\omega_p > \tau^{-1}$ (extrinsic semiconductors).



(a) (EXTRINSIC SEMICONDUCTOR)



(b) (INTRINSIC SEMICONDUCTOR)

FIGURE 4. Qualitative plot of the real (n) and imaginary (k) parts of the generalized refractive index. (a) $\omega_p > \tau^{-1}$ (extrinsic semiconductor); (b) $\omega_p < \tau^{-1}$ (intrinsic semiconductor).

$\omega = \omega_p$ or τ^{-1} , whichever is smaller. Absorption then levels off (attains maximum value) until the frequency reaches τ^{-1} or ω_p , whichever is larger. Thereafter, β decays inversely proportional to the second power of the frequency, $\beta \sim \omega^{-2}$.

Thus, we can see that there exist several frequency regions in which the absorption coefficient behaves differently. It is easy to verify that, for semiconductors, unless the semiconductor is intrinsic, the limit of $\tau^{-1} < \omega_p$ usually applies. Using Eq. (46), one finds that typical values of τ range from 4×10^{-13} to 4×10^{-12} seconds (Si, InAs, GaAs and Ge); therefore, $\tau^{-1} < \omega_p$ for electron concentrations above, typically, 10^{14} cm^{-3} . Hence, for most semiconductors, the absorption coefficient $\beta = \omega_p/c$ in the frequency region of $\tau^{-1} < \omega < \omega_p$ and $\beta = \omega_p^2/2c\tau\omega^2$ for frequencies $\omega > \omega_p$. A list of calculated values of β at the ruby frequency ($\lambda = .694 \text{ } \mu\text{m}$) and at $7 \text{ } \mu\text{m}$ for silicon, InAs, GaAs and germanium for doping concentrations of 10^{17} , 10^{18} and 10^{19} cm^{-3} is given in Table 2.

In Table 2, the effect of frequency and carrier concentration on values of β is clearly seen. Absorption peaks up in the vicinity of $\omega = \omega_p$. With frequencies increasing into the near infrared region of the spectrum, the absorption decreases until, in the visible region of the spectrum, it become very small. We note that this region also coincides with the region of the onset of strong band-to-band transistions, hence, in semiconductors, the effect of free carriers on the optical properties becomes important really only at frequencies lower than the bandgap frequency. Whereas at frequencies $\omega \leq \omega_p$, the absorption coefficient $\beta = \omega_p/c = 10^4 \text{ cm}^{-1}$ for electron concentration of $n = 10^{19} \text{ cm}^{-3}$, the value of the absorption coefficient at the band gap frequency is lower than this maximum value by several orders of magnitude.

We note, finally, that in the near infrared region, where the frequency $\omega > \omega_p$, it holds that

TABLE 2. ABSORPTION COEFFICIENT ASSOCIATED WITH FREE ELECTRONS.

Semicon- ductor	$\tau(\text{sec})$	$n(\text{cm}^{-3})$	$\omega_p(\text{rad})$	$\lambda_p(\mu\text{m})$	Absorption Coefficient $\alpha(\text{cm}^{-1})$		
					$\omega = 3 \times 10^{15} \text{ rad}$ (Ruby: $\lambda = .694 \mu\text{m}$)	$\omega = 2 \times 10^{15} \text{ rad}$ (Nd: $\lambda = 1.06 \mu\text{m}$)	$\omega = 3 \times 10^{14} \text{ rad}$ ($\lambda = 6.3 \mu\text{m}$)
Si	6×10^{-13}	10^{17}	7×10^{12}	269	10^{-3}	3×10^{-3}	10^{-1}
		10^{18}	2×10^{13}	90	10^{-2}	3×10^{-2}	1
		10^{19}	7×10^{13}	27	10^{-1}	.3	10
		10^{20}	2×10^{14}	9	1	3	10^2
InAs	4×10^{-13}	10^{17}	3×10^{13}	63	3×10^{-2}	8×10^{-2}	3
		10^{18}	10^{14}	20	3×10^{-1}	8×10^{-1}	30
		10^{19}	3×10^{14}	6.3	3	8	3×10^2
		10^{20}	10^{15}	2	30	80	Metallic
GaAs	3×10^{-13}	10^{17}	2×10^{13}	94	1.6×10^{-2}	4×10^{-2}	1.6
		10^{18}	7×10^{13}	30	1.6×10^{-1}	4×10^{-1}	16
		10^{19}	2×10^{14}	9.4	1.6	4	160
		10^{20}	7×10^{14}	3	16	40	Metallic
Ge	2×10^{-12}	10^{17}	5×10^{12}	377	2×10^{-4}	6×10^{-4}	2×10^{-2}
		10^{18}	1.5×10^{13}	120	2×10^{-3}	6×10^{-3}	2×10^{-1}
		10^{19}	5×10^{13}	37.7	2×10^{-2}	6×10^{-2}	2
		10^{20}	1.5×10^{14}	12	2×10^{-1}	6×10^{-1}	20

$$16\pi^2\sigma^2/\omega^2 < \epsilon \quad , \quad (47)$$

and hence,

$$n \approx \sqrt{\epsilon} \quad . \quad (48)$$

In addition, if the carrier concentration is not too high, the dielectric constant ϵ may be approximated by its value in the absence of free electrons, $\epsilon \approx \epsilon_0 \approx n_0^2$. Therefore, electrons affect optical properties only through their contribution to conductivity, influencing κ or β , but not n :

$$\beta = \frac{\omega}{c} \kappa \approx \frac{2\pi}{n_0} \frac{\sigma}{c} \approx \frac{n_0 \omega_p^2}{2c \omega^2 \tau} \quad , \quad (49)$$

which is the expression written in Figure 4 for the limit of $\omega > (\tau^{-1}, \omega_p)$.

In the usual mode of its operation, LISP utilizes lasers whose radiation is strongly absorbed in the processed material, necessitating frequency regimes above the band gap frequencies. The ruby laser is used for irradiation of semiconductor surfaces in our laboratory. The instantaneous concentrations of free electrons induced at the semiconductor surface by the laser irradiation were calculated in Section 1.0 to be on the order or less than 10^{19} cm^{-3} . Hence, as has already been noted, in the frequency regime above the band gap frequency where the semiconductor is strongly absorbing ($\alpha \geq 10^4 \text{ cm}^{-1}$), optical absorption due to the photoexcited electrons is less than the band-to-band absorption, and hence, the effect of free electrons on the absorption coefficient can be neglected.

PART II - LASER BLOW-OFF ION IMPLANTATION

from p 2

SUMMARY OF FINAL REPORT, PART II

PART II

The objective of ~~Task 2~~ was to evaluate the laser blow-off ion implantation source. This part reports the results of this evaluation.

1.0 SUMMARY

A new, potentially less expensive and relatively simple technique for ion implantation of extended areas of semiconductor material was experimentally developed under contract to DARPA. This new method involves a source of implant ions produced by laser 'blow-off' from a piece of dopant material. Energy from a short-pulse laser is focused onto the surface of the dopant material, forming a small bubble of dopant plasma which 'blows-off'. This plasma bubble is allowed to expand into vacuum until its density and area become suitable for electrostatic acceleration to the necessary ion implant energy. Key features include the easy formation of intense ion beams of virtually any dopant material, with beam areas of several inch diameter, and without the necessity for slower and more expensive rastering of ion beams from sophisticated ion beam machines. Perhaps most significant, although also more speculative, was the potential for self-annealing of implant damage during the implant process. The possibility arose from the unique situation of the short pulse of high intensity, high energy ion beam, which rapidly deposits energy exactly in the implant region to momentarily raise the material temperature. If this possibility could have been realized in practice, an entire and sometimes troublesome separate annealing process normally associated with ion implantation might have been eliminated.

Recent theoretical studies during the present contract indicate that for the pulse durations and magnitudes likely to be obtained, only small temperature rises are expected. Thus self-annealing due to thermal effects alone is not likely. However, the very interesting and potentially important finding was made that the much higher current densities used here (pulsed) produce amorphous silicon at total doses far smaller than required with conventional implantation. The effect is quite striking, but no satisfactory explanation has been given as yet. The production of amorphism at low dose may prove very useful in annealing some low-dose structures.

During the contract, an apparatus was built and tested for implanting ions by this method. Implants of boron and antimony ions into silicon substrates were made at energies up to 65 keV. The upper energy was limited by electrical breakdown across vacuum feedthroughs and electrode spacing, a problem which appears to be solvable.

The quality of the implants was assayed with Ion Microprobe Mass Analysis (IMMA) equipment and with Spreading Resistance Probe techniques (SRP). The IMMA measurements are ideal for determining precisely the implant ion depth-profiles and surface areal uniformity, and provide meaningful comparison between the new and the conventional methods. In fact, IMMA was more appropriate as a diagnostic than actual semiconductor device fabrication tests during early phases, since the success or failure of device fabrication may say little about large and small scale uniformity and overall depth profiles which were our initial concern. Early major emphasis was therefore placed on the IMMA evaluation technique.

During the later phase, major emphasis was shifted from IMMA as diagnostic toward the quality of actual semiconductor materials and devices fabricated with the laser blow-off implantation technique. This shift was particularly important in studying possible self-annealing with the new method since IMMA could say little about semi-conductor structure and activation properties. In the final analysis the quality of the fabricated semiconductor device operation is clearly the key measure of success. Spreading resistance probe measurements were utilized to determine resistivity and implant uniformity. Implant uniformity was found to be excellent. A groove-and-stain technique was used to determine junction depths.

Careful analysis of IMMA comparisons between depth profiles for conventional and laser blow-off implants raised the possibility of a potential problem with the blow-off method. Namely, multiply-charged ions are present in the blow-off plasma, and result in implant energies at multiples of the acceleration voltage. This could produce a "tail" on the depth profile extending to considerable distances. The experiments to determine the actual junction depths showed that for many implant purposes, the problem is not serious.

2. EXPERIMENTAL APPARATUS

A schematic diagram and picture of the ion implantation system developed here is shown as Figure 1a and 1b. This system is an adaptation of the high intensity metal ion beam source described in Reference 1. The ions to be implanted are created by pulsed laser irradiation of a solid block of the implant material. In the present case a Nd:YAG laser is Q-switched with a Pockels cell, producing an 0.1 joule laser pulse with less than 0.01 microsecond length at a wavelength of 1.06 micron. The laser beam passes through steering prisms and vacuum system windows and is focused to a 1 mm diameter spot on the implant material by a 50 cm focal length lens. Tests thus far have utilized solid boron and antimony targets. This laser target is located in an electrical field-free region, with the normal to its surface directed approximately toward the silicon wafer to be implanted. The laser beam strikes the surface from an angle of about 25° to the normal. The position and angle of the boron target are adjustable to optimize the intensity and uniformity of the ion beam in the direction of the silicon wafer, since these parameters are complicated functions of the laser beam energy and angle.^{1,2}

The result of the rapid deposition of laser energy on the implant material surface is to produce a high temperature plasma "bubble" of implant material ions and electrons, which "blow-off" from the surface. In the present configuration this plasma bubble expands freely until it reaches the ion acceleration region. This distance is presently 32 cm. In the first measurements no acceleration was utilized, and the silicon wafers and an array of current measuring Faraday cups were placed at this position. This set-up allowed the measurement of implant ion fluence and areal uniformity. This configuration may prove to be valuable in its own right as a method for depositing a thin layer of certain materials for subsequent laser diffusion processing, since atoms of essentially any solid dopant can be deposited under vacuum conditions. The ion energies are a few hundred electron volts in this case, and thus barely penetrate the surface.

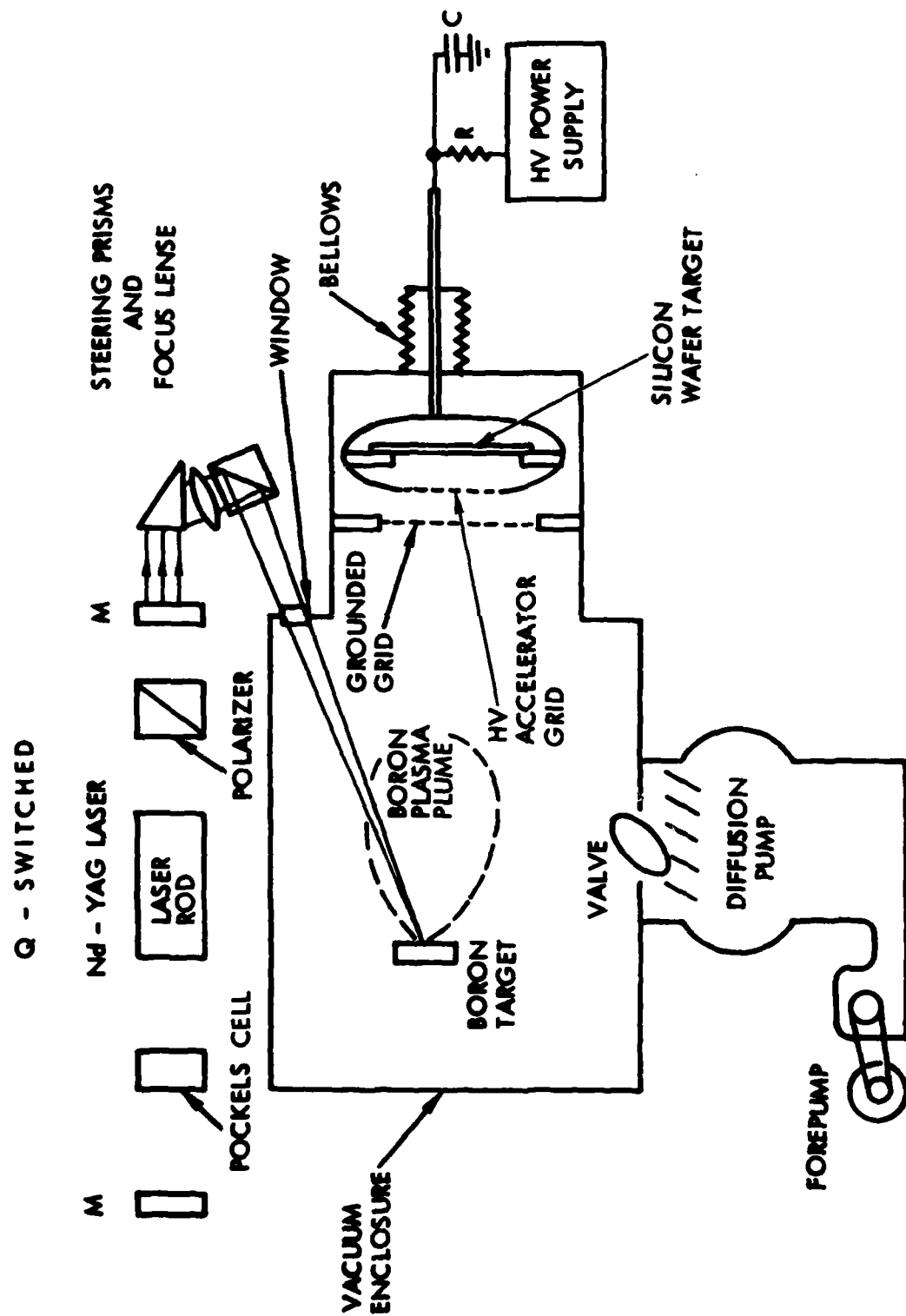


Figure 1a. Schematic Diagram of Laser Blow-Off Ion Implantation System



Figure 1b. Photograph of Laser Blow-Off Ion Implantation System

In the case where high energy implantation is to be used, acceleration of the implant ions is necessary as they reach the acceleration region. In the present configuration, this acceleration occurs between the grids shown. The first grid is held at the same potential as the field-free plasma expansion region. The second is held at a high negative voltage equal to the ion kinetic energy in eV desired. The silicon wafer is held at the same potential as the second grid at a distance approximately one centimeter beyond. This "drift" distance is intended to wash out any non-uniformity in implant caused by grid shadows or focusing effects. The drift distance cannot be too long because space charge spreading becomes severe because the plasma electrons are rejected by the ion acceleration region. The grids are presently 100 mesh stainless steel.

For initial tests, two types of silicon wafers were obtained from Monsanto. Both types are 3 inches in diameter and 0.015 inches thick, are oriented 100, and have resistivities of 10 ohm-centimeters. One type is N doped with phosphorus and the other type is P doped with boron. In order to economize on wafer material, the wafers are cut into cm-size chips for use when the measurements permit.

The accelerating voltage is supplied by a Universal Voltronics, 160 kV power supply, which charges an 0.05 microfarad capacitor across the accelerating grids. In the event of arc breakdown, the grids would have to dissipate 60 joules of energy at 50 kV. If an accelerating region area of 100 cm^2 and an implant ion density of $1 \text{ micro-coulomb/cm}^2/\text{pulse}$ is considered, the accelerating voltage drops from 50 kV to 48 kV during the pulse. A larger capacitance value would reduce the voltage change, but the present value is safer during development.

The vacuum system consists of fairly standard components including a 10 inch oil diffusion pump with liquid nitrogen cooled baffle and mechanical forepump. This system should be adequate for development purposes, but final definitive quantitative device tests may necessitate an ultra-high vacuum system to minimize surface contamination.

2.1 The Laser Blow-Off Plasma

In order to examine the characteristics of the expanding plasma plume with regard to ion energy, current and number density, and angular distribution, an array of 5 Faraday cups was placed symmetrically along an arc perpendicular to the normal to the boron laser target in a plane containing the normal. The cups were 41 cm from the target and were spaced 4.2° apart with respect to the target, that is, the 5 cups observed the target at angles of 8.4° , 4.2° and 0° each side of the normal. The distance between centers of the outer cups was 12 cm. The Faraday cups detected ions within the expanding plasma plume as the ions reached the cup collectors. These cups were designed and tested for high current operation at the plasma densities encountered. The effective detection area was 1 cm^2 . These cups were of planar construction so that the ion transit time within the cup was negligibly small compared to the transit time from the laser target to the cup. Elements within the cup were electrically biased to suppress secondary electron emission. The Faraday cups could be operated in either the current sensing mode or the total charge collection mode, with the signals displayed directly on an oscilloscope in either case. The present results with boron ions are consistent with earlier theoretical and experimental work² done in this laboratory on laser blow-off plumes. This work involved a model based on the following physical assumptions.

It was assumed that the deposited laser energy vaporizes and ionizes N_0 particles from a small region of the source material surface. This hot plasma "bubble" of N_0 ions begins to expand against the substrate and imparts momentum to it, thereby giving the center of mass of the N_0 ions a velocity v_{cm} in the laboratory coordinate frame. Because of symmetry, v_{cm} is normal to the surface. After the center of mass of the N_0 ions has moved a distance from the surface, the number density of ions remains high enough so that most of the N_0 ions equilibrate at a temperature T relative to their center of mass, which continues

to move at v_{cm} . That is, an observer moving with the center of mass would observe an essentially spherically symmetric plasma "bubble" in equilibrium at T , and freely expanding. As the number density continues to decrease, the ion velocity distribution corresponding to equilibrium at temperature T becomes "frozen" in the center-of-mass system. A laboratory observer at a larger distance from the source laser spot observes ions arriving with velocity essentially along a line from source spot to observer, but with a plume-like angular distribution due to the center-of-mass velocity v_{cm} superimposed on the purely thermal velocity distribution.

The theory thus consists simply of calculating the number density ρ and current density \vec{j} of ions to be observed in the laboratory frame resulting from N_0 ions expanding with spherical symmetry and having equilibrium velocity distribution corresponding to T in their center-of-mass system, and with a superimposed center-of-mass velocity v_{cm} .

Figure 2 shows the coordinate system for the theoretical model. The present adaptation differs in that a solid target is struck by the laser beam on the front surface. The current density of ions \vec{j} in ions per unit area per unit time is given by

$$\vec{j}(r, \theta, \lambda, \eta) = \left(\frac{512}{9}\right) \left(\frac{2}{\pi}\right)^{3/2} \left(\frac{kT}{m}\right)^{1/2} \frac{N_0}{r^3} \exp\left(\frac{-3\lambda^2}{2}\right) \cdot (\phi\eta)^{-4} \\ \times \exp\left\{\left[\frac{-32}{3}(\phi\eta)^{-2}\right]\left[1-3(\lambda \cos \theta)(\phi\eta)/4\right]\right\} \hat{r}$$

where

$$\phi = \left\{ \sqrt{(\lambda \cos \theta)^2 + \frac{16}{3}} - (\lambda \cos \theta) \right\} ,$$

$$t_{max} = 3/8 \phi \sqrt{m/3kT} \quad r ,$$

$$\eta = t/t_{max} ,$$

and

$$\lambda v_{RMS} = v_{cm} = \lambda \sqrt{3kT/m}$$

gives the relation defining the "blow-off" parameter λ . Small λ implies small v_{cm} and hence a broad angular distribution, while large λ implies a narrow "plume". The other parameters above include time t , ion mass m , Boltzmann's constant k , temperature T , and time of J_{max} , t_{max} . Figure 3 shows these results graphically in terms of J/J_{max} versus η , and therefore represents an expected picture of j versus t on an oscilloscope trace of a current sensing Faraday cup. Picture A of Figure 4 shows an actual trace of a boron ion pulse from the present measurement. The points on Figure 3 are the same data plotted there. The skewness away from the theoretical curves has been noted before² for ions, while the agreement is quite good for neutral atom blow-off.² The λ values depend on laser energy density and the target materials, and are thus subject to some control. The general agreement with theory is sufficiently good to predict currents and densities as functions of time, distance and angles. Of particular importance is the sensitivity of the angular distribution to λ , as seen next. The total number of ions passing across unit area normal to \hat{r} per pulse is given by

$$\int_0^{\infty} j \, dt = \frac{N_0}{4\pi r^2} \sqrt{\frac{2}{\pi}} \exp(-3\lambda^2/2) \times \left[\chi + \sqrt{\pi}(1/2 + \chi^2)(1 + \operatorname{erf} \chi) e^{\chi^2} \right] \hat{r}$$

where

$$\chi = \sqrt{3/2} (\lambda \cos \theta)$$

and

$$\operatorname{erf} \chi = \frac{2}{\sqrt{\pi}} \int_0^{\chi} \exp(-u^2) \, du$$

Figure 5 shows these theoretical angular distributions as functions of λ . Also included are previous experimental points obtained for aluminum ions and present points obtained for boron ions.

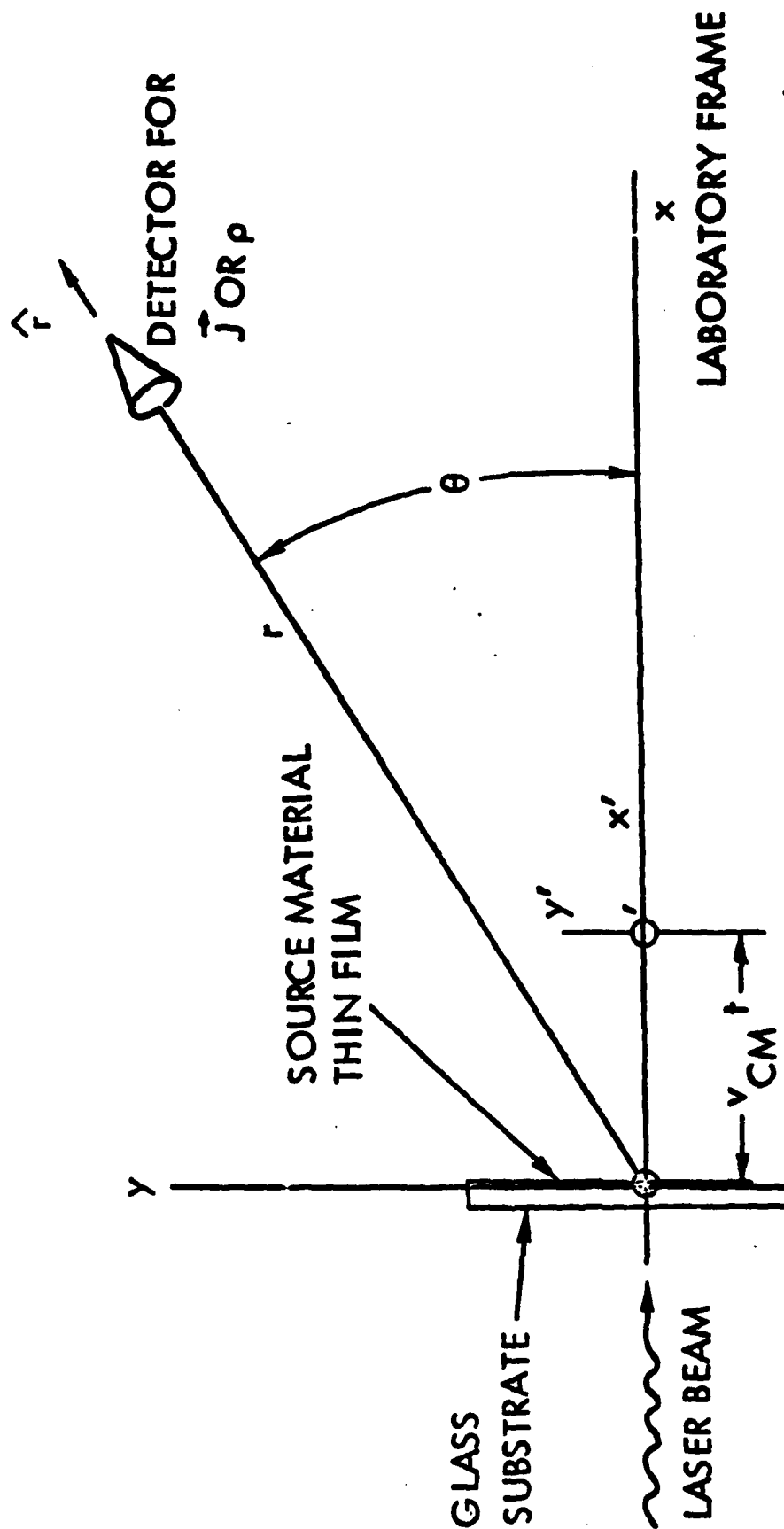


Figure 2. Geometric Arrangement for the Theoretical Model and Experiment

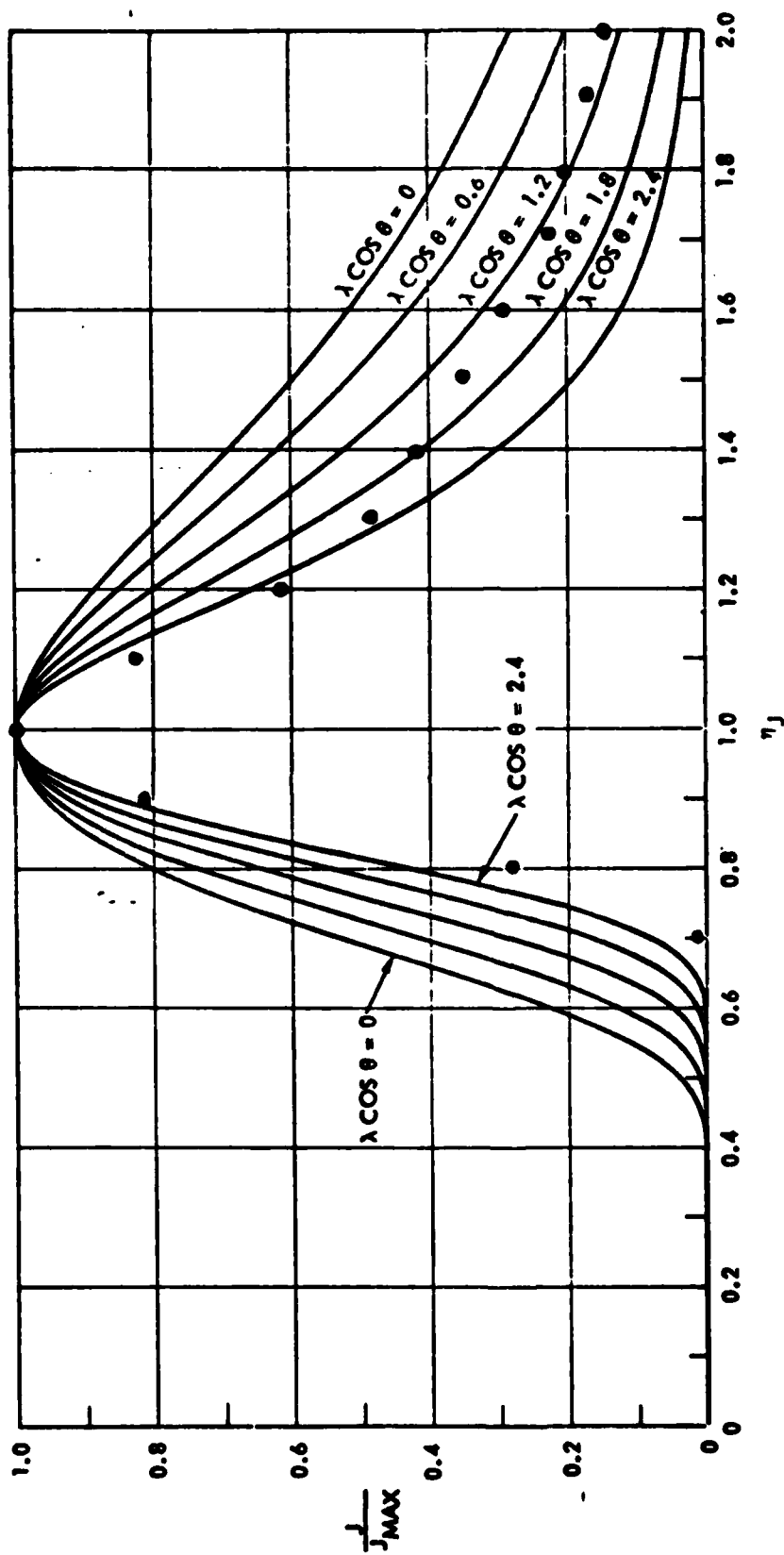
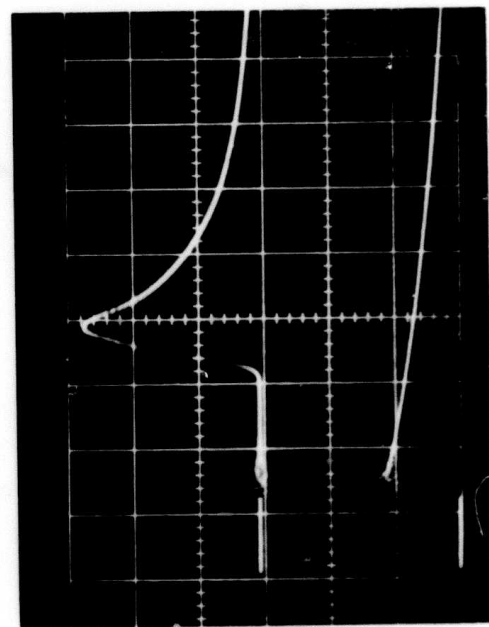
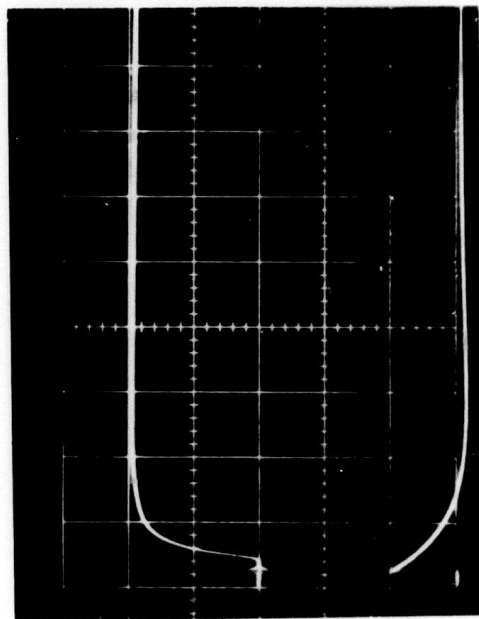


Figure 3. Theoretical Curves for Beam Particle Current Density j versus Time, Normalized to the Time at Which j is a Maximum. Points are measured values for boron ions. Boron ion current vs time.



(a)

Upper: Boron Ion Current vs Time
Lower: Laser Energy and Timing Marker
2 μsec /large div



(b)

Upper: Boron Ion Collected Charge vs Time
Lower: Laser Energy and Timing Marker
20 μsec /large div

Figure 4. Unaccelerated Boron Ion Pulses

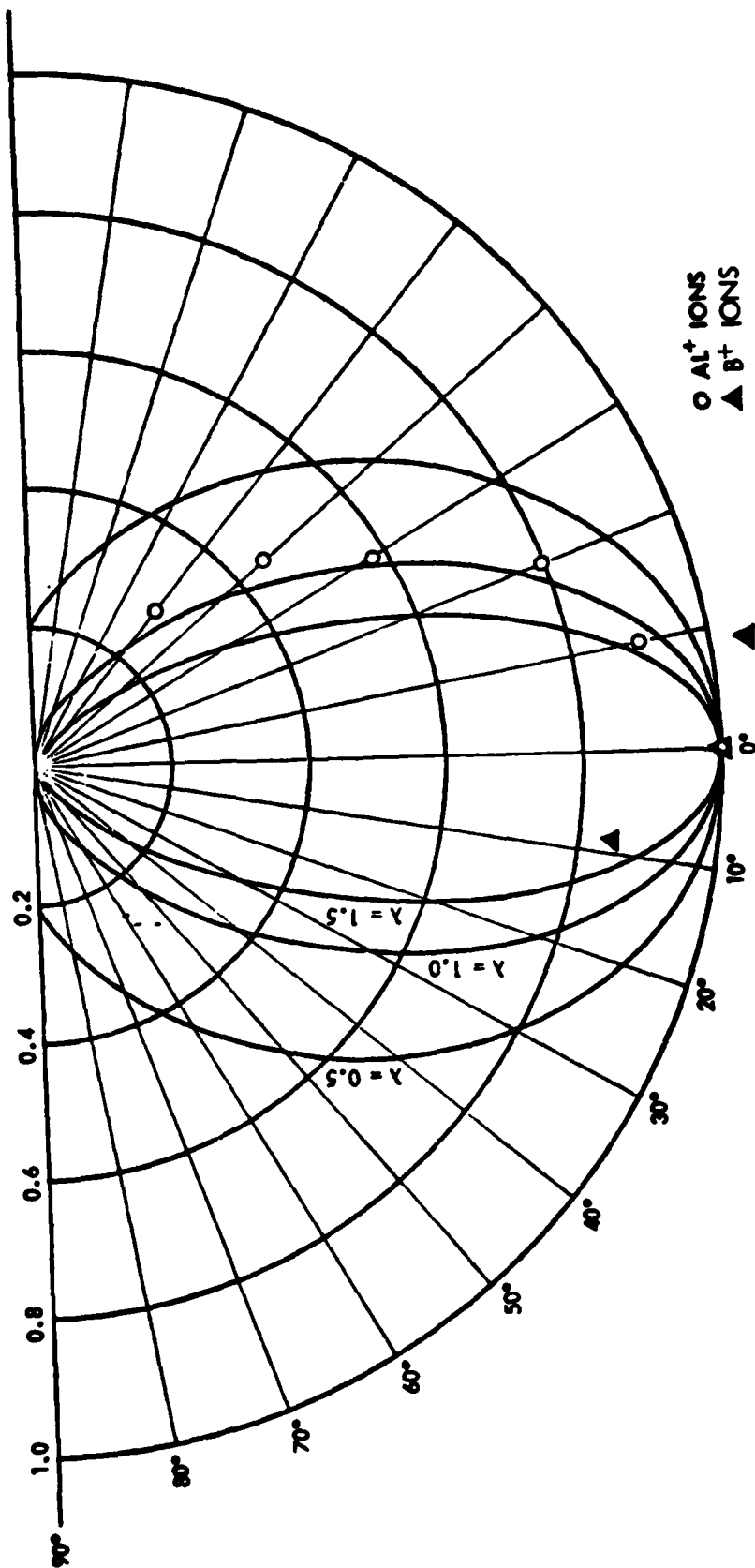


Figure 5. Theoretical Curves for $\int_0^\pi dt$ versus Detector Angle θ at Constant Distance r and Normalized to the Value for $\theta = 0$. Points are measured values for aluminum and boron ions.

It is obvious that small values of λ are necessary if one is to implant large areas with high uniformity without "rastering" the wafer between shots. The ion arrival time profiles may also be very important in self-annealing aspects, since the thermal pulse will reflect the arrival time pulse. Figures 4 and 5 from Reference 2 show examples of widely differing angular distributions depending on laser beam conditions. The presently obtained angular distributions are adequate for present purposes and will be optimized further, but it is clear that variations in ion fluence as a function of angle put eventual limits on the size of wafers which can be implanted with high uniformity over the surface.

Measurements have been made to determine the actual ion current and areal implant ion density by combining Faraday cup array current measurements with implant ion deposition without acceleration. The currents and charge collected are displayed directly on an oscilloscope for the two outer and the middle Faraday cups in the array. The apertures of the other two cups are covered with silicon wafer chips. A number of laser shots are then made to deposit boron on the silicon chips, at the same time summing the charge collected on either side of the chips. Table 1 shows the results of one such run. In this particular case, cup A was on the side of the normal toward the laser beam, and the results show the asymmetry toward the laser beam which was reported earlier.² The uniformity of $\pm 2\%$ over the 3 cm interval between cups A and M is acceptable for now, but the $\pm 8\%$ variation between cups B and M is not. This run shows a particular strong dependence on angle, a dependence itself dependent on laser conditions as noted above.

Table 1. Boron on Silicon Experimental Results

SHOT NUMBER	RELATIVE LASER ENERGY	CHARGE COLLECTED (MICROCLOULOMBS)		
		CUP A	CUP M	CUP B
1	13.1	OFF SCREEN (~1.05)	.98	.80
2	9.9	.98	.92	.79
3	8.5	.79	.77	.67
4	8.6	.75	.73	.63
5	8.4	.78	.75	.65
		<u>4.35</u>	<u>4.15</u>	<u>3.54</u>

3. CHARACTERIZATION OF SILICON SURFACES ION IMPLANTED BY THE LASER BLOW-OFF TECHNIQUE

Conventional commercial ion implantation equipment utilizes a collimated beam which is rastered vertically and horizontally across the silicon wafer surface. This results in a very uniform distribution of the implanted atoms, one of the desirable features of ion implantation. In addition, the use of an analyzing magnet insures that the only species implanted is a single-charged ion of one of the isotopes.

The laser blow-off technique utilizes a series of plasma blow-offs of implant material from the source surface which are then accelerated to the desired energy before implantation. Here one expects to implant all isotopes of the source and to implant both doubly as well as singly charged ions. The doubly charged ions will be accelerated to a higher velocity, equivalent to twice the energy for singly charged ions.

Silicon wafers were implanted here by a conventional commercial ion implanter as standards of comparison for evaluation and characterization of the blow-off implanted surfaces. The implantation of such standard wafers is uniform and reproducible and the impurity distribution has been extensively studied and described.

To demonstrate the characterization techniques, five wafers were prepared. Three of these were implanted with a conventional implanter. They were 2-inch n-type, (100) silicon wafers with a resistivity of 2 Ωcm and were implanted with 10^{13} , 10^{14} , and 10^{15}B^{11} at 75 keV. The two blow-off prepared wafers were 3 inches in diameter. One was 10 Ωcm n-type and was implanted with boron; the other was 10 Ωcm p-type and was implanted with antimony.

3.1 The as-implanted Surfaces

There is a limited amount of information that can be obtained from the as-implanted surface. The implanted ions are on non-lattice positions. Thus they do not have electric properties which can be measured. Normally the as-implanted surface, due to the effect of the defects on carrier mobility, exhibits a very high resistivity. It requires a heat treatment to permit the implanted ions to diffuse to lattice positions.

The defect structure is also difficult to evaluate in the as-implanted surface. The use of transmission electron microscopy (TEM) also requires the application of a thermal anneal. This causes the agglomeration of the point defects, i.e., vacancies and interstitial atoms, so that a resultant defect is obtained that is large enough to be detected by TEM.

An important factor characterizing an ion implanted surface is whether that surface becomes amorphous as a result of the implantation. This is usually indicated by the development of a "milky" appearance. Such amorphism is found in conventionally implanted surfaces subjected to high fluences of heavy ions. In the laser blow-off implants, amorphism was noted at surprisingly low fluences at implant energies of 20 keV, boron into silicon. Amorphism was noted at fluences as low as 5×10^{14} B/cm². At implant energies above 50 keV, only antimony produced amorphism at this fluence. This surprising result is attributed to the very high instantaneous current densities occurring during laser blow-off implantation.

3.2 Uniformity of Implantation

The presence of group III and group V implanted ions in silicon can be easily detected by utilizing their electrical properties. As mentioned earlier, it is necessary to anneal the implanted surfaces to cause the implanted ions to diffuse to lattice positions where they exhibit electrical properties. A two step thermal anneal was used to activate the implanted ions. The first step was a 1 hour anneal in dry N₂ at 550°C. This treatment was specifically developed for implantations where the surface becomes amorphous. In such cases it permits the slow solid state epitaxial regrowth of the amorphous surface layer. The second step, a 10 minute anneal at 1000°C, is chosen to give complete electrical activation with a minimum of impurity redistribution by diffusion.

With the ions activated one can measure the uniformity of implantation by taking a traverse across the surface with a spreading resistance probe (SRP). Figure 6a illustrates a SRP traverse taken across a diameter from a starting position near the edge. We note that near the edge the resistivity is higher, corresponding to a significantly lower boron concentration. Within the inner 2.5 inch circle the implant distribution is fairly constant.

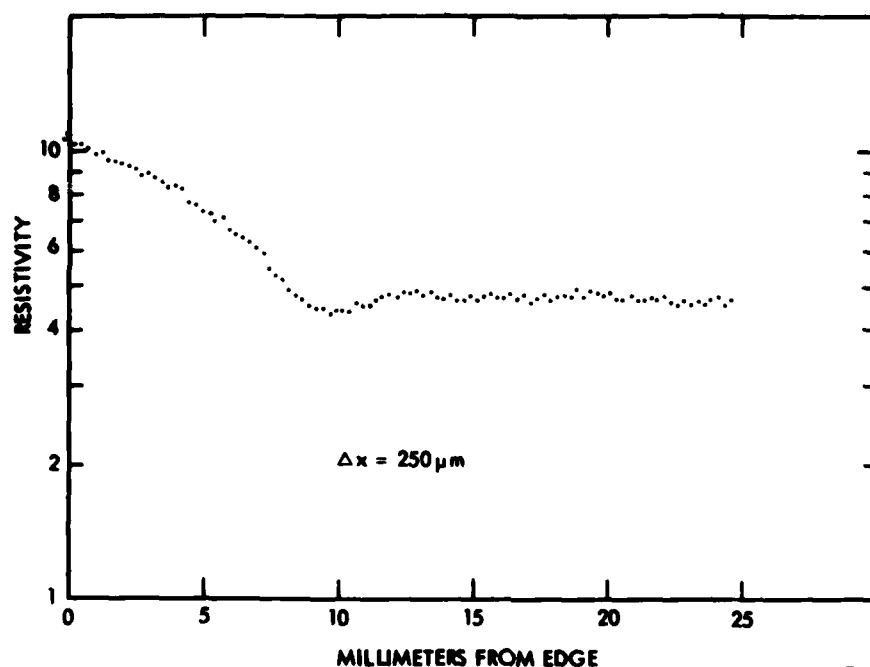


Figure 6a. Spreading Resistance Profile of Experiment a1 Laser Blow-off Implantation, along Diameter, 250 Micron Step, 25 mm Traverse

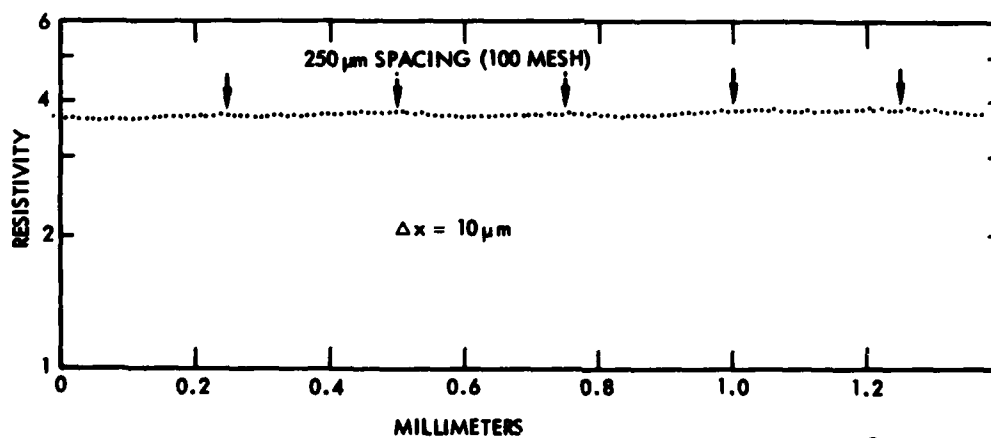


Figure 6b. Spreading Resistance Profile of Experimental Laser Blow-off Implantation, in Center, 10 Micron Step, 1.4 mm Traverse

Figure 6b illustrates an SRP traverse taken in the center of the wafer with a step, Δx , of only 10 μm . The aim here is to determine whether the accelerator grid affects the implantation pattern. It may be noted that there is a very slight undulation in the SRP traverse with a period of 250 μm . This corresponds to the grid mesh of 100 per inch.

3.3 Implant Fluence

The implant fluence is determined from the product of the number of pulses, the duration of each pulse, and the current density measured by a Faraday cup. For the first experimental B implantation, assuming singly charged ions, this was calculated to be $5.4 \times 10^{14} \text{ B cm}^{-2}$.

K. H. Nicholas (3) has developed a useful algorithm which permits one to predict the sheet resistances of boron-implanted layers prepared by conventional ion implanters. One can use this algorithm to estimate the fluence obtained with the experimental implanter. The algorithm derives the sheet resistance R in Ω/\square from the expression

$$R = 1 \times 10^{11} D^{-.7} (10^{-4} \Delta R_p)^{-.3}$$

where D is the fluence, Bcm^{-2} , and ΔR_p is the projected standard deviation, μm . Choosing the value for ΔR_p of .057 μm from the tables of Bernard Smith, Harwell, for a 50 keV implantation and using the value of 330.7 Ω/\square obtained by 4-pt probe measurement, one can calculate a fluence of $2.3 \times 10^{14} \text{ Bcm}^{-2}$. By comparison a similar calculation for the conventionally implanted B fluences of 1×10^{13} , 1×10^{14} and $1 \times 10^{15} \text{ Bcm}^{-2}$ with R_\square 's of 1995, 493, and 92.25 Ω/\square give values of 1.64×10^{13} , 1.21×10^{14} and $1.32 \times 10^{15} \text{ Bcm}^{-2}$.

The fluence calculated for the experimental implantation is less than half of that obtained on the basis of the Faraday cup. One possibility is that a significant fraction of the ions were multiply charged resulting in an actual fluence lower than that calculated on the basis of singly charged ions. This becomes evident on the basis of implant penetration measurements to be described next.

3.4 Implant Penetration

The penetration of the implanted ions is determined by three factors, the atomic or molecular weight, the charge number on the ion, and the accelerating voltage. Because of their closeness in atomic weight, isotopes will exhibit only slight differences in penetration. Multiple atomic ions, if such occur will penetrate a significantly lesser distance into the silicon while multiply charged ions will penetrate a significantly greater distance. An accurate model (LSS) exists and the distributions for these conditions can be predicted.

The ion microprobe represents a means of obtaining an impurity distribution profile. Comparing such a profile for an experimental laser blowoff implantation with one obtained for a conventional implantation of the same fluence and energy enables the evaluation of the contributions of multiple atomic species and multiply charged ions.

Implanted impurities are often used to generate pn junctions in device preparation, and the depth of this junction below the silicon surface is an important factor in device behavior. Of the factors mentioned above, one, the presence of multiply charged ions, plays a significant role in affecting junction penetration, x_j , and its presence can be easily detected from measurements of junction penetration. Such measurements were used to characterize the experimental implantations. This x_j value was compared with the values obtained from conventional implantations performed with the same energy and fluence.

While techniques for measuring x_j have been available for several decades, they have never been satisfactorily applied to the very shallow junctions obtained with ion implantation. A recent paper by C. P. Wu and his associates at RCA Laboratories, Princeton, "Techniques for Lapping and Staining Ion-Implanted Layers," J. Electrochem. Soc. 126, 1982 (1979) describes a series of precautions that are required to adapt present angle-lap techniques to the measurement of such shallow junctions. We have developed a new technique which we feel gives the requisite accuracy without the investment of excessive time and care that prior techniques appear to require. This technique, which we intend to publish in the scientific literature is described under the section on Groove and Stain Technique.

3.5 Implant Damage

Together with the desired introduction of impurity atoms into the silicon lattice there also occurs undesired lattice damage. The thermal anneal which was used here permits the implanted atoms to migrate to lattice positions and thus become electrically active. It has been shown (4, 5) that a considerably more drastic anneal, i.e. higher temperature at a longer time is required to remove the concomitant lattice damage.

A single technique that has been developed for studying implant defects consists of exposing the ion implanted surface to a thermal oxidation such as 1 hour in wet oxygen at 1100°C. This causes the implant defects to expand to stacking faults (SF) which are several orders of magnitude larger and can thus be detected by optical microscopy. This is accomplished by stripping off the grown SiO_2 with an HF rinse and subjecting the bare silicon surface to a short Sirtl etch. Figure 7 illustrates the stacking fault density found for a $1 \times 10^{14} \text{ B cm}^{-2}$ fluence implanted by a conventional ion implanter.

It is our intent to evaluate the implant damage developed by our experimental technique in two ways. The first is to compare the SF concentrations obtained for the experimental technique with that obtained for a conventional implantation of the same fluence and energy. The second is to determine the thermal annealing conditions necessary to dissolve the defects generated by the experimental implantation and to compare it to the annealing conditions required for a similar conventional implantation.

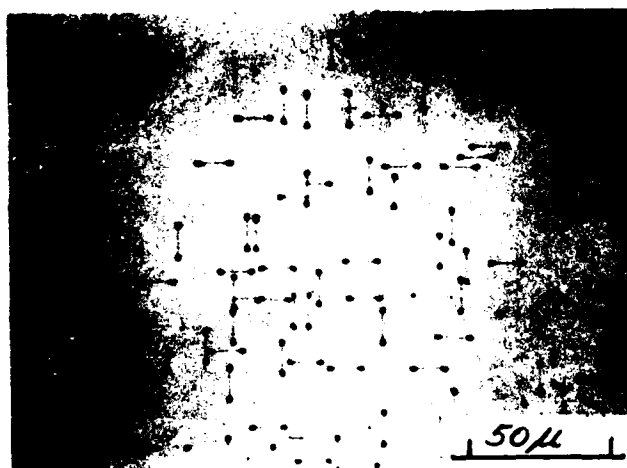


Figure 7. Ion Implant Boundary, 10^{14} B cm $^{-2}$, 50 keV (100) wet
Oxidized at 1100°C for 1h, Sirtl etched 30 sec.
Magnification 405X

3.6 Groove and Stain Technique

The measurement of shallow junctions characteristic of ion implantation raises special problems. We have developed a technique to permit accurate reproducible measurement of such junctions, using a groove and stain technique together with a profilometer. There are two variants to this procedure, one a fairly time-consuming one, and the other a short convenient one. In this study the latter was used.

Our specimens in this study were three n-type wafers of 1-4 Ωcm resistivity conventionally implanted with 1×10^{13} , 1×10^{14} and $1 \times 10^{15} \text{ B}^{11} \text{ cm}^{-2}$ at 75 keV, and a 10 Ωcm n-type wafer experimentally implanted with the laser blow-off technique with approximately $2 \times 10^{14} \text{ B}$ (natural isotopic abundance) at 50 keV. All wafers were subjected to a two step anneal, 1h at 550°C, and 10 minutes at 1000°C.

The process began by grooving the wafer surfaces. For this procedure, lower than conventional pressures were used so that the groove depth exceeded the junction depth only in part of the groove length. In other grooved areas the groove was shallower than the junction. After staining, the lighter n-type region appeared only where the groove extended below the pn junction. Figure 8 illustrates a stained groove length, part of which was deeper than the junction and part of which was shallower. As Section A-A, the groove depth was exactly equal to the junction depth. Measuring the groove depth at this point permits one to obtain the junction depth. Figure 9 exhibits the profiles measured at these points giving values for the junction depths.

The following results were obtained:

<u>FLUENCE</u>	<u>ENERGY</u>	<u>IMPLANT TYPE</u>	<u>X_j, Å</u>
$1 \times 10^{13} \text{ B}^{11}$	75 keV	Convent.	4800
$1 \times 10^{14} \text{ B}^{11}$	75 keV	Convent.	5200
$1 \times 10^{15} \text{ B}^{11}$	75 keV	Convent.	5500
$\sim 2 \times 10^{14} \text{ B}$	50 keV	Laser Blowoff	6000

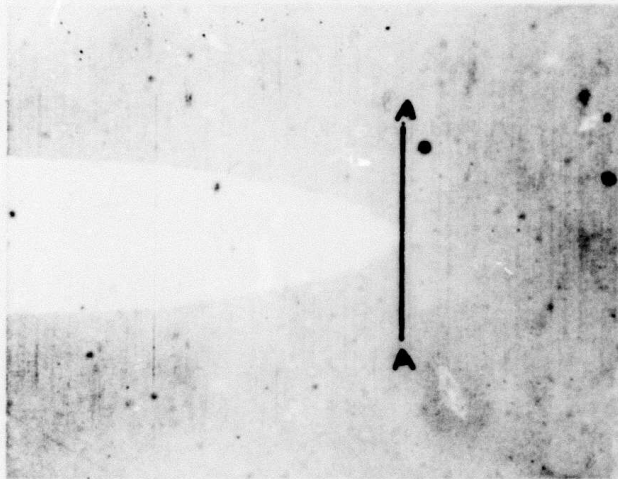


FIGURE 8. Microphotograph of grooved and stained wafer. Mag. 100X
Profile measured at A-A

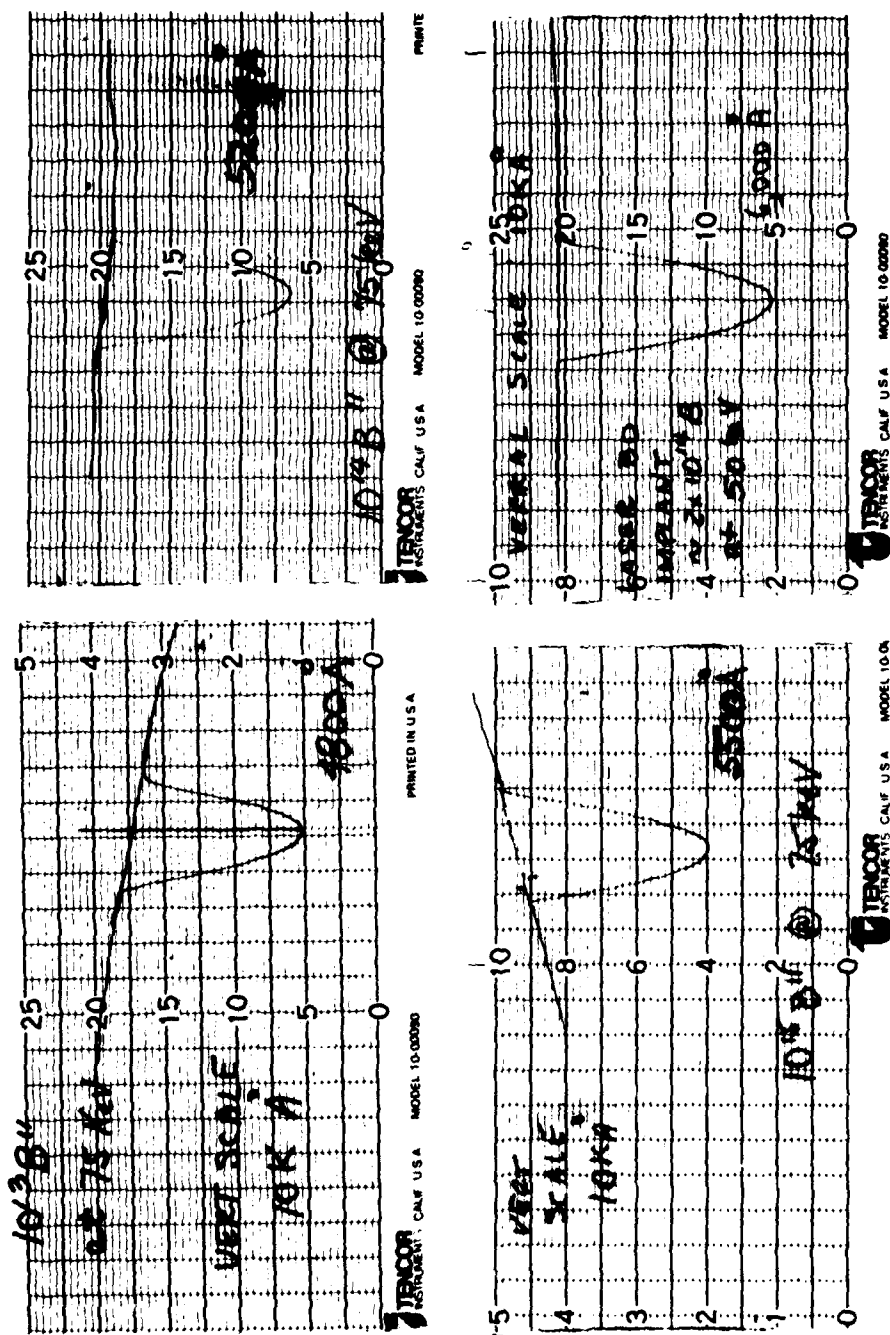


FIGURE 9. Profiles for four implantations. Horizontal scale 50:1.
Vertical scale 5000:1

4. ION MICROPROBE COMPARISONS

4.1 Preparation of Standards by Conventional Ion Implantation

In order to make ion microprobe comparisons of silicon implanted with boron by conventional techniques to silicon implanted with the laser blow-off techniques, three wafers were implanted with a conventional machine.

4.1.1 Equipment Description:

The wafers were implanted with a Varian/Extrion ion implanter model 200-20A2F with a 30CN end station. The 200-20A2F is a high throughput, multi-purpose production ion implanter with an energy range from 10 to 200 KeV. It utilizes a filament type ion source to achieve beam currents of 150 μA for boron and up to 600 μA for phosphorous and arsenic. An electrostatic deflection system is used to scan the beam. Figure 10 shows a schematic diagram of this conventional machine.

4.1.2 Process:

The wafers were implanted with B^{11+} at the fluences listed below:

<u>Dose</u>	<u>Beam Current</u>
Wafer 1: $1 \times 10^{13}/\text{cm}^2$	3.0 μA
Wafer 2: $1 \times 10^{14}/\text{cm}^2$	26.0 μA
Wafer 3: $1 \times 10^{15}/\text{cm}^2$	125.0 μA

The incident energy remained constant at 75 KeV.

An implant angle of 7° was used.

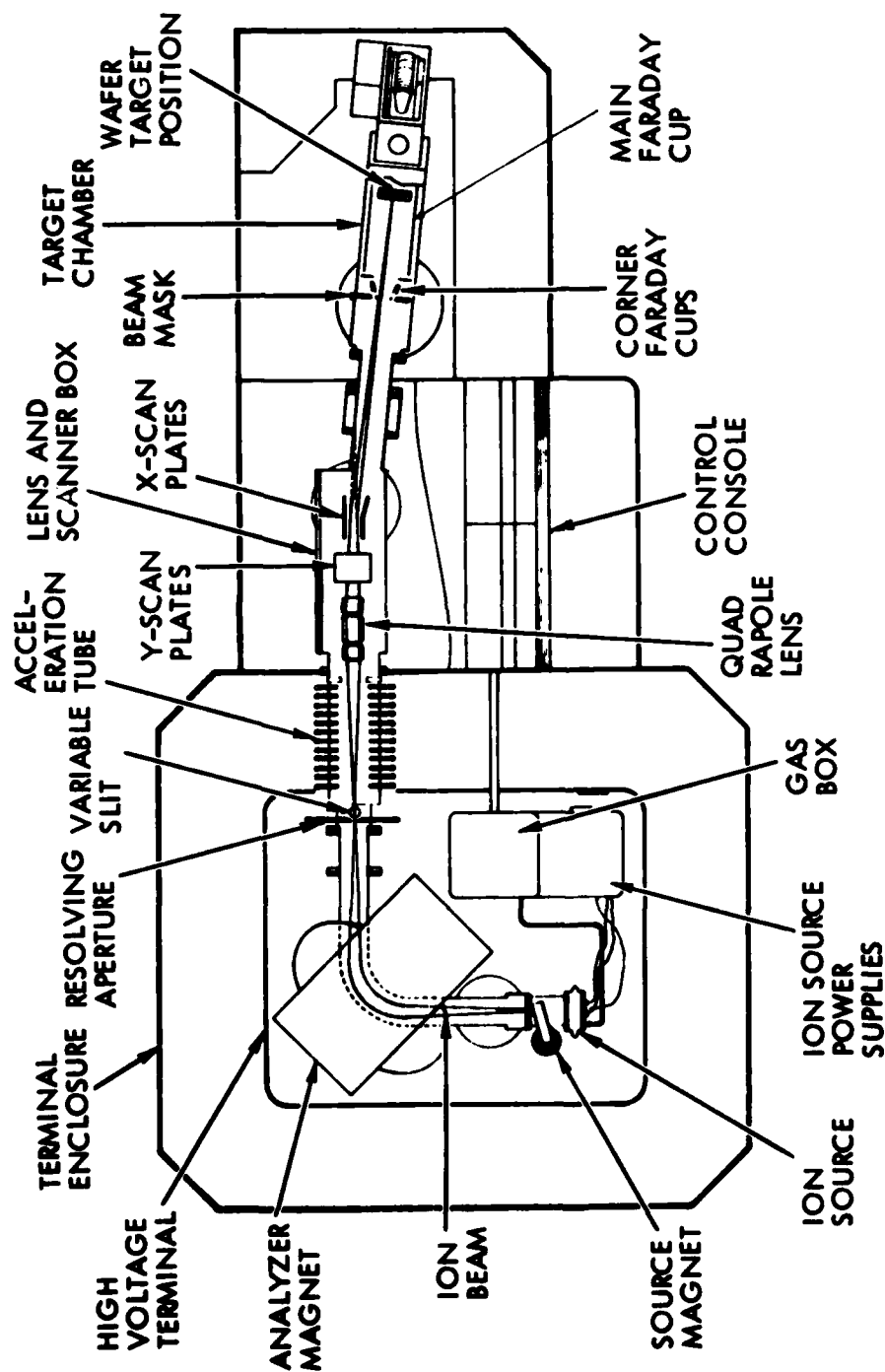


Figure 10. Schematic Diagram of Ion Implant Machine Used to Produce Standards for Comparison

4.2 Preparation of Annealed Ion Implant Standards

In order to measure the amount of boron redistribution due to annealing, and to compare any differences for the case of laser blow-off implants, silicon wafers (10 ohm-cm phosphorous-doped n-type) implanted with boron by conventional means were annealed according to the following procedures.

4.2.1 Cleaning procedure:

The wafers are loaded in a quartz carrier and cleaned in pyrex beakers.

- SN - The wafers are immersed in 3 successive baths of sulfuric acid at 150°C for 5 minutes minimum in each bath.
 - The wafers are then immersed in a nitric acid bath at 55°C for a minimum of 5 minutes.
 - The wafers are then rinsed in flowing deionized water for a minimum of 1 minute.
- OE - The wafers are immersed in 7:1 buffered oxide etch for exactly 3 seconds followed by immediately immersing in flowing deionized water for at least 1 minute.
- PA - The wafers are immersed in a 1:1 boiling mixture of freshly prepared H_2O_2 and NH_4OH for exactly 25 minutes.
- 30'R - The wafers are rinsed in flowing deionized water for exactly 30 minutes.

4.2.2 Annealing Procedure:

The wafers are annealed in a diffusion furnace tube at 900°C for 1 hour in an ambient of flowing nitrogen.

4.3 Procedure for Profiling Boron Implantation in Silicon Wafers using the Ion Microprobe (IMMA)

4.3.1 Introduction

This section outlines the procedure for determining profiles of boron implanted in silicon wafers. Only qualified personnel instructed in IMMA operation in conjunction with the system manuals supplied by the manufacturer make measurements using this procedure. The procedure describes operator functions but avoids descriptions of instrument functions.

4.3.2 Samples

4.3.2.1 Sample Preparation. The samples are prepared and identified by requestor. After samples are prepared they are stored in clean sample holders and transported to the IMMA facility.

4.3.2.2 Sample Constraints. Due to the design of the instrument sample chamber, all IMMA samples must conform to the following specifications:

- 1) The difference in thickness of the sample on a given sample holder shall not exceed ± 0.009 inches. The difference between the highest point on the sample holder and the lowest point that can be analyzed is < 0.020 inches.
- 2) The surface of the sample must be conductive. A conductive path must exist between the sample surface being analyzed and the sample holder.
- 3) The sample must be a solid.
- 4) The sample cannot exceed 1-1/4 inch in diameter.

4.3.3 Sample Receipt

The samples or sample identification are logged in the IMMA sample log book.

4.3.4 IMMA Sample Holder and Fixture Cleaning Procedure

- 1) Ultrasonic clean in acetone to remove conductive paint on sample fixture surface.
- 2) Ultrasonic clean in trichlorethylene.
- 3) Parts are thoroughly dried by placing in a clean oven at $\sim 200^{\circ}\text{C}$ for 1-2 hours.
- 4) After drying, sample fixture is stored in a clean dry area such as a desiccator containing silica gel or seal in a clean plastic bag.

4.3.5 Sample Fixture Loading

The sample or samples are attached to a clean sample holder and placed in a cleaned IMMA sample fixture. The highest point of the sample holder is made level with the top surface of the fixture. The sample fixture is placed in one of the four positions of the sample select table. A total of three fixtures can be loaded into the sample chamber. The fourth position on the sample table contains alignment standards.

4.3.6 Stage Auto Vent and Pump Down

During either stage pump down or venting operations it is unnecessary to shut down, or make adjustments to any other parts of the system. Complete sequencing of all vacuum operations is initiated in the auto vacuum mode.

4.3.6 (Continued)

It is necessary to lower the sample elevator to allow closing of the gate valve. The average pump down time is 30 minutes; however, if the stage is open for extended periods, or samples out gas heavily, pumping time extended.

4.3.7 Operating Conditions

4.3.7.1 Beam Alignment. When the chamber is pumped to 4×10^{-6} torr, the alignment standard is raised to the analyze position. The alignment is performed at the beginning of a series of samples but, no less than at the beginning of each work day.

4.3.7.2 System Operation Conditions

- 1) Cold plate on if required - LN_2
- 2) Primary beam - O_2^+ , 20 kV, 30 nA
- 3) Raster size = 100 x 100 microns
- 4) Raster rate - 100/sec
- 5) Lines/Raster - 100
- 6) Function - Cr
- 7) Scope 1 mode - XLP
- 8) Scope input - secondary ion
- 9) Sample bias - H.V. position
- 10) Scaler/timer - 100 seconds
- 11) Set aux. drive - 0.7

4.3.8 Measurements

For depth profile measurements a flow diagram is given in Figure 11. The following is a step wise operation to make said measurements.

- 1) Turn ion beam on and align beam, refer to manual for instructions. Use operating conditions described in 4.3.7.2.

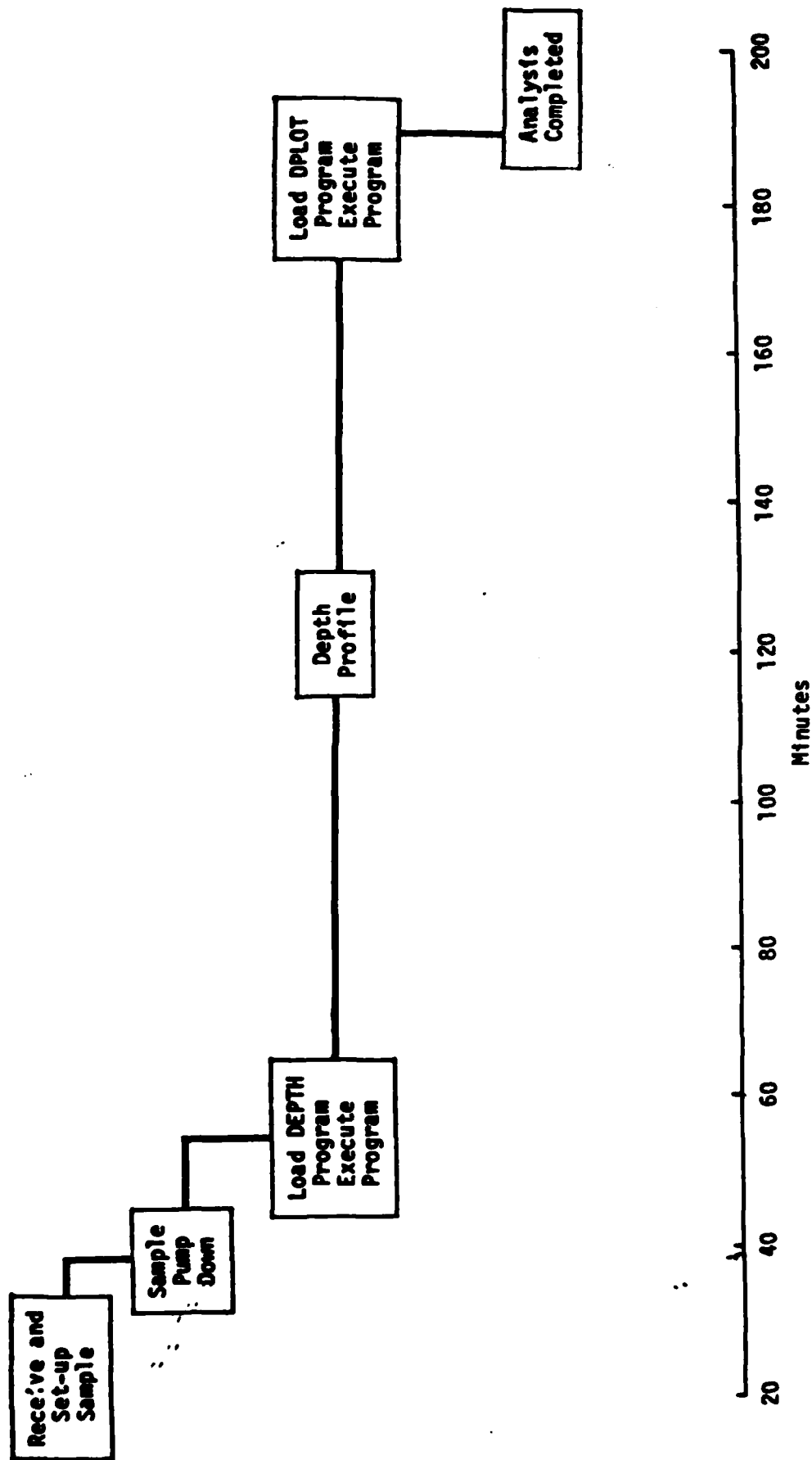


Figure 11. Flow diagram for depth profile measurements. The time scale is for one sample. More than one sample can be loaded and pumped down at the same time.

4.3.8 (Continued)

2) Tune secondary beam (refer to manual)

3) Load computer program DEPTH

a. Computer input from operator

1. Sample bias adjust - no
2. DAC adjust - yes
3. Operating conditions - (operator selected)
4. Data file identification - (operator selected)
5. Masses to be profiled
 - a) M/E 10 (B) count time = 5 sec
 - b) M/E 11 (B) count time = 5 sec
 - c) M/E 56 (Si_2) count time - 3 sec
6. Masses to be plotted - all

NOTE: M/E 28 (Si) was not used for the analysis due to after glow causing high background at M/E 10 and 11.

7. Total profile time in seconds = 0 (max. 200 cycles).

b. Execute program

NOTE: The computer drives magnet to selected mass (lowest mass first) counts for preset time. Moves to next mass, etc., and repeats cycle for total profile time while continuously sputtering into the sample. Count data is plotted and stored for future reduction. Upon completion of the profile the operator can select to repeat with same parameters on a new area of the sample or select a new sample for analysis.

4) Data Reduction

a. Load computer program DPLOT.

b. Execute program.

NOTE: Operator selects stored data input. The computer ratios M/E 10 and 11 to M/E 56 and plots data.

ION MICROPROBE MASS ANALYZER

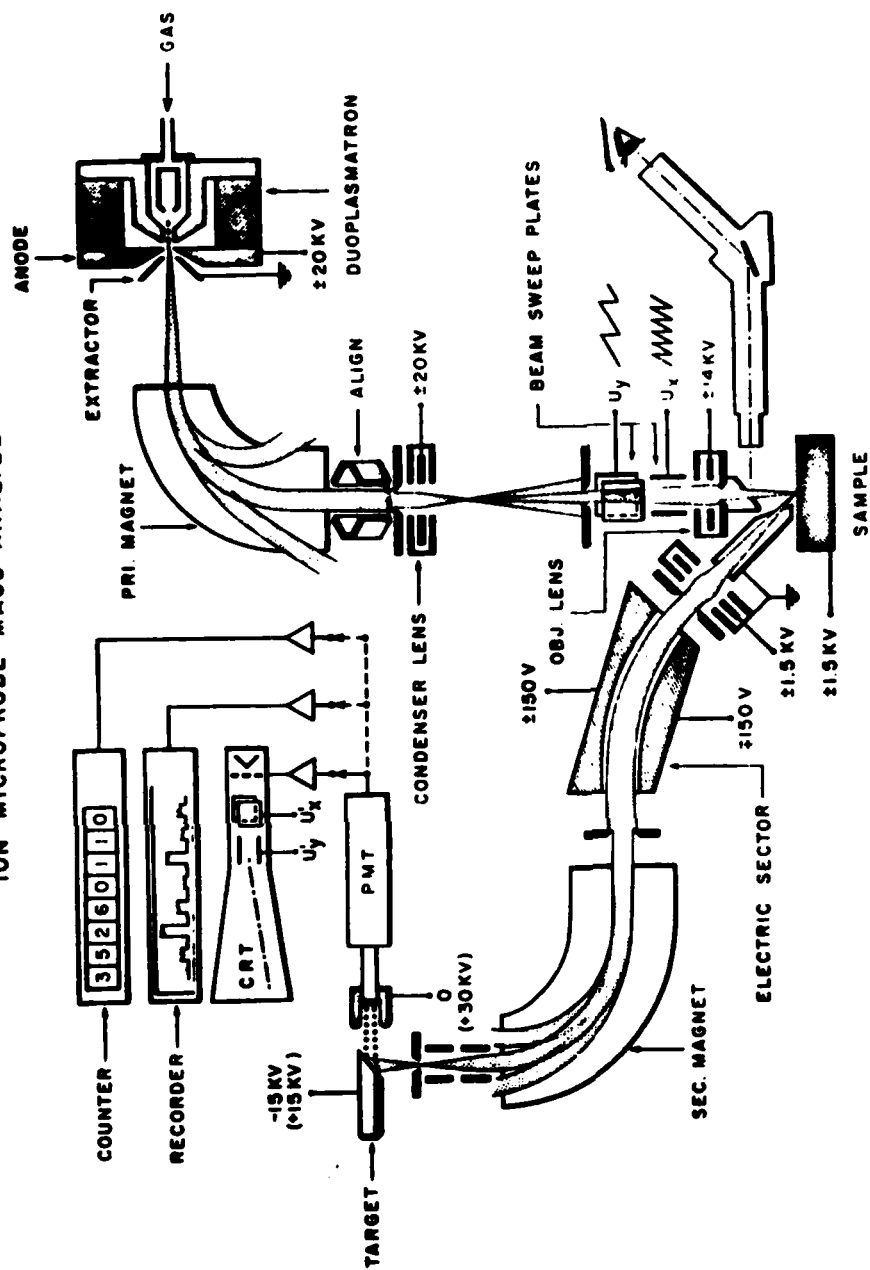


Figure 12. Applied Research Laboratories IMMA
(Ion Microprobe Mass Analyzer)

4.4 Results of Ion Microprobe Comparisons of Laser Blow-Off Ion Implants with Conventional Implants

Figure 13 shows the B depth profile obtained with the Ion Microprobe Mass Analyzer (IMMA) for the B into Si standard implanted with the conventional machine at 75 keV and a fluence of 10^{15} B/cm². The results are as expected. Except for more random noise, similar results were obtained at fluences of 10^{13} and 10^{14} B/cm², with the peaks occurring at the same sputter times. Intensities differed by factors of x10.

Figure 14 shows the B depth profile obtained with IMMA for B implanted into an identical Si wafer at 50 keV with the laser blow-off machine at a fluence of 2×10^{14} B/cm². The dashed curve shows the expected profile for a conventional implant at 50 keV. The difference is due to the presence of B⁺⁺ and B⁺⁺⁺ in the laser blow-off plasma, which are accelerated to 100 keV and 150 keV, respectively, for the 50 kV potential difference.

Although potentially a problem to some applications, it is believed that by tailoring the acceleration voltages, this high energy component will not present serious difficulties in most practical cases. See next section.

BORON IN SILICON

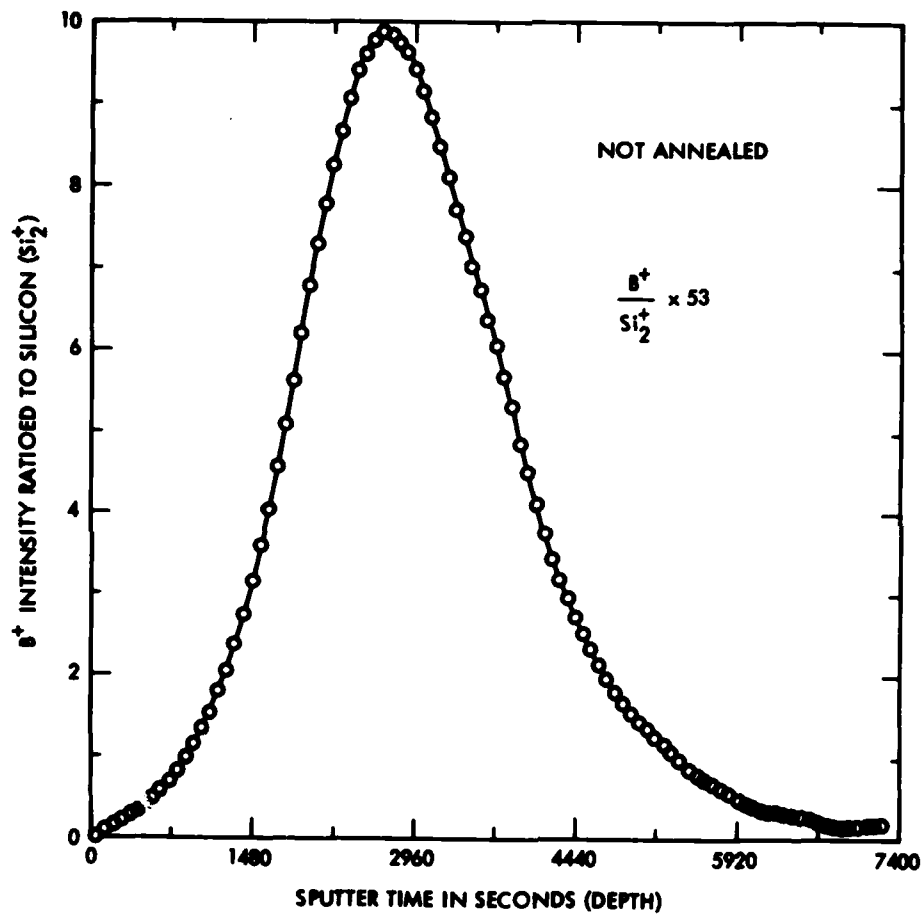


Figure 13. Ion microprobe depth profile of boron implanted into silicon by conventional ion beam implanter at 75 keV at 1×10^{15} B/cm² fluence

BORON IN SILICON

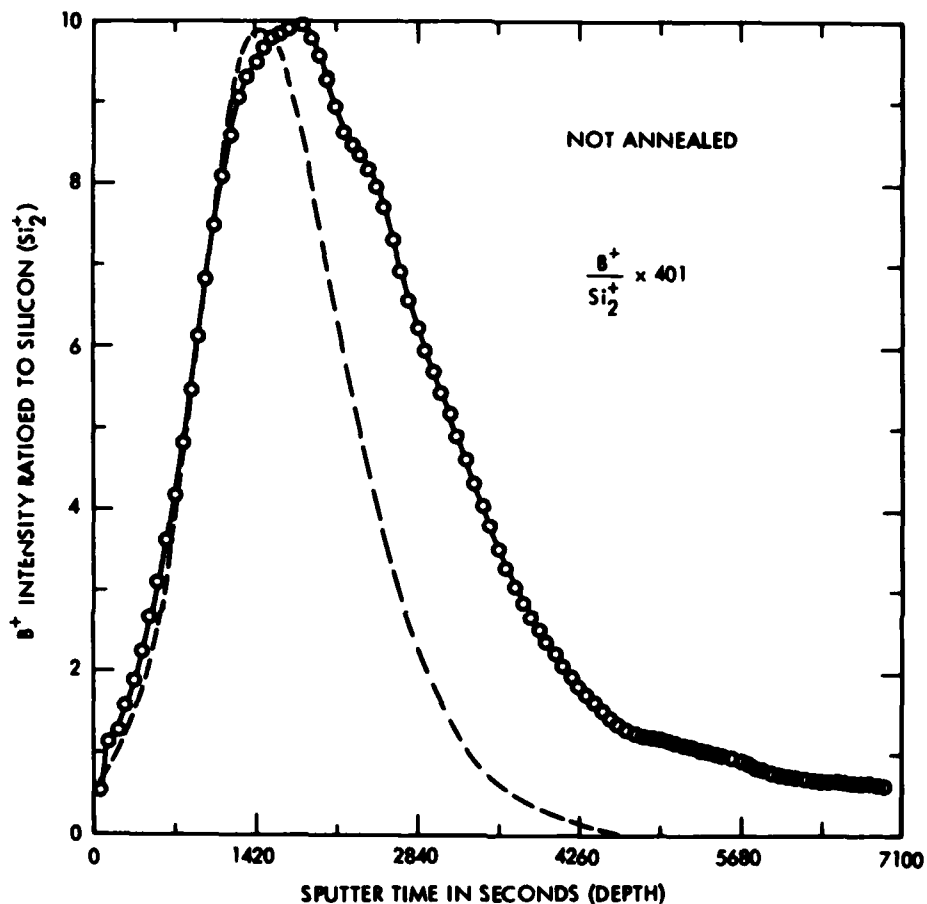


Figure 14. Ion microprobe depth profile of boron implanted into silicon with laser blow-off ion implanter at 50 keV and 2×10^{14} B/cm² fluence. Dashed curve shows profile for 50 keV conventional implant. The difference is due to plasma components of B⁺⁺ and B⁺⁺⁺ accelerated to energies of 100 and 150 keV. The abscissas should be directly comparable to the two preceding figures.

4.5 Nature of Non Mass-Analyzed Ion Implantation

Results of IMMA analysis of ion implanted impurity distributions for conventional and laser blow-off ion implantations show very clearly that for laser blow off ion implantation a significant part of the implant current is made up of multiply charged ions.

An approximation of the IMMA profile suggests that the implanted boron beam contains 60% singly charged, 30% doubly charged ions and 10% triply charged ions. Figure 15 illustrates the B distribution expected when 1×10^{14} B is implanted in a conventional implanter into silicon at 50 keV with only singly charged ions. Figure 16 illustrates the B distribution expected when 1×10^{14} B is implanted at 50 keV with 60% singly charged, 30% double charged and 10% triply charged ions. Note that in the latter case there is a significantly deeper penetration.

The deeper penetration of the multiply charged ions does not pose a serious problem since the laser blow off implanter permits the use of low implant energies. Thus the implant energy can be reduced to obtain the desired junction depth.

Figures 15 and 16 also exhibit the B profiles after an anneal of 30 minutes at 1000°C. Although it appears that the thermal effect is greater for the singly charged implantation, this is not necessarily true. The deeper multiply charged implantation has a shallower gradient. Using a lower energy for the multiply charged implant results in a shallower penetration, a steeper concentration gradient and a greater thermal diffusion as compared to results shown in Figure 16. Figure 17 illustrates the profiles obtained for multiply charged 10^{14} B implantations at 15, 20 and 25 keV. Figure 18 allows one to compare the profile of a singly charged B implantation at 50 keV with that of a multiply charged implantation of the same fluence at 20 keV. We note that both the junction depth and the concentration gradient at the junction are quite similar, leading us to conclude that a multiply charged implantation with a correctly chosen energy could be substituted for a singly charged conventional implantation.

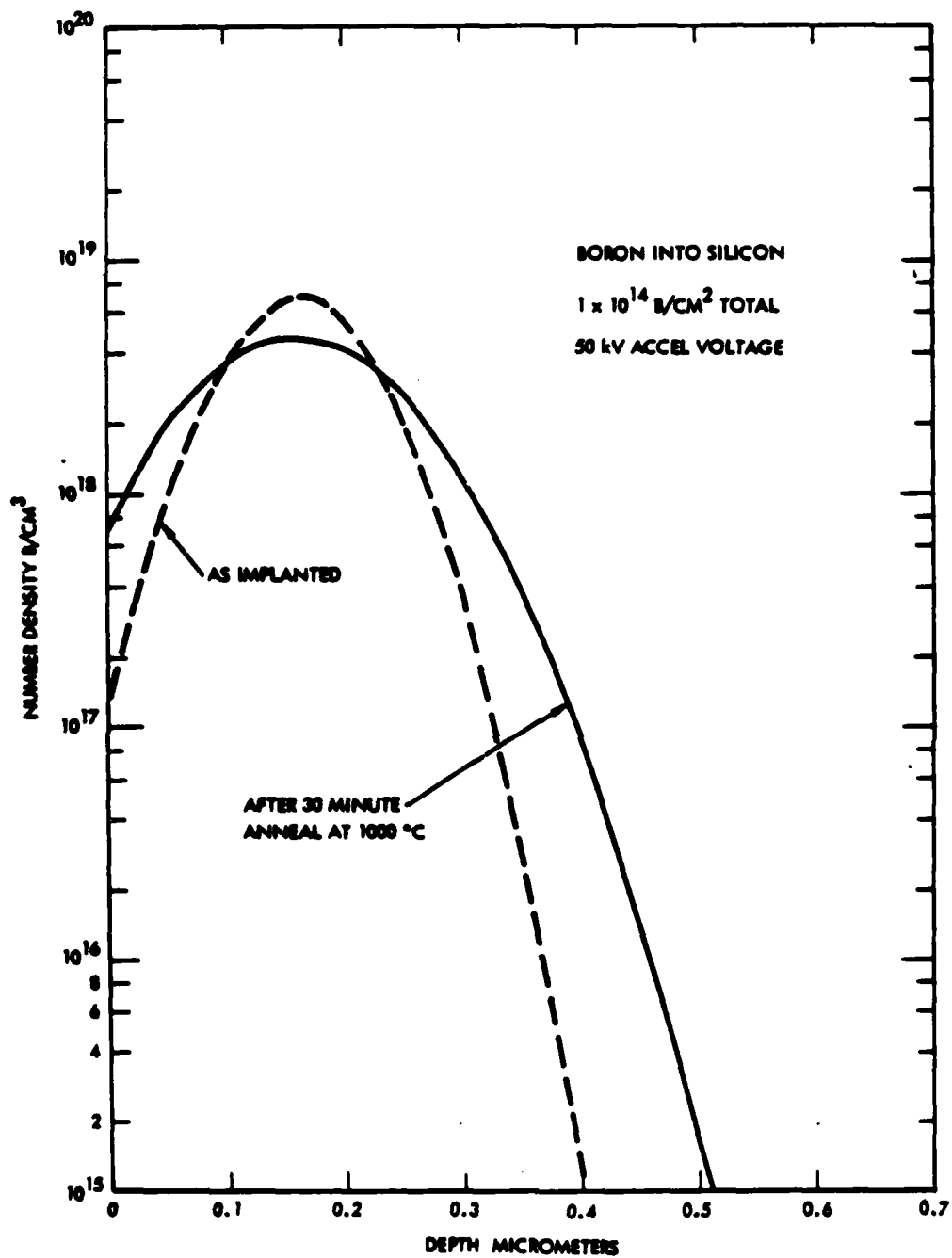


FIGURE 15. Depth Profile of Singly-Charged Ion Implantation as Implanted and after Anneal

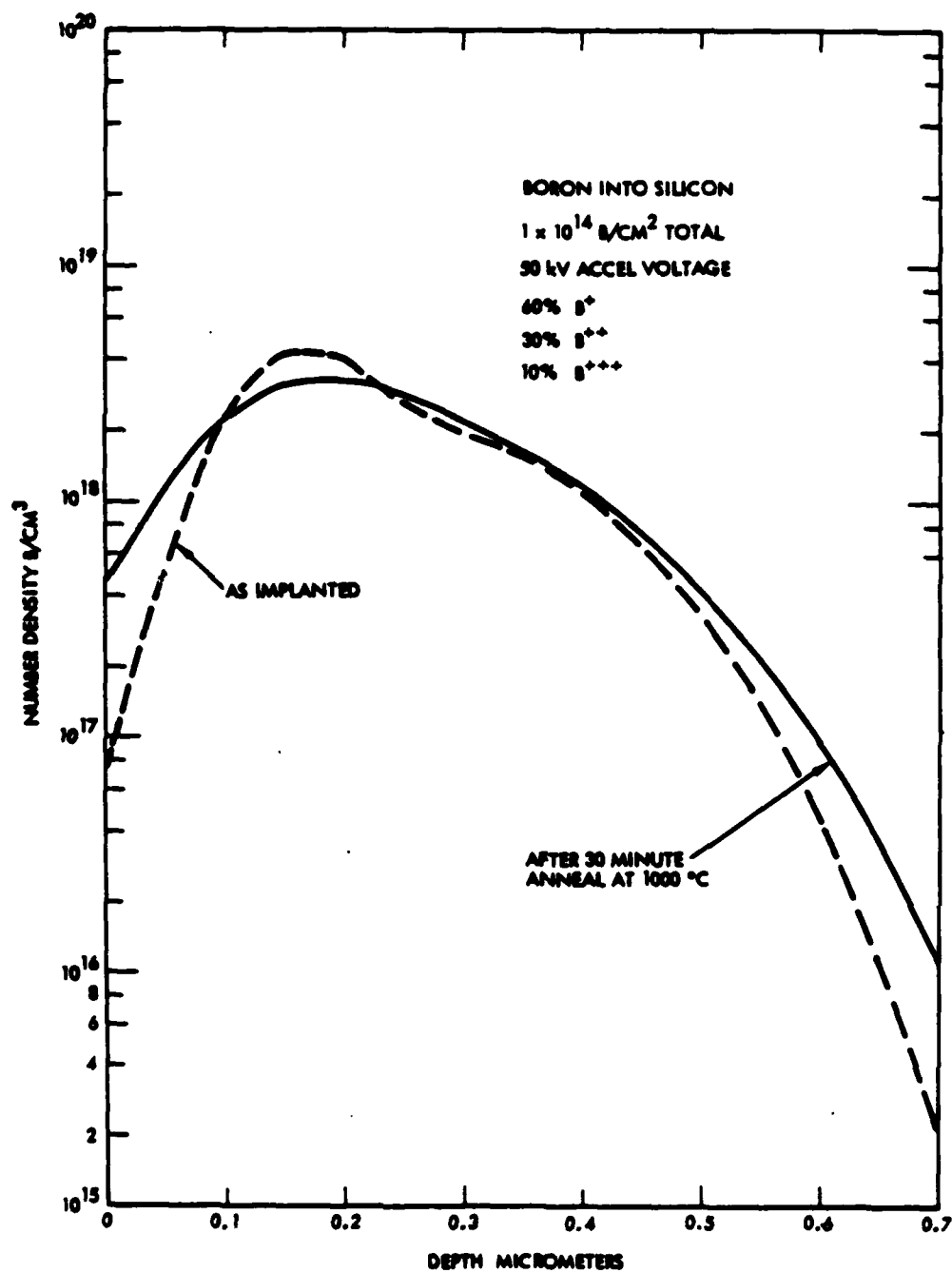


FIGURE 16. Depth Profile of Multiply-Charged Ion Implantation as Implanted and After Anneal

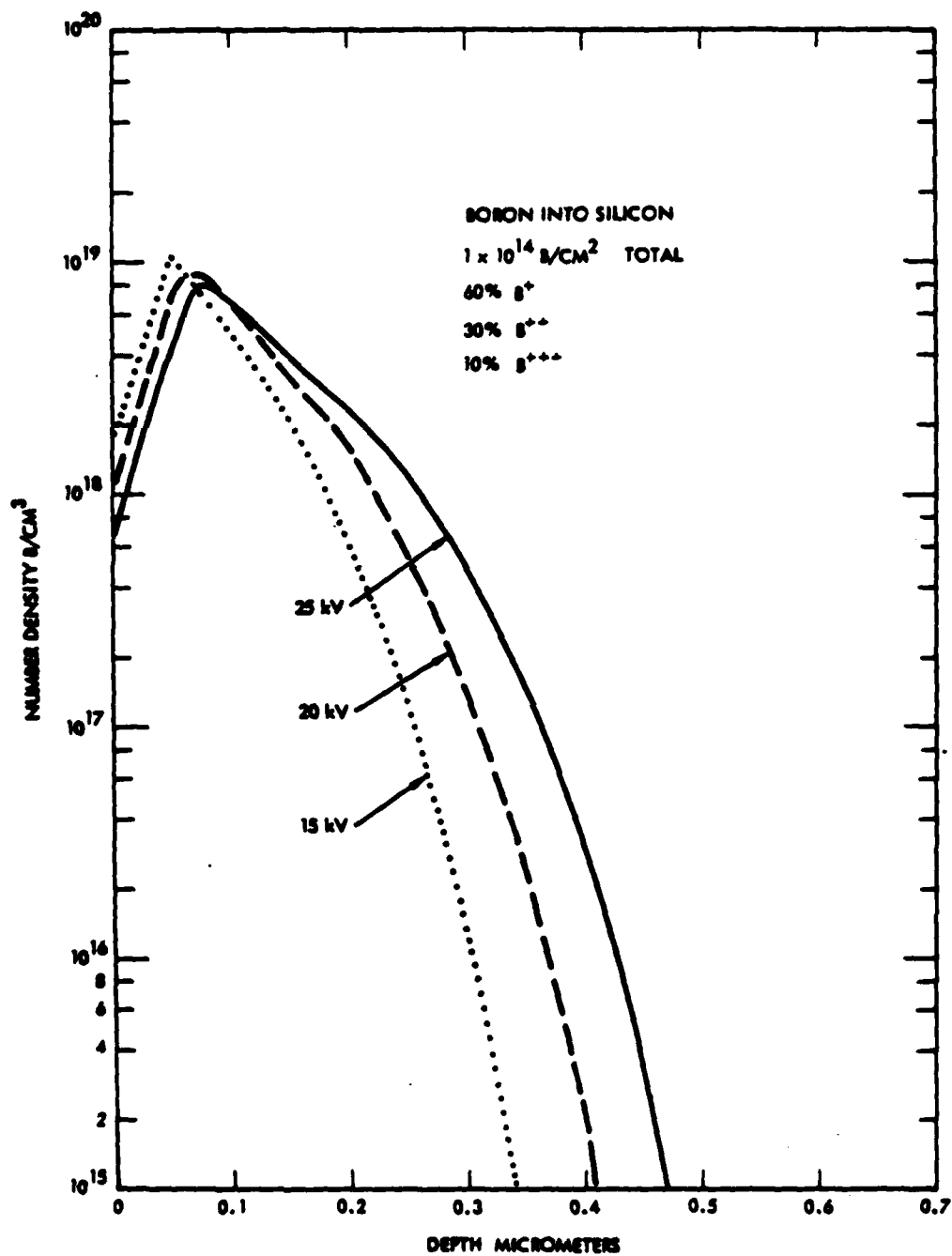


FIGURE 17. Depth Profiles of Multiply-charged Ion Implantations as Implanted at 15, 20 and 25 keV Accel Voltage

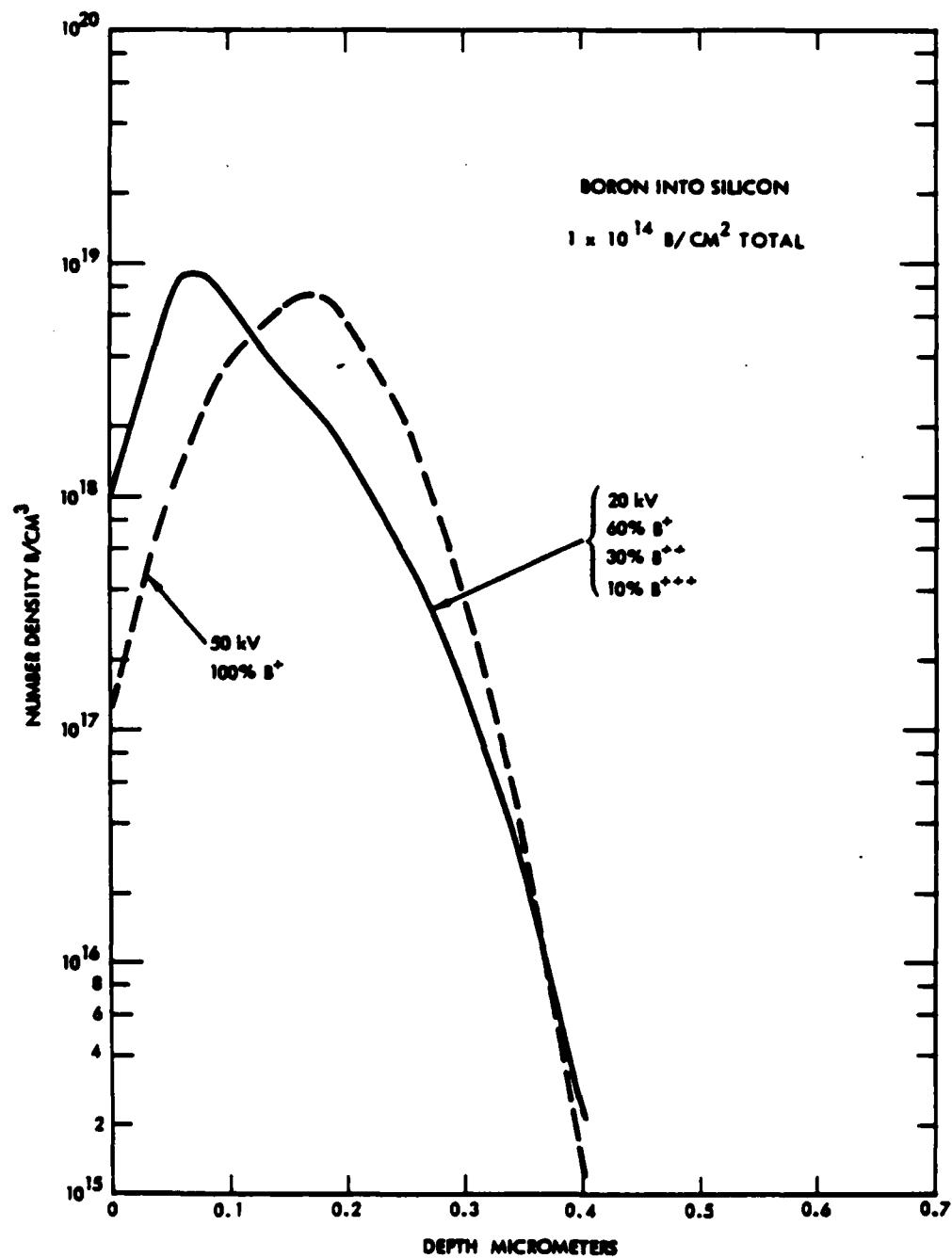


FIGURE 18. Comparison of Singly-and Multiply-Charged Ion Implantation Depth Profiles

4.6 RESULTS OF EVALUATION OF LASER BLOW-OFF ION IMPLANTED DEVICE

Laser blow-off ion implantation was utilized for base production on device test wafers. Boron was implanted into silicon at appropriate energy and dose so as to replicate the conventionally-implanted boron distribution. The devices were 16-bit multipliers.

The devices were tested after completion of fabrication. It was found that, although none of the devices (containing 10's of thousands of transistors) were entirely functional, the individual transistors showed transistor action. Beta curves are shown on Figure 19. All indications point to a boron dose too low by 15 - 20% as the source of the difficulty. Resources did not allow a repeat of the implantation and subsequent wafer processing.

These first device tests indicate that laser blow-off ion implantation is a viable method for implanting semiconductor material to produce transistors.

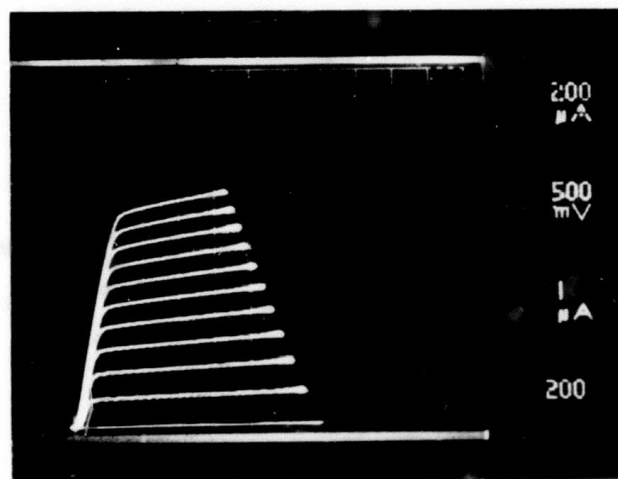
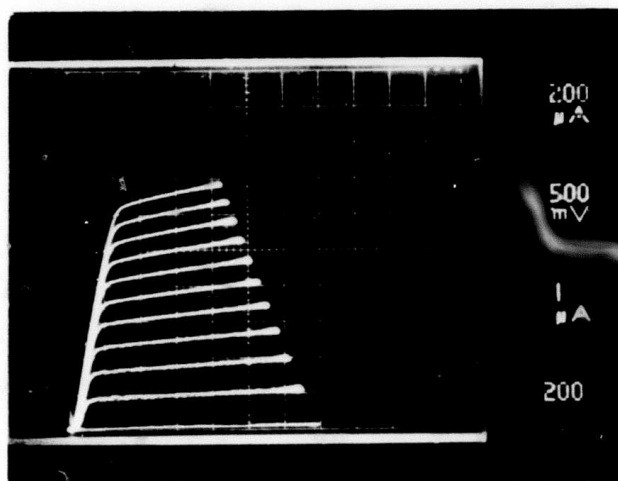


FIGURE 19. Beta Curves for Transistors Produced by Laser Blow-Off Ion Implantation. Curves show a beta of 125; top line is 10 μ A.

REFERENCES

1. J. F. Friichtenicht, N.G. Utterback, and J. R. Valles, "Intense Accelerated Metal Ion Beam Utilizing Laser Blow-Off", Rev. Sci. Instru., 47, (1976), 1489.
2. N. G. Utterback, S. P. Tang, and J. F. Friichtenicht, "Atomic and Ionic Beam Source Utilizing Pulsed Laser Blow-Off," Physics of Fluids, 19, (1976), 900.
3. K. H. Nicholas, Rad. Effects 28, 177 (1976).
4. S. Prussin, J. Appl. Physics 45, 1635 (1974).
5. S. Prussin, and Anthony M. Fern, J. Electrochem. Soc. 122, 821 (1975).
6. TRW DSSG, "Laser-Assisted Semiconductor Device Processing," Semi-Annual Technical Reports I and II, June 1978 - January 1979 and February 1979 - June 1979, DARPA Contract No. MDA 903-78-C-0284.
7. S. M. Sze, Physics of Semiconductor Devices, Wiley-Interscience, New York (1969).

APPENDIX A

THERMAL TRANSPORT IN THE TARGET MATERIAL
DURING LASER BLOW-OFF ION IMPLANTATION

THERMAL TRANSPORT IN THE TARGET MATERIAL DURING LASER BLOW-OFF IMPLANTATION

Summary

The time evolution of temperature profiles was calculated for pulsed laser blow-off ion implantation. It was shown that for practical values of ion energy and ion current density the temperatures reached in the implanted regions are too low to produce efficient self annealing by thermal effects alone of the damage created during the implantation.

Introduction

The laser blow-off implantation technique utilizes pulsed laser irradiation of a solid surface of pure dopant material to produce a high temperature plasma of dopant ions. The plasma expands into vacuum, reducing the charge density to the point where an externally applied electrical field can be used to extract ions from the plasma. In principle these ions can be accelerated to an arbitrarily high energy and can be used to implant semiconductor materials. The method offers several advantages over the conventional ion-implantation technique. The laser blow-off method is relatively simple, very fast (the pulse duration is several microseconds), permits large aerial coverage, and is amenable to a very wide range of dopant species. It has also been suggested that because of the pulsed nature of the ion beam current, the temperatures reached in the implanted region during the laser blow-off implantation could be very high. This is in contrast to the conventional implantation technique, where the host crystal remains at low temperature during the implantation. A deleterious side effect of ion implantation is damage to the host crystal caused by the high energy ions necessary to penetrate to the desired depths. This damage must be removed. This is achieved through further processing of the implanted samples, such as a high-temperature thermal annealing, or, more recently, laser-induced annealing. The possibility of reaching high temperatures in the implanted region during the laser blow-off implantation might alleviate this requirement of further processing. If sufficiently high, the temperatures produced through the use of high intensity, short duration

ion beam pulses might permit self-annealing of the implant damage during the implantation.

The present work addresses the possibility of reaching high temperatures in the implanted region during the laser blow-off. It presents the results of the thermal calculations inside the implanted material. In the model used in this work, it is assumed that the heat is generated along the path of the penetrating ions at the same rate at which the ions lose their energy. In the passage of heavy charged particles through matter, the ion energy is lost through ionization, excitation (without ionization) of atoms in the absorber, capture and loss of electrons, and elastic nuclear scattering. Thus, the assumption that the heat is generated at the same rate as the ions lose their energy implies that the transfer of the energy through these processes to the lattice proceeds at a rate which is faster than the inverse of the ion beam current pulse length. This assumption is well satisfied, the typical pulse length and thermal equilibration times being on the order of 10^{-5} sec and 10^{-8} sec, respectively.

Because of the large aerial cross-section of the beam, the thermal transport will be assumed one-dimensional in this work. Further assumptions will involve approximating the current beam pulse shape by a square shape pulse, and approximating the values of the material physical parameters by constants. These assumptions and mathematical methods are discussed in more detail in the Model Section. The results are discussed in the Discussion Section.

Model

The temperature distribution in the semiconductor in the one-dimensional approximation is obtained by solving the following thermal equation,

$$\frac{\partial T}{\partial t} - \frac{\partial}{\partial x} \left(\frac{\kappa}{c_p} \frac{\partial T}{\partial x} \right) = \frac{S}{c_p}, \quad (1)$$

where c_p and κ are the "specific" heat and thermal conductivity, respectively, and where the source function $S(S = S(x,t))$ is equal to the absorbed power per unit volume.

$$S(x,t) = \alpha(J/e), \quad (2)$$

where $\alpha(\alpha = \alpha(x,t))$ is the energy loss in the bombarded material per unit length per ion, $J(J = J(t))$ is the incident current density, and e is the charge of the electron. In (2), it has implicitly been assumed that the majority of the ions are singly ionized. Neglecting loss of heat radiated from the front surface, Equation (1) is then solved subject to the following initial and boundary conditions:

$$T(x, t = 0) = T_0 \quad (3)$$

$$\frac{\partial T(x = 0, t)}{\partial x} = 0 \quad (4)$$

$$T(x = \ell, t) = T_0 \quad (5)$$

where ℓ is the sample thickness and T_0 is temperature of the heat sink at the back side of the sample.

In Equation (1), the material constants c_p and κ are, in general, functions of temperature. However, in the temperature region of interest, c_p is practically constant, and κ varies from 1.2 W/cm°K at 300°K to .3 W/cm°K at 1000°K for pure silicon, and is lower for doped silicon.² Hence, in what follows, the temperature dependence of c_p and κ will be neglected (from our past experience^{1,3} the error introduced by approximating κ by the "average" value of $\kappa = .6$ W/cm°K is on the order of some 5% in the value of the calculated temperature profiles).

Making the approximation that c_p and κ are constant permits one to solve Equation (1) analytically by using Green's function techniques.

It is easy to verify that for the boundary conditions Equations (3)-(5), the Green's function for Equation (1) is

$$G(x, x', t-t') = \frac{1}{\sqrt{4\pi D(t-t')}} \sum_{n=-\infty}^{+\infty} (-1)^n \quad (6)$$

$$\left\{ \exp\left(\frac{-(x-x' - 2n\ell)^2}{4D(t-t')}\right) + \exp\left(\frac{-(x+x' - 2n\ell)^2}{4D(t-t')}\right) \right\},$$

where the diffusion constant $D \equiv \kappa/c_p$. The temperature distribution is the convolution of the Green's function and the source term S ,

$$\Delta T(x, t) \equiv T(x, t) - T_0 = \int_0^\infty dx' \int_0^t G(x, x', t-t') S(x', t')/c_p. \quad (7)$$

Assuming the slab thickness $\ell \gg (x_R, x_{th})$, where x_R is the "range" of the implanted ions, and x_{th} is a characteristic thermal diffusion length, $x_{th} = \sqrt{4D t_p}$, where t_p is the pulse length, the semiconductor can be replaced by a semi-infinite medium, with the result that the summation \sum_n in Equation (6) reduces to only one term, namely the term $n = 0$. Substituting the resulting equation into Equation (7) then yields

$$\Delta T(x, t) = \sum_{(+,-)} \frac{1}{c_p} \int_0^\infty dx' \int_0^t dt' \frac{\exp\left(\frac{-(x \pm x')^2}{4D(t-t')}\right)}{\sqrt{4\pi D(t-t')}} S(x', t'). \quad (8)$$

In Equation (8), the source term S is generally time and coordinate-dependent. The coordinate dependence arises because of the dependence of the ion energy loss α on depth below the material surface. The time dependence arises primarily because of the pulse shape, and, to a lesser extent, because of a finite transit time in the material before the ions stop and transfer their energy to the crystalline lattice. However, for typical parameters of interest, the stopping time has been estimated to be on the order of 10^{-12} to 10^{-11} sec. This is much shorter than the typical pulse length t_p of several microseconds.¹ Thus, the time dependence of α can be neglected. The shape of the current pulse has been described in Reference (1). The shape somewhat resembles the "Gaussian" pulse shape,

$$J(t) = \begin{cases} J_0 \left(1 - \frac{(t - t_m)^2}{t_m^2} \right) & 0 < t < t_m \\ J_0 e^{- (t - t_m)^2 / t_m^2} & \text{otherwise,} \end{cases} \quad (9)$$

where t_m is the time at which the pulse reaches its maximum value J_0 . Again, from our past experience,⁸ we have found that by approximating the Gaussian pulse shape by a square shape pulse,

$$J(t) = \begin{cases} J_0 & 0 < t < t_p \\ 0 & \text{Otherwise,} \end{cases} \quad (10)$$

where the pulse length $t_p = 2 t_m$, introduces a very small error (some 5%) into our final results. Furthermore, using the square shape pulse permits us to integrate Equation (8) analytically. Therefore, in what follows, we shall approximate the current pulse by a square shape pulse.

Finally, the energy loss per unit length will be approximated by a constant,

$$\alpha \approx \frac{Ee}{x_R}, \quad (11)$$

where E is the ion energy (in electron volts), and x_R is the projected range. A better approximation to α can be obtained through the use of the specific ionization curves for passage of heavy charged particles through matter, discussed in Reference 4. From Reference 4, a typical specific ionization curve for a heavy charged particle starts at the surface at about 1/2 of its maximum value, then slowly rises with depth beneath the surface, reaches its maximum value at some distance x_m , and then falls abruptly to zero. A typical (normalized) plot of the specific ionization $I(x)$ is shown in Figure 1. However, as has already been discussed in the Introduction Section, other processes such as host atom excitation, capture and loss of electrons, and nuclear scattering, also contribute to the ion energy loss. Thus, the coordinate dependence of the energy loss α per unit length will not necessarily correspond exactly to the specific ionization curve. In the spirit of the other approximations in this calculation, we shall approximate α by a constant, chosen such that the product of α and projected range x_R is equal to the ion energy eE (see Equation (11)).

Making the above discussed approximations, the source term $S(x,t)$ reduces to a constant for times $0 < t < t_p$ and coordinates $0 < x < x_R$, and is equal to zero otherwise. Substituting $S(x,t)$ into Equation (8) and making the change of variables $t - t' = t''$ and $x'' = (x + x')/\sqrt{4Dt''}$ then yields

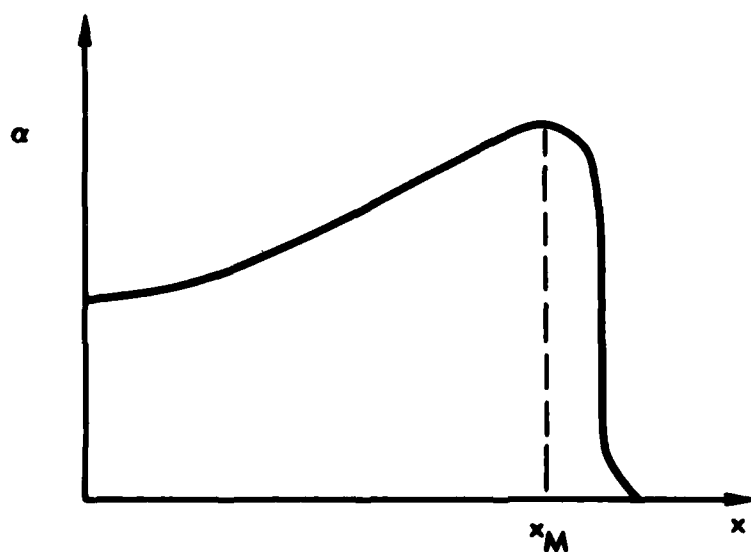


Figure 1. A typical average specific ionization along a collimated beam of heavy particles in matter

$$\Delta T(x,t) = \frac{J_0}{c_p} \frac{E}{ex_R} \sum_{(+,-)} \int_{t_0}^t \frac{dt'}{\sqrt{4\pi Dt'}} \int_0^{x_R} dx \exp\left(-\frac{(x \pm x')^2}{4Dt'}\right) \quad (12)$$

$$= \frac{J_0}{c_p} \frac{E}{ex_R} \sum_{(+,-)} \int_{t_0}^t \frac{dt'}{2} (\pm) \operatorname{erf}\left(\frac{x \pm x_R}{\sqrt{4Dt'}}\right) .$$

In Equation (12), the time t_0 is $t_0 = \max(t - t_p, 0)$

$$t_0 = \begin{cases} t - t_p & t \geq t_p \\ 0 & t \leq t_p \end{cases} \quad (13)$$

Equation (12) can be evaluated by using changes of variables and partial fractions. First, using the change of variables $1/\sqrt{t''} = (x_R \pm x)/\sqrt{4Dt'}$ $\operatorname{sign}(x_R \pm x)$, where $\operatorname{sign}(x) = \pm 1$ for $x \gtrless 0$, Equation (12) transforms into

$$\Delta T' \equiv \frac{\Delta T}{(J_0 E / ec_p x_R)} = \frac{1}{8D} \sum_{(\pm)} \operatorname{sign}(x_R \pm x) (x \pm x_R)^2 \int_{t_1^{(\pm)}}^{t_2^{(\pm)}} dt' \operatorname{erf}\left(\frac{1}{\sqrt{t'}}\right) \quad (14)$$

where the lower and upper integral boundaries are

$$t_1^{(\pm)} = 4Dt_0 / (x \pm x_R)^2$$

$$t_2^{(\pm)} = 4Dt / (x \pm x_R)^2 . \quad (15)$$

Application of a partial fraction to Equation (14) yields:

$$\Delta T' = \frac{1}{8D} \sum_{(\pm)} \text{sign}(x_{R \pm x})(x_{R \pm x})^2 \left\{ \left[t' \operatorname{erf} \frac{1}{\sqrt{t'}} \right]_{t_1^{(\pm)}}^{t_2^{(\pm)}} + \frac{1}{\sqrt{\pi}} \int_{t_1^{(\pm)}}^{t_2^{(\pm)}} \frac{dt'}{t'^{1/2}} e^{-1/t'} \right\} \quad (16)$$

The second bracketed term on the right hand side of Equation (16) is evaluated by using the change of variables $t'^{1/2} = 1/x$ and a partial fraction. This yields:

$$\begin{aligned} \int_{t_1}^{t_2} \frac{dt}{t^{1/2}} e^{-1/t} &= - \int_{x_1}^{x_2} \frac{2dx}{x^2} e^{-x^2} = 2 \left\{ \frac{e^{-x^2}}{x} + 2 \int_{x_1}^{x_2} dx e^{-x^2} \right\} \\ &= 2 \left\{ \frac{e^{-x^2}}{x} + \sqrt{\pi} \operatorname{erf}(x) \right\}_{x_1}^{x_2} \end{aligned} \quad (17)$$

Substituting Equation (17) into Equation (16) finally yields:

$$\Delta T' = \frac{c_p}{8\kappa} \sum_{(\pm)} \text{sign}(x_{R \pm x})(x_{R \pm x})^2 \left\{ (2+t') \operatorname{erf} \left(\frac{1}{\sqrt{t'}} \right) + 2 \sqrt{\frac{t'}{\pi}} e^{-1/t'} \right\}_{t_1^{(\pm)}}^{t_2^{(\pm)}} \quad (18)$$

where the lower and upper boundaries $t_1^{(\pm)}$ and $t_2^{(\pm)}$ are given by Equation (15).

Results and Discussion

Equation (18) was evaluated numerically for several values of the current pulse length t_p , and several values of the ion energy E . The implanted ions were boron. The projected range x_R , corresponding to a particular energy E , is tabulated in Table 1. The energy ranged from 20 keV to 180 keV, and the corresponding projected range was from .0662 μm to .4872 μm . The pulse length ranged from $t_p = 10 \mu\text{sec}$ to $t_p = 40 \mu\text{sec}$. The substrate material was silicon. The material parameters were $c_p = 1.6 \text{ J/cm}^3\text{K}$, and $\kappa = .6 \text{ W/cm}^2\text{K}$.

Samples of the numerical results are shown in Figure 2-6. The temperature profiles are shown as a function of the normalized distance x/x_R away from the semiconductor front surface, with time (in fractions and multiples of the pulse length t_p) as a parameter. The temperature shown is a temperature rise per unit current density $J_0 (\text{A/cm}^2)$.

Inspecting the calculated profiles, the main results of this calculation can be summarized as follows:

- a. The temperature is linearly proportional to current.
- b. The maximum temperature is reached at the end of the ion beam pulse, at time $t = t_p$.
- c. The temperature profiles are thermal diffusion-limited.

The conclusions are physically easily understood. The profiles are thermal diffusion-dominated because, for the beam and material parameters used, the projected range is much smaller than the thermal diffusion length, $x_R \ll x_{th}$, where a typical value of x_{th} is $x_{th} = \sqrt{4\kappa t_p / c_p} \approx 8 \times 10^{-3} \text{ cm}$ for $t_p = 40 \mu\text{sec}$. From this follows that, for example, for $t_p = 40 \mu\text{sec}$, current density 1 amp/cm^2 and the ion energy $E = 200 \text{ keV}$, the effective heated depth is $x_{th} \approx 8 \times 10^{-3} \text{ cm}$, the associated rise in the silicon temperature is

LSS RANGE STATISTICS FOR									
BORON IN SILICON									
	ENERGY (KEV)	PROJECTED RANGE (MICRONS)	STANDARD DEVIATION (MICRONS)	THIRD MOMENT RATIO ESTIMATE	LATERAL STANDARD DEVIATION (MICRONS)	RANGE (MICRONS)	STANDARD DEVIATION (MICRONS)	NUCLEAR ENERGY LOSS (KEV/MICRON)	ELECTRONIC ENERGY LOSS (KEV/MICRON)
SUBSTRATE PARAMETERS	10	0.0333	0.0171	-0.031	0.0236	0.0423	0.0141	0.0466	0.1022
	20	0.0442	0.0283	-0.109	0.0409	0.1100	0.0221	0.1589	0.1443
	30	0.0597	0.0371	-0.403	0.0555	0.1536	0.0276	0.2309	0.1798
	40	0.1102	0.0643	-0.417	0.0682	0.1960	0.0316	0.3435	0.2035
	50	0.1608	0.0956	-0.727	0.0793	0.2317	0.0347	0.4812	0.2234
	60	0.1903	0.0756	-0.821	0.0891	0.2673	0.0371	0.6428	0.2421
	70	0.2188	0.0601	-0.904	0.0980	0.3030	0.0392	0.8345	0.2649
	80	0.2465	0.0461	-0.978	0.1061	0.3391	0.0409	0.1060	0.2822
	90	0.2733	0.2677	-1.046	0.1135	0.3638	0.0424	0.1345	0.2944
	100	0.2954	0.0713	-1.108	0.1203	0.3894	0.0437	0.1645	0.3134
ANALYST	110	0.3248	0.0739	-1.166	0.1265	0.4210	0.0449	0.2028	0.3277
	120	0.3496	0.0765	-1.223	0.1325	0.4494	0.0459	0.2485	0.3411
	130	0.3737	0.0797	-1.271	0.1380	0.4761	0.0468	0.2975	0.3558
	140	0.3974	0.0823	-1.319	0.1431	0.5023	0.0476	0.3475	0.3695
	150	0.4203	0.0834	-1.364	0.1480	0.5272	0.0484	0.3980	0.3826
	160	0.4432	0.0854	-1.408	0.1525	0.5518	0.0491	0.4485	0.3953
	170	0.4654	0.0872	-1.449	0.1569	0.5759	0.0497	0.4985	0.4076
	180	0.4872	0.0893	-1.489	0.1610	0.5993	0.0503	0.5475	0.4195
	190	0.5086	0.0906	-1.527	0.1649	0.6223	0.0509	0.5955	0.4309
	200	0.5297	0.0921	-1.564	0.1687	0.6448	0.0514	0.6425	0.4418
SNO	210	0.5506	0.0937	-1.600	0.1725	0.6666	0.0523	0.6885	0.4521
	220	0.5708	0.0952	-1.636	0.1757	0.6880	0.0532	0.7335	0.4618
	230	0.5908	0.0975	-1.671	0.1789	0.7090	0.0539	0.7775	0.4708
	240	0.6098	0.0999	-1.706	0.1821	0.7298	0.0546	0.8205	0.4795
	250	0.6285	0.1020	-1.740	0.1853	0.7503	0.0552	0.8625	0.4878
	260	0.6465	0.1040	-1.774	0.1885	0.7705	0.0558	0.9035	0.4958
	270	0.6645	0.1059	-1.808	0.1916	0.7905	0.0564	0.9435	0.5035
	280	0.6825	0.1076	-1.842	0.1946	0.8103	0.0569	0.9825	0.5108
	290	0.7005	0.1092	-1.876	0.1975	0.8298	0.0573	1.0205	0.5178
	300	0.7185	0.1107	-1.910	0.2003	0.8490	0.0578	1.0575	0.5245
ION: BORON	310	0.7365	0.1121	-1.944	0.2030	0.8680	0.0582	1.0935	0.5308
	320	0.7545	0.1136	-1.978	0.2057	0.8868	0.0586	1.1285	0.5368
	330	0.7725	0.1147	-2.012	0.2083	0.9053	0.0589	1.1625	0.5425
	340	0.7905	0.1159	-2.046	0.2108	0.9235	0.0593	1.1955	0.5478
	350	0.8085	0.1171	-2.080	0.2134	0.9413	0.0596	1.2275	0.5528
	360	0.8265	0.1182	-2.114	0.2159	0.9588	0.0599	1.2585	0.5575
	370	0.8445	0.1194	-2.148	0.2183	0.9760	0.0603	1.2885	0.5620
	380	0.8625	0.1205	-2.182	0.2206	0.9928	0.0606	1.3175	0.5662
	390	0.8805	0.1216	-2.216	0.2228	1.0093	0.0609	1.3455	0.5702
	400	0.8985	0.1227	-2.250	0.2249	1.0255	0.0613	1.3725	0.5738
EISEN	410	0.9165	0.1238	-2.284	0.2269	1.0413	0.0616	1.3985	0.5772
	420	0.9345	0.1249	-2.318	0.2288	1.0568	0.0619	1.4235	0.5805
	430	0.9525	0.1259	-2.352	0.2306	1.0720	0.0622	1.4475	0.5835
	440	0.9705	0.1269	-2.386	0.2323	1.0868	0.0625	1.4705	0.5862
	450	0.9885	0.1279	-2.420	0.2339	1.1018	0.0628	1.4925	0.5888
	460	1.0065	0.1289	-2.454	0.2354	1.1165	0.0631	1.5135	0.5912
	470	1.0245	0.1299	-2.488	0.2368	1.1308	0.0634	1.5335	0.5935
	480	1.0425	0.1309	-2.522	0.2381	1.1448	0.0637	1.5525	0.5955
	490	1.0605	0.1319	-2.556	0.2393	1.1585	0.0640	1.5705	0.5972
	500	1.0785	0.1329	-2.590	0.2405	1.1718	0.0643	1.5875	0.5988
ELECTRONIC CROSS SECTIONS OF									
EISEN									
WORTHCLIFFE CONSTANT 0.252E 04									

SILICON

BORON



Table 1. LSS Range Statistics for Boron Implanted in Silicon

BORON INTO SILICON
 TEMPERATURE RISE PER UNIT CURRENT DENSITY J
 PULSE LENGTH $t_p = 1.0 \text{ E} - 05 \text{ sec}$
 ENERGY $E = 2.0 \text{ E} + 04 \text{ eV}$
 RANGE $R = 6.6200 \text{ E} - 06 \text{ cm}$
 $J(\text{A}/\text{cm}^2)$; TEMP($^{\circ}\text{K}$)

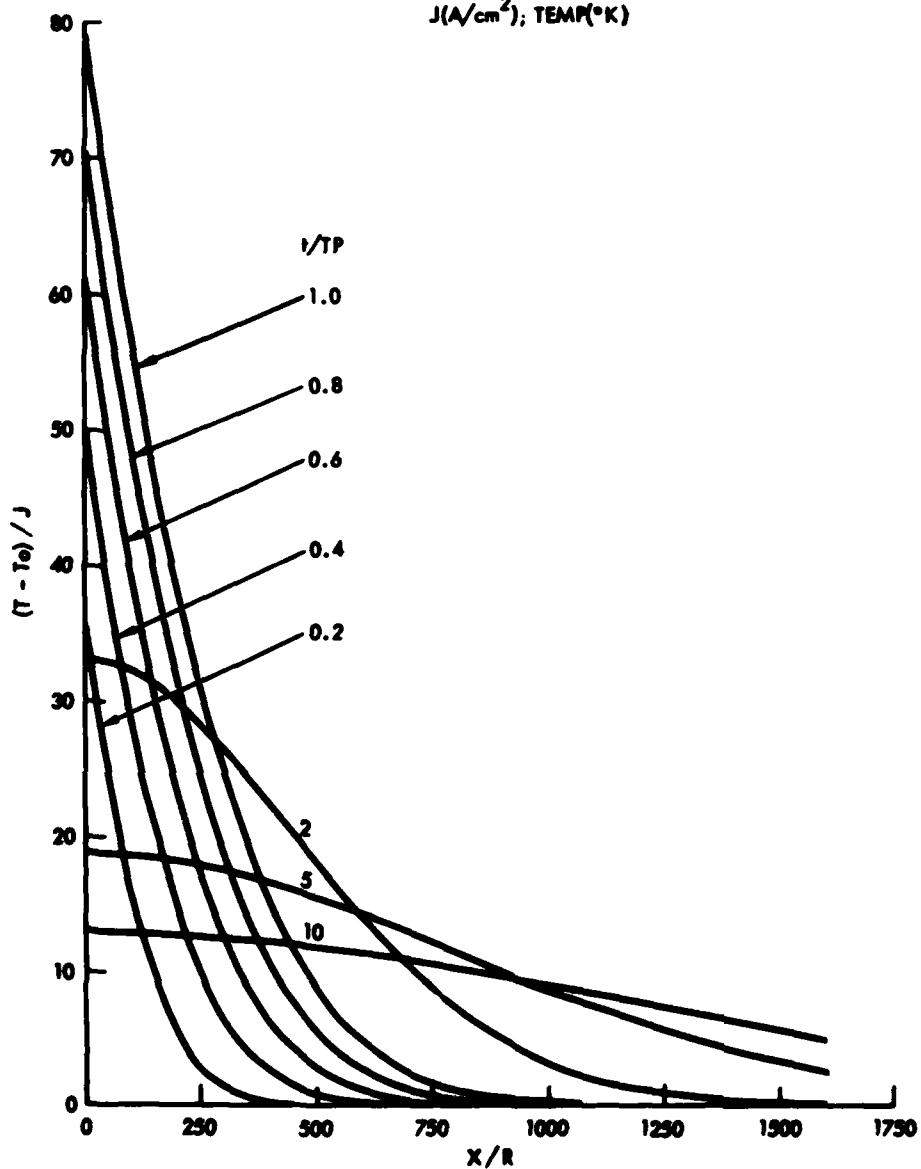


Figure 2. Temperature profiles for pulsed laser blowoff per unit current density J . Pulse length $t_p = 10^{-5} \text{ sec}$, ion energy $e = 20 \text{ keV}$, projected range $R = 6.62 \times 10^{-6} \text{ cm}$.

BORON INTO SILICON
TEMPERATURE RISE PER UNIT CURRENT DENSITY J

PULSE LENGTH $t_p = 1.0 \text{ E} - 05 \text{ sec}$

ENERGY $E = 1.0 \text{ E} + 05 \text{ eV}$

RANGE $R = 2.9940 \text{ E} - 05 \text{ cm}$

$J(\text{A}/\text{cm}^2); \text{TEMP}(\text{°K})$

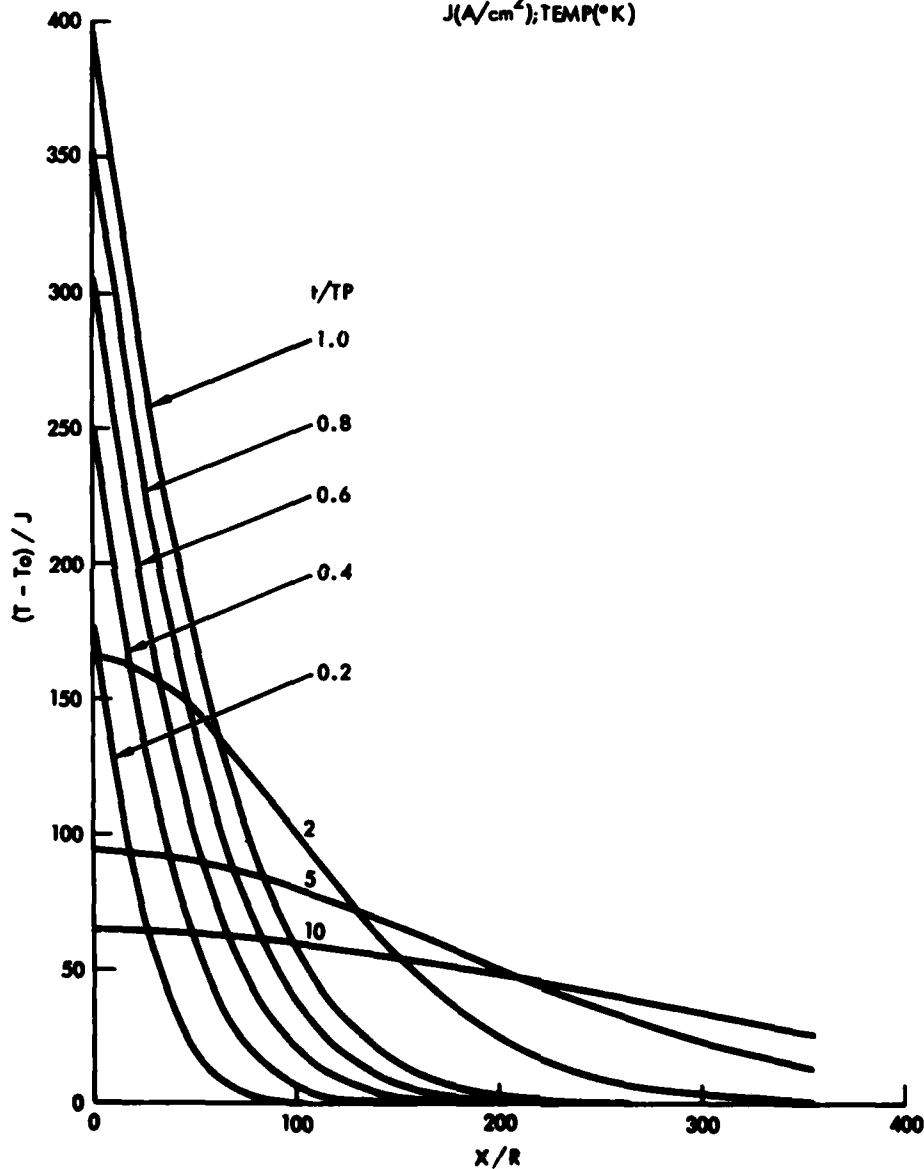


Figure 3. Temperature profiles for pulsed laser blowoff per unit current density J . Pulse length $t_p = 10^{-5}$ sec, ion energy $E = 100$ keV, projected range $R = 2.994 \times 10^{-5}$ cm.

BORON INTO SILICON
TEMPERATURE RISE PER UNIT CURRENT DENSITY J

PULSE LENGTH $t_p = 2.0 \times 10^{-5}$ sec

ENERGY $E = 1.0 \times 10^5$ eV

RANGE $R = 2.9940 \times 10^{-5}$ cm

$J(\text{A/cm}^2)$; TEMP($^{\circ}\text{K}$)

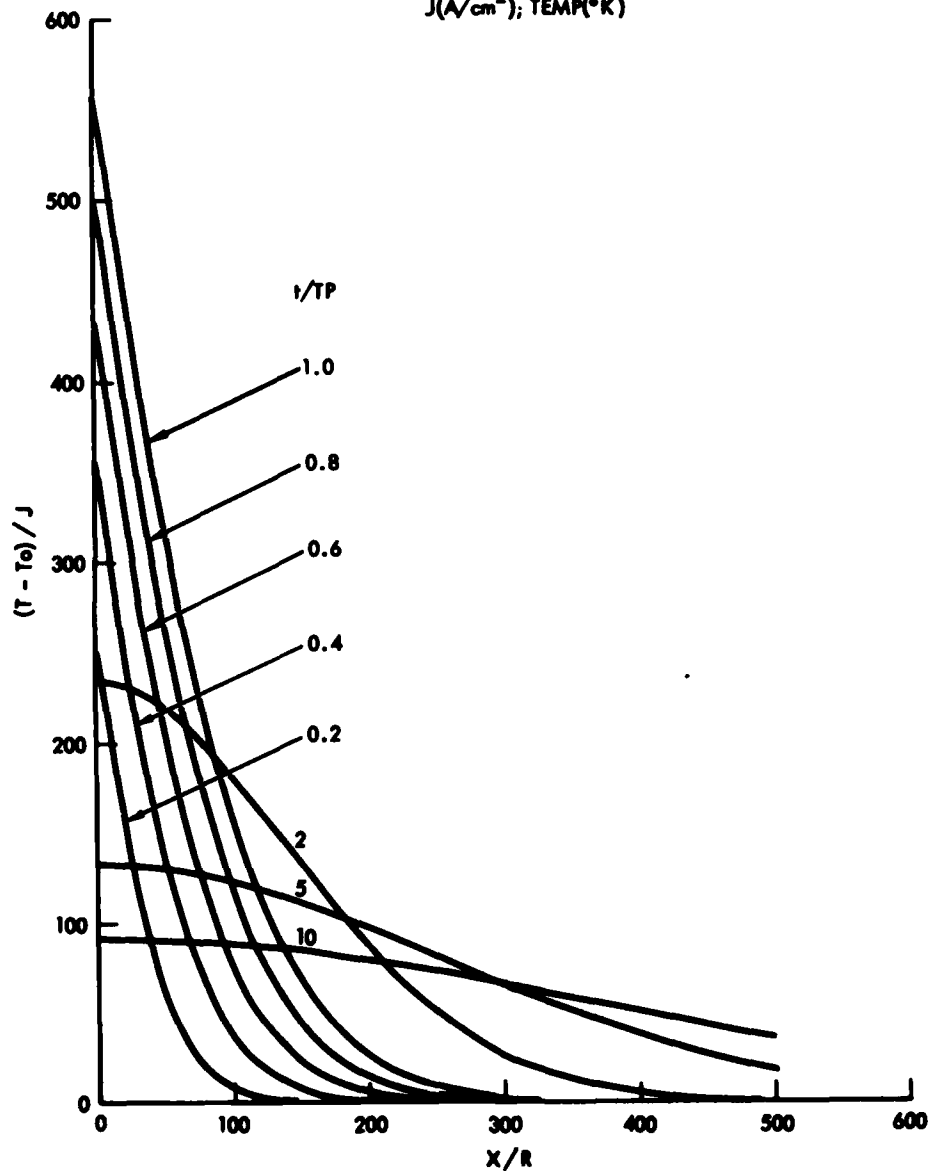


Figure 4. Temperature profiles for pulsed laser blowoff per unit current density J. Pulse length $t_p = 2 \times 10^{-5}$ sec, ion energy $E = 100$ keV, projected range $R = 2.994 \times 10^{-5}$ cm

BORON INTO SILICON
TEMPERATURE RISE PER UNIT CURRENT DENSITY J

PULSE LENGTH $t_p = 4.0 \times 10^{-5}$ sec

ENERGY $E = 1.0 \times 10^5$ eV

RANGE $R = 2.9940 \times 10^{-5}$ cm

$J(\text{A}/\text{cm}^2)$; TEMP($^{\circ}\text{K}$)

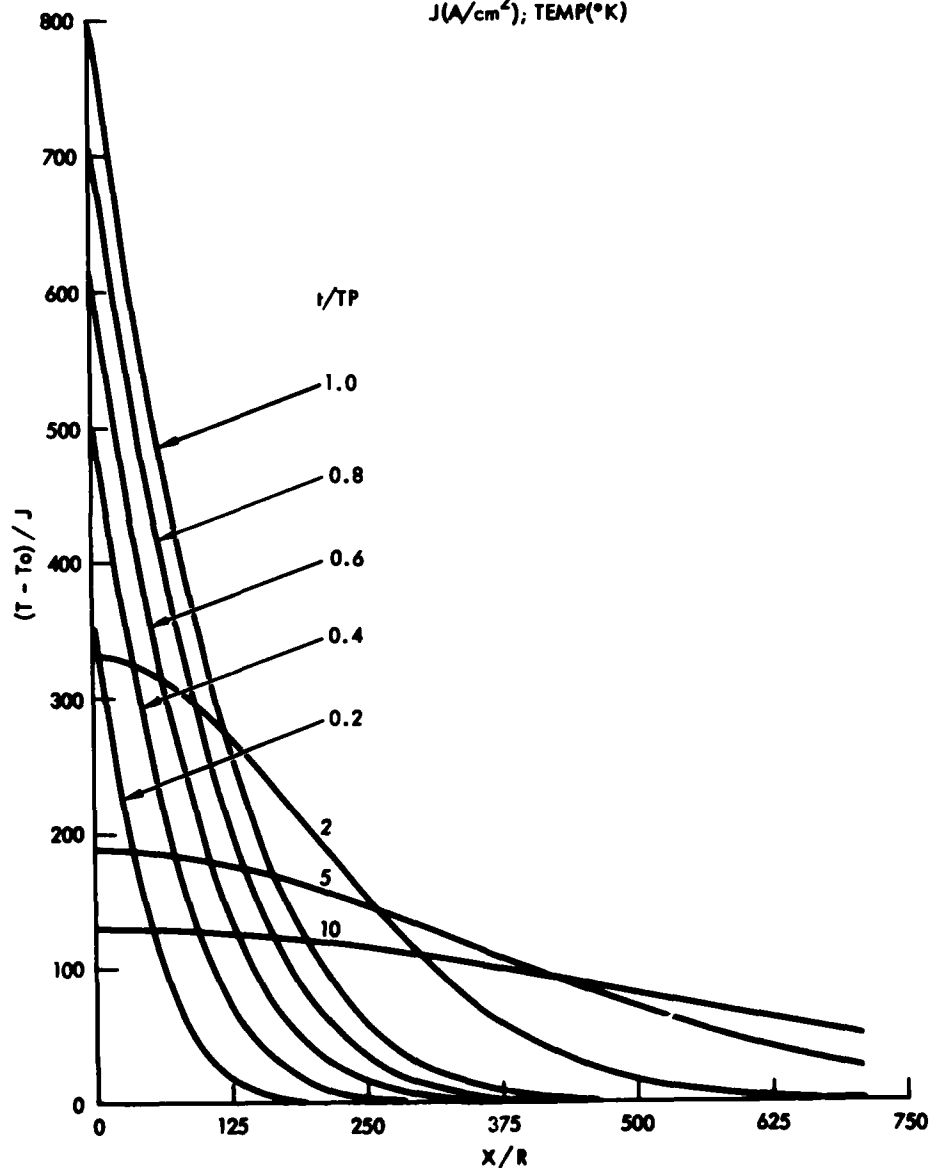


Figure 5. Temperature profiles for pulsed laser blowoff per unit current density J. Pulse length $t_p = 4 \times 10^{-5}$ sec, ion energy $E = 100$ keV, projected range $R = 2.994 \times 10^{-5}$ cm.

BORON INTO SILICON
TEMPERATURE RISE PER UNIT CURRENT DENSITY J

PULSE LENGTH $t_p = 4.0 \times 10^{-5}$ sec

ENERGY $E = 1.8 \times 10^5$ eV

RANGE $R = 4.8720 \times 10^{-5}$ cm

$J(\text{A}/\text{cm}^2)$; TEMP($^{\circ}\text{K}$)

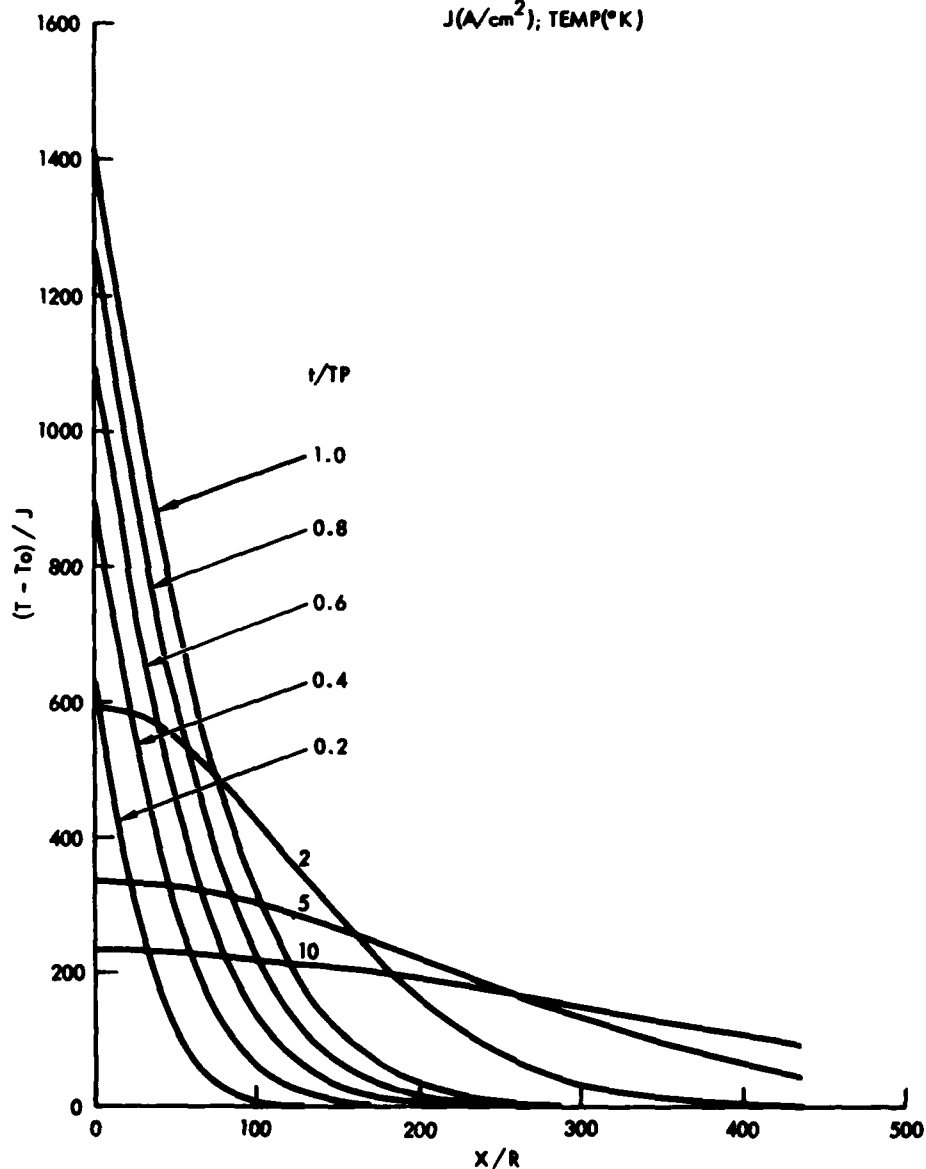


Figure 6. Temperature profiles for pulsed laser blowoff per unit current density J. Pulse length $t_p = 4 \times 10^{-5}$ sec, ion energy $E = 180$ keV, projected range $R = 4.872 \times 10^{-5}$ cm.

$$\Delta T \approx \frac{E J_0}{e} \frac{t_p}{c_p x_{th}} \approx 700^\circ K, \quad (19)$$

and the time it takes for the temperature to drop to about 1/2 of its maximum surface value is $t_{1/2} \approx 4t_R$.

Inspection of Figure 2-6 confirms the essential correctness of these elementary estimates. In Figure 2, the maximum surface temperature per unit current is $\Delta T_m \approx 80^\circ K$ for $E = 20$ keV and $t_p = 10$ μ sec. The temperature distribution halfwidth is $\approx 500 x_R \approx 3 \times 10^{-3}$ cm, which is in very good agreement with $x_{th} \approx \sqrt{4\kappa/c_p t_p} \approx 3 \times 10^{-3}$ cm. Figure 3 shows the temperature increase with the ion energy E . Because of the limit $x_{th} \gg x_R$, the temperature increases with E approximately linearly. Figures 4 and 5 show the effect of increasing the pulse length t_p . For the same energy, both the depth of the heated volume and the surface temperature increase approximately as the square root of the pulse length t_p . Figure 6 shows the temperature profiles for $t_p = 40$ μ sec and $E = 180$ keV. These values represent probably the maximum achievable pulse length and ion energy, respectively. For $J_0 = 1$ A/cm², the maximum surface temperature is $\Delta T_m \approx 1,400^\circ K$, and the surface remains at this elevated temperature during a time interval of, say, one-tenth of t_p .

A practical annealing of damage in ion-implanted semiconductors occurs either because of a rapid melting and regrowth of the surface implanted region, or because of a slow solid state regrowth of the crystalline lattice. For example, in pulsed laser-induced heating, the typical laser pulse lengths are $t_p \approx 10 - 100$ nsec, laser energy $Q \approx 1$ J, and the optical absorption depth $x_{abs} \approx x_{th} \approx .5$ μ m. Performing elementary estimates similar to those above, and assuming reflection losses of 50%, the temperature rise at the surface is $\Delta T_m \approx Q/c_p x_{abs} \approx 5,000^\circ K$, which indicates surface melting. This has been indeed confirmed by more detailed calculations and experimental observations.

The temperature profiles as calculated here for the ion bombardment of silicon were calculated for $J_0 = 1 \text{ A/cm}^2$. In practice, this current value is difficult to achieve, a more probable value being $\approx .1 \text{ A/cm}^2$. Clearly, the temperatures obtained during the ion bombardment are insufficient to produce surface melting.

The solid-state regrowth annealing occurs during cw laser processing. There, typical laser parameters are laser power $P \approx 2 \times 10^5 \text{ W/cm}^2$, scanning velocity $v = 2.76 \text{ cm s}^{-1}$, and the beam cross-section diameter $d = 38 \text{ }\mu\text{m}$. Under these conditions, the heating is thermal diffusion-limited. Using the same elementary analyses as above, the maximum surface temperature is given by $\Delta T_m \approx Pd/vc_p \times t_{th} \approx \frac{P}{2} \sqrt{d/vc_p}$. Assuming 50% reflection losses, this gives $\Delta T_m \approx 1,500^\circ\text{K}$. This ΔT_m lasts during an effective heating time interval of $t_{heat} \approx d/v \approx 15 \times 10^{-4} \text{ sec}$, and although the amount of the absorbed energy is insufficient to produce surface melting, the induced temperature is very close to the material melting temperature. Comparing these estimates with those for ion beam bombardment, it is clear that heating induced during the ion bombardment is too low to produce efficient annealing during the bombardment.

APPENDIX REFERENCES

1. TRW DSSG, "Laser-Assisted Semiconductor Device Processing," Semi-Annual Technical Reports I and II, June 1978 - January 1979 and February 1979 - June 1979, DARPA Contract No. MDA 903-78-C-0284.
2. S. M. Sze, Physics of Semiconductor Devices, Wiley-Interscience, New York (1969).
3. J. Z. Wilcox, "The Effect of Carrier Diffusion on Laser Heating of Lightly Damaged Semiconductors", J. Appl. Physics, April, 1980.
4. R. D. Evans, "Passage of Heavy Charged Particles through Matter," Chapter 22 in "The Atomic Nucleus", McGraw-Hill Book Company (1955).